Coded Excitation with Lead-Free Ultrasonic Arrays: From Complex Structural Integrity Assessments to Intravascular Ultrasound Imaging

Elmergue Germano

Department of Electronic and Electrical Engineering

University of Strathclyde

A thesis submitted for the degree of

Doctor of Philosophy

January 2026

Copyright

Signed: Elmargue Germano

Date: 07/01/2026

Acknowledgements

I would foremost like to express my sincere gratitude to my supervisors, Professor Dr. Anthony Gachagan and Dr. Ehsan Mohseni from the Centre for Ultrasonic Engineering (CUE), Department of Electronic and Electrical Engineering at the University of Strathclyde and Dr. Kwok Ho Lam from the Centre for Medical and Industrial Ultrasonics (CMIU), James Watt School of Engineering, University of Glasgow. Their academic guidance, continuous support and opportunities throughout the duration of this work have been invaluable. Special thanks should be given to Mr. David Lines, Knowledge Exchange Fellow at CUE, for generously sharing his extensive expertise in ultrasonics, which has proven an invaluable asset throughout this research.

To all my colleagues, both past and present, I express gratitude for your time, expertise, and for creating an enriching and enjoyable research environment over the past few years.

I extend heartfelt gratitude to the UKRI EPSRC Centre for Doctoral Training in Future Ultrasonic Engineering (FUSE CDT) for their support of this work and for delivering high-quality training throughout the completion of this programme. Furthermore, I am deeply grateful to Novosound Ltd., for fostering a strong connection between this research and industry.

To my family, especially my mother, Joaquina, for their unconditional love, faith and encouragement. Thank you for instilling in me the dedication and confidence necessary to make this achievement possible – this work is dedicated to you.

Abstract

The superior piezoelectric coefficients of ceramics, including Lead Magnesium Niobate-Lead Titanate (PMN-PT) and Lead Zirconate Titanate (PZT), make them ideal for high-performance transducers, driving their extensive use in industrial and medical sectors. However, the presence of lead in these materials has raised apprehensions about potential risks to the environment and human health. To comply with global regulations, the prompt adoption of lead-free alternatives is essential to advance the development of environmentally sustainable piezoelectric materials.

In Non-Destructive Testing (NDT) contexts, the growing complexity of components has driven the development of flexible ultrasonic probes, allowing efficient inspection without requiring custom wedges to accommodate to intricate surfaces. In medical settings, piezoelectric transducers such as those based on PMN-PT are the preferred choice for commercial Intravascular Ultrasound (IVUS) catheters owing to their mature fabrication processes. Nonetheless, the lead content in these materials raises health and safety concerns, and this work explores the application of scalable, lead-free, flexible, high-frequency (~20 MHz) ultrasonic arrays in these two settings.

Coded excitation strategies in conjunction with Full Matrix Capture (FMC) and Total Focusing Method (TFM) were applied to inspect thick non-planar industrial components. The Golay-based TFM demonstrated superior performance compared to the pulse-based TFM. Golay excitation strategies offer reduced data acquisition and frame rate (by a factor of two) compared to single transmission excitations, and can introduce motion-dependent

decoding errors. Therefore, investigations on single transmission Barker and chirp signals were also undertaken. Moreover, a novel Signal-to-Noise Ratio (SNR) approach was introduced, enabling the evaluation of a single-cycle pulse, Barker and chirp excitation schemes in simulation and experimentation. The ultrasonic array demonstrated excellent conformity to the non-planar components, and the coded excitation schemes consistently achieved better imaging quality in relation to pulse excitation.

The medical context introduced a scalable, RoHS-compliant, 5 French gauge ultrasonic array, leveraging its fabrication benefits for IVUS imaging. Despite exhibiting lower piezoelectric coefficient values in relation to its lead-based counterparts, resulting in reduced signal quality, the lead-free array demonstrates effective imaging performance through the use of coded excitation strategies, enabling the detection of calcified plaques in ex-vivo porcine heart arteries. The array was then characterised through electrical impedance and pulse-echo responses. Coded chirp and Barker excitations were used to image the arteries, detecting calcified plaques, with chirp offering better imaging quality. A 10-µm haematoxylin and eosin histological section of an artery was used for comparison with an IVUS image, showing strong concordance in detecting the calcified plaque.

The accumulation of this work underscores the potential of flexible lead-free RoHS-compliant arrays as an effective approach to address the increasing complexity of industrial components and a sustainable solution for the next generation of IVUS systems. Combining the array with coded excitation provides additional SNR gain and increases penetration depth, which enhances the scope of industrial and medical applications to which this flexible lead-free array can be deployed.

Contents

List of Figures

List of Tables

Abbreviations

1-D	One-Dimensional
2-D	Two-Dimensional
3-D	Three-Dimensional
ADC	Analogue To Digital Converter
AlN	Aluminium Nitride
Ave	Average
BNT	Sodium Bismuth Titanate
BP	Beam Pattern
BT	Barium Titanate
CAD	Coronary Artery Disease
CVD	Cardiovascular Disease
DC	Direct Current
DI	Deionised
EU	European Union
FFT	Fast Fourier Transform
FMC	Full Matrix Capture
GCS	Golay Complementary Sequences
IVUS	Intravascular Ultrasound
KNN	Potassium Sodium Niobate
MDU	Motor Drive Unit

MFMC	Multi-Frame Matrix Capture
NDE	Non-Destructive Evaluation
NDT	Non-Destructive Testing
PAUT	Phased Array Ultrasonic Testing
PCI	Percutaneous Coronary Interventions
PCIe	Peripheral Component Interconnect Express
PLA	Polylactic Acid
PMN-PT	Lead Magnesium Niobate-Lead Titanate
PVDF	Polyvinylidene Fluoride
PZT	Lead Zirconate Titanate
RF	Radio Frequency
RMS	Root Mean Square
RoHS	Restriction Of Hazardous Substances
SD	Standard Deviation
SDH	Side-Drilled Hole
SFR	Signal-To-Filter Artifact Ratio
SNR	Signal-To-Noise Ratio
SSR	Signal-To-Sidelobe Artifact Ratio
TFM	Total Focusing Method
UTA	Universal Transducer Adapter
ZnO	Zinc Oxide

Chapter 1

Introduction

1.1. Industrial Motivation

Piezoelectric ceramics, including Lead Zirconate Titanate (PZT) and Lead Magnesium Niobate-Lead Titanate (PMN-PT), are extensively employed in industrial and medical ultrasonic imaging applications due to their high piezoelectric coefficients, which enables high-performance transducer operation. Nevertheless, concerns regarding the human health and environmental risks associated with the lead content in these materials have been raised [1]. In accordance with global regulatory frameworks, such as the Restriction of Hazardous Substances (RoHS) directive established by the European Union (EU) and similar legislations in China and Japan, the timely adoption of lead-free alternatives is essential for advancing the development of environmentally sustainable piezoelectric materials [2-4].

Fig. 1.1 depicts the annual number of published articles on various transducer materials from 1985 to 2022, as recorded in the Web of Science platform, revealing a notable increase of over 200 % in publications between 2004 and 2022. Particular emphasis is placed on sodium bismuth titanate (BNT) and potassium sodium niobate (KNN), with additional consideration given to materials such as polyvinylidene fluoride (PVDF) and barium titanate (BT). The data indicates that research in the field of lead-free piezoceramics has attained a significant level of maturity in recent years. Numerous findings regarding the piezoelectric properties of lead-free materials have been reported over the past two decades. However, challenges remain in translating these results into large-scale production [5-7].

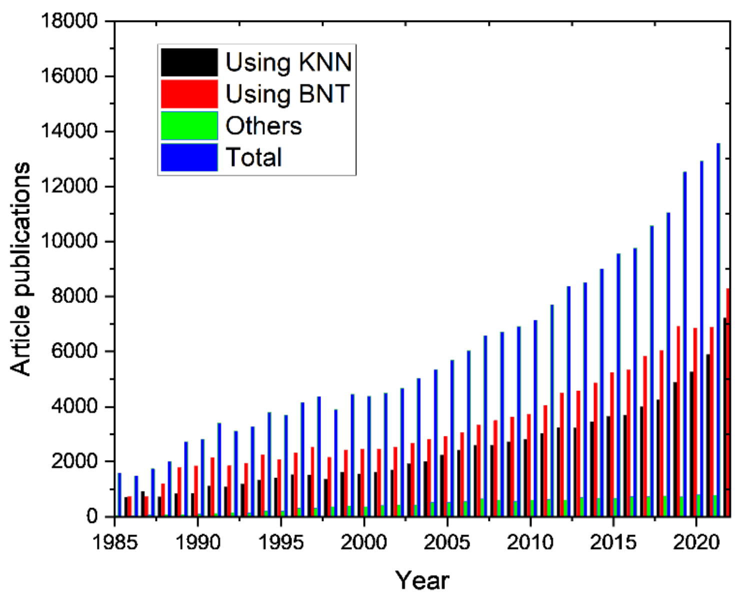

Figure 1. 1: Annual number of published articles from 1985 to 2022, with emphasis on BNT and KNN-based materials as documented by the Web of Science platform.

The increasing intricacy of industrial components has spurred the development of conformable ultrasonic probes, enabling efficient inspection without the need for custom-designed wedges to adapt to complex surfaces. In alignment with these advancements and considering medical applications, flexible ultrasonic arrays have been explored for their capability to inspect complex, non-planar surfaces [8-15]. For example, a flexible lead-based ultrasonic array was employed to acquire high-resolution Total Focusing Method (TFM) images of flaws within components with irregular surfaces [11].

Piezoelectric transducers, such as those utilising PMN-PT, remain the preferred choice for commercial intravascular ultrasound (IVUS) catheters due to their well-established fabrication processes. However, the presence of lead in these materials poses substantial environmental and human health-related concerns, necessitating imperative consideration for sustainable alternatives [16, 17].

The ultrasonic arrays utilised in this work incorporate zinc oxide as a piezoelectric material, produced through a thin film fabrication process. An overview on ultrasonic arrays, encompassing their configurations, benefits, and limitations, is elaborated in sub-section 2.1.4. Lead-free thin-film piezoelectric materials including zinc oxide and aluminium nitride are among the most commonly utilised compounds in this field [18, 1]. These lead-free arrays exhibit a markedly inferior piezoelectric coefficient relative to their lead-based counterparts, contributing to reduced signal-to-noise ratio (SNR), and thereby limiting their widespread adoption in conventional industrial and medical applications. Conventional strategies for improving the SNR in ultrasonic arrays entail either decreasing the frequency or averaging signals over multiple transmissions. However, these methods inherently compromise resolution and data acquisition speed, respectively [19]. Coded excitation schemes hold promise for integration with these lead-free arrays to improve their SNR. A comprehensive review on coded excitation is provided in sub-section 2.5. Coded excitation techniques improve SNR without sacrificing acquisition speed by employing extended coded pulses rather than repeated pulses. The fundamental resonant frequencies of piezoelectric films are generally around 1 GHz, which makes these materials impractical for NDT and medical applications. By introducing a thin, flexible metallic substrate combined with mass loading to the piezoelectric film, operating frequencies have been successfully reduced to below 50 MHz, providing opportunities to investigate its use in both industrial and medical applications. Precise control over thickness, composition and scalability is achieved, thereby enabling large-scale production that is both efficient and cost-effective [1, 18, 20]. This thesis investigates the application of coded excitation strategies with the lead-free array technology to develop systems which are appropriate for application in real-world applications associated with industrial and medical sectors.

1.2. Contribution to Knowledge

The contributions to knowledge generated as a result of the work of this Doctor of Philosophy are outlined below:

- Application of advanced phase-modulated dual transmission Golay coded excitation technique and TFM imaging algorithm combined with a high-frequency, lead-free, flexible ultrasonic array for inspection of thick non-planar industrial components.
- Examination and comparison of the performance associated with the single transmission phase-modulated Barker signal and the frequency-modulated chirp signal excitation schemes to improve the ultrasonic array operability in thick convex and concave test specimens.

- A novel SNR methodology, enabling the characterisation of the image noise region and the identification of parameters where the SNR achieves stabilisation.
- Development of a novel lead-free array transducer system for intravascular ultrasound catheters. The system incorporates a lead-free, high-frequency, flexible array transducer combined with coded excitation schemes to improve the signal quality, allowing imaging and detection of calcific plaques in *ex-vivo* porcine heart arteries.

1.3. Thesis Structure

The organisational structure of this work is as follow: Chapter 2 provides the essential theoretical foundation necessary for understanding the research presented throughout the rest of this thesis. This encompasses a brief overview of the core principles of ultrasonic inspection, including piezoelectricity, wave propagation, attenuation as well as the functionality of single-element and array transducers. This is followed by information on the inspection of complex-geometry components, highlighting current flexible ultrasonic array technologies in both research and commercial phases. Sub-section 2.3 presents technical background on intravascular ultrasound, covering atherosclerosis, essential system components of IVUS, and considerations of transducer materials in catheter design. Sub-section 2.4 contains information on the Zinc Oxide-based ultrasonic arrays utilised in this work. The parameters of the arrays used in the industrial and the medical settings are detailed in this sub-section. The next sub-section details information on modulated signals and background on pulse compression. Sub-section 2.6, the last sub-section in chapter 2, contains information on ultrasonic data presentation. This includes details on A-scans, B-scans, C-scans, FMC

and TFM, as well as Hilbert Transform considerations. Chapter 3 introduces novel work on the application of phase-modulated dual transmission Golay coded excitation scheme, combined with FMC/TFM imaging algorithm and the high-frequency, lead-free, flexible ultrasonic array. This allowed inspection of thick non-planar industrial components. Chapter 4 investigates and compares the efficacy of the single transmission Barker and chirp strategies to optimise the ultrasonic array performance in thick convex and concave test specimens. Moreover, a novel SNR methodology is introduced, facilitating the characterisation of image noise regions and identification of parameters at which SNR stabilisation is achieved. Chapter 5 presents a 5 French gauge, approximately 1.67 mm diameter, 32-element ultrasonic array transducer with a 163 μm pitch and a 3.82 mm elevation, enabling radial scanning in ex-vivo porcine heart arteries. This represents a novel lead-free array transducer system for intravascular ultrasound catheters. In Chapter 6, a summary of the research detailed in prior chapters of this thesis is provided and directions for future work in both industrial and medical applications are proposed.

1.4. Publications and Awards

The journal publications as lead author produced during the completion of this Doctor of Philosophy are outlined below:

- **Germano, E.**, Tabatabaeipour, M., Mohseni, E., Lines, D., MacLeod, C. N., Lam, K.-H., Hughes, D., Trodden, H., & Gachagan, A. (2025). Application of Golay-based total focusing method using a high-frequency, lead-free, flexible ultrasonic array for inspection of thick non-planar industrial components. *NDT & E International*, *150*, 103282. https://doi.org/10.1016/j.ndteint.2024.103282

- **Germano, E.**, Mohseni, E., Lines, D., Tabatabaeipour, M., MacLeod, C. N., Lam, K.-H., Hughes, D., Trodden, H., & Gachagan, A. (2025). Single transmission phase- and frequency-modulated coded excitation for enhanced inspection of thick complex industrial components using a scalable, flexible, lead-free, ultrasonic array. *NDT & E International*, 158, 103564. https://doi.org/10.1016/j.ndteint.2025.103564
- **Germano, E.**, Core, G., Metzger, H., Russell, D., Kinney, J., Mohseni, E., Lines, D., Lam, K.-H., Hughes, D., Trodden, H., & Gachagan, A. (2025). Calcified plaque detection in ex-vivo porcine heart arteries using a scalable, zinc oxide-based intravascular ultrasound array with real-time coded excitation schemes. ***In preparation.***

The conference contributions as lead author produced during the completion of this Doctor of Philosophy are outlined below:

- **Germano, E.**, Core, G., Kinney, J., Russell, Mohseni, E., Lines, D., Lam, K.-H., Hughes, D., Trodden, H., Gachagan, A. Detection of Calcified Plaques in ex-Vivo Porcine Heart Arteries Using a scalable, eco-Friendly Zinc oxide-Based Intravascular Ultrasound Array with real-Time Coded Excitation. Lecture Presentation session presented at IEEE International Ultrasonics Symposium (*IEEE IUS 2025*), Utrecht, Netherlands.

- **Germano, E.**, Mohseni, E., Lines, D., Tabatabaeipour, M., Lam, K.-H., Hughes, D., Trodden, H., Gachagan, A. Single Transmission phase- and frequency-Modulated Signals for Enhanced Inspection of Thick Complex Industrial Components Using a Flexible eco-Friendly Ultrasonic Array. Lecture Presentation session presented at IEEE International Ultrasonics Symposium (*IEEE IUS 2025*), Utrecht, Netherlands.
- **Germano, E.**, Mohseni, E., Lines, D., Tabatabaeipour, M., Lam, K.-H., Hughes, D., Trodden, H., Gachagan, A. Ultrasonic Inspection of Industrial Components with Complex Geometries Using Optimised Single Transmission Modulated Signals and a Flexible Eco-Friendly Ultrasonic Array. Presentation session presented at BINDT – 62nd Annual British Conference on NDT (*NDT 2025*), Edinburgh, United Kingdom.
- **Germano, E.**, Tabatabaeipour, S. M., Mohseni, E., Gachagan, A., Lam, K. H., Hughes, D., & Trodden, H. Improving industrial inspections with high-frequency flexible ultrasonic arrays. Presentation session presented at The Doctoral School Multidisciplinary Symposium (*DSMS 2023*), Glasgow, United Kingdom.
- **Germano, E.**, Tabatabaeipour, M., Mohseni, E., Gachagan, A., Lam, K., & Lines, D. Improving industrial inspections combining high-frequency flexible ultrasonic arrays and coded excitation. Presentation session presented at BINDT - 60th Annual British Conference on NDT (*BINDT 2023*), Northampton, United Kingdom.

- **Germano, E.**, Tabatabaeipour, S. M., Mohseni, E., Lines, D., Gachagan, A., Lam, K. H., Hughes, D., & Trodden, H. Golay-based total focusing method using a high-frequency, lead-free, flexible ultrasonic array to improve industrial inspections. Presentation session presented at Anglo-French Physical Acoustics Conference (*AFPAC 2024*).
- **Germano, E.**, Walker, J., Mills, B., Javadi, Y., Buffa, G., MacLeod, C. N., Gachagan, A., Pierce, G., Mineo, C., Tamimi, S., Mohseni, E., & Lam, K. H. Enhancing additive friction stir deposition through comprehensive ultrasonic defect detection and process optimisation. Poster session presented at UK & Ireland IEEE Ultrasonics, Ferroelectrics And Frequency Control Chapter (*IEEE UFFC 2024*), Glasgow, United Kingdom.
- **Germano, E.**, Tabatabaeipour, M., Mohseni, E., Lines, D., MacLeod, C. N., Lam, K.-H., Hughes, D., Trodden, H., & Gachagan, A. Application of Golay-Coded Excitation Schemes with a Lead-Free, High-Frequency, Flexible Ultrasonic Array for Defect Detection of Thick, Non-Planar Components. Presentation session presented at UK & Ireland IEEE Ultrasonics, Ferroelectrics And Frequency Control Chapter (*IEEE UFFC 2024*), Glasgow, United Kingdom.
- **Germano, E.**, Deans, M., Lam, K. H & Bailet, G. *Application of Total Focusing Method in Thin, Strongly Attenuating Materials for Aerospace Applications*. Poster session presented at UK & Ireland IEEE Ultrasonics, Ferroelectrics And Frequency Control Chapter (*IEEE UFFC 2024*), Glasgow, United Kingdom.

- **Germano, E.**, Tabatabaeipour, M., Mohseni, E., Lines, D., Gachagan, A., Lam, K.-H., Hughes, D., & Trodden, H. Synergizing High-Frequency Flexible Ultrasonic Arrays and Coded Excitation Schemes for Advanced Industrial Inspections. Presentation session presented at 20th World Conference on Non-Destructive Testing (*WCNDT 2024*), Incheon, Republic of Korea.
- **Germano, E.**, Lines, D., Tabatabaeipour, M., Mohseni, E., Gachagan, A., Lam, K.-H., Hughes, D., Trodden, H. & MacLeod, C. N. Application of phase and frequency modulated signals to improve defect detection in thick, non-planar components using a lead-free, high-frequency, flexible ultrasonic array. Poster session presented (online) at IEEE Ultrasonics, Ferroelectrics, and Frequency Control Joint Symposium (*UFFC-JS 2024*), Taipei, Taiwan.
- **Germano, E.**, Lines, D., Tabatabaeipour, M., Mohseni, E., Gachagan, A., Lam, K.-H., Hughes, D., Trodden, H. & MacLeod, C. N. Application of phase and frequency modulated signals to improve defect detection in thick, non-planar components using a lead-free, high-frequency, flexible ultrasonic array. Poster session presented at The Advanced Nuclear Research Centre (*ANRC 2024*) Research Showcase, Glasgow, United Kingdom.
- **Germano, E.**, Tabatabaeipour, M., Mohseni, E., Lines, D., Gachagan, A., Lam, K.-H., Hughes, D., Trodden, H. & MacLeod, C. N. Application of phase-modulated Golay codes for defect detection in thick, non-planar components using a lead-free, high-frequency, flexible ultrasonic array. Poster session presented at

The UKRI EPSRC Centre for Doctoral Training in Future Ultrasonic Engineering (*FUSE CDT 2024*) Annual Scientific Meeting, Glasgow, United Kingdom.

- **Germano, E.**, Deans, M., Lam, K. H & Bailet, G. Application of Total Focusing Method in Thin, Strongly Attenuating Materials for Aerospace Applications. Poster session presented at The UKRI EPSRC Centre for Doctoral Training in Future Ultrasonic Engineering (*FUSE CDT 2024*) Annual Scientific Meeting, Glasgow, United Kingdom.
- **Germano, E.**, Walker, J., Mills, B., Javadi, Y., Buffa, G., MacLeod, C. N., Gachagan, A., Pierce, G., Mineo, C., Tamimi, S., Mohseni, E., & Lam, K. H. Enhancing additive friction stir deposition through comprehensive ultrasonic defect detection and process optimisation. Poster session presented at The UKRI EPSRC Centre for Doctoral Training in Future Ultrasonic Engineering (*FUSE CDT 2024*) Annual Scientific Meeting 2024, Glasgow, United Kingdom.
- **Germano, E.**, Core, G., Mohseni, E., Lines, D., Lam, K.-H., Kinney, J., Russell, D., Gifford, J., deGuzman, B. J., Hughes, D., Trodden, H., Gachagan, A. Calcified plaque imaging and detection in ex-vivo porcine heart arteries using a scalable, lead-free intravascular ultrasound array. Presentation session presented at The Scottish Imaging Network: A Platform for Scientific Excellence (*SINAPSE 2025*) Annual Scientific Meeting, Aberdeen, United Kingdom.
- **Germano, E.**, Mohseni, E., Lines, D., Gachagan, A., Lam, K.-H., Hughes, D., & Trodden, H. Towards lead-free transducers: Employing Zinc Oxide-based, high-frequency, flexible ultrasonic arrays for industrial and medical settings.

Presentation session presented at The UKRI EPSRC Centre for Doctoral Training in Future Ultrasonic Engineering (*FUSE CDT 2025*) Annual Scientific Meeting, Glasgow, United Kingdom.

The awards as lead author produced during the completion of this Doctor of Philosophy are outlined below:

- Student Pitch Competition: 3rd Place. IEEE International Ultrasonics Symposium (IUS). September 15-18, 2025. Utrecht, Netherlands. Detection of Calcified Plaques in ex-Vivo Porcine Heart Arteries Using a scalable, eco-Friendly Zinc oxide-Based Intravascular Ultrasound Array with real-Time Coded Excitation.
- Best Oral Presentation: Runner-Up. FUSE CDT Annual Scientific Meeting. June 4th, 2025. Glasgow, United Kingdom. Towards lead-free transducers: Employing Zinc Oxide-based, high-frequency, flexible ultrasonic arrays for industrial and medical settings.

1.5. Industrial Collaboration

The research conducted during this Doctor of Philosophy has been supported by Novosound Ltd., with a particular focus on advanced ultrasonic Non-Destructive Evaluation (NDE) activities for complex-geometry inspection, and advanced ultrasonic medical imaging activities for imaging *ex-vivo* porcine heart arteries.

Working with Novosound has allowed engagement and collaboration opportunities with industry. This included a 3-month secondment that enabled the integration of coded excitation schemes for intravascular ultrasound imaging applications. This showcased some of the contributions of this doctoral research, as well as served as an opportunity to acquire insights and expertise through engagement with industry specialists. Moreover, participation in numerous site visits has allowed deployment of on-site inspections. These visits played a pivotal role in translating this research from academia to real-world industrial contexts, aligning the work with both present demands and future technological needs.

This work was supported by the UKRI EPSRC Centre for Doctoral Training in Future Ultrasonic Engineering (FUSE CDT) under the EPSRC Grant reference EP/S023879/1.

Chapter 2

Technical Background

The capability to assess the integrity of materials, structures and tissues non-destructively is an essential process in numerous industrial and medical applications. Typical medical imaging techniques include radiology, magnetic resonance and ultrasound, while the common methods for industrial asset inspection include eddy current, ultrasound, liquid penetrant, radiographic and thermographic testing [21-25]. Nevertheless, among the versatile and practical inspection techniques widely employed in both industrial NDT and medical imaging, ultrasound remains an effective imaging technique. The propagation of acoustic waves through a medium has applications such as inspection of complex-geometry industrial components [8, 26] and evaluating coronary artery disease in the medical field [27]. This chapter provides the essential theoretical and technical foundations required to understand the original contributions developed in the subsequent chapters of this thesis.

2.1. Fundamentals of Ultrasonic Inspection

2.1.1. Piezoelectricity

Piezoelectricity, initially demonstrated in 1880 by the Curie brothers, Pierre and Jacques [28], has become fundamental to the design and fabrication of ultrasonic transducers utilised in NDT and medical applications. It is attributed to the reversible conversion between mechanical and electrical energy. The piezoelectric effect describes the behaviour of piezoelectric materials that generate an electrical charge proportional to the applied mechanical stress. The converse of the conversion of energy is known as the inverse piezoelectric effect [28]. Ultrasonic transducers in both industrial and medical sectors generate and detect ultrasound energy through these effects.

2.1.2. Wave Propagation

The term *ultrasound* refers to acoustic waves with frequencies exceeding the human auditory range of 20 Hz to 20 kHz [29]. Acoustic energy produced by a transducer propagates through a medium by inducing vibrational motions in the particles of the medium. The velocity of ultrasound propagation in a medium, c, is determined by the product of its frequency, f, and the wavelength λ [29], as described in Equation 2.1. The velocity of ultrasound remains constant within a given medium under uniform temperature and stress conditions.

$$c = f\lambda \tag{2.1}$$

The primary ultrasound wave types utilised in industrial and medical imaging are longitudinal and shear (or transverse) waves. Longitudinal waves result from particle vibrations that oscillate parallel to the direction of the wave propagation. Shear waves arise from particle oscillations perpendicular to the direction of the wave propagation. Both wave types are present in tissue, however, shear waves are typically disregarded in standard B-mode (brightness mode) imaging due to their significantly lower velocities relative to longitudinal waves and their high attenuation at high frequencies [30]. Longitudinal and shear waves can propagate in solid media. The selection of wave propagation type is commonly referred to as the *wave mode*, with bulk waves restricted to longitudinal and shear modes [31]. Several additional wave types can be observed, especially at the interface between two materials. These encompass Rayleigh, Guided, and Love waves, which are not pertinent to the research presented in this thesis.

When an ultrasound wave propagates perpendicularly through a material and encounters a boundary interfacing with a material with different acoustic impedance, reflection of the wave occurs at that interface. The acoustic impedance, Z, of an isotropic material is defined as the product of its velocity, c, and density, ρ, as expressed in Equation 2.2. It is frequently required to assume lossless media with perfect energy transfer between molecules in order to comprehend how sound propagates over a boundary where changes in impedance occurs. The proportions of incident acoustic energy transmitted E_T and reflected E_R , for a wave incident normal to the boundary between two media with acoustic impedances Z_1 and Z_2 , are quantitatively described by Equations 2.3 and 2.4, respectively.

$$Z = \rho c \tag{2.2}$$

$$E_T = \frac{4Z_1Z_2}{(Z_1 + Z_2)^2} \tag{2.3}$$

$$E_R = \left(\frac{Z_1 - Z_2}{Z_1 + Z_2}\right)^2 \tag{2.4}$$

This relationship indicates that as the difference in acoustic impedance between the two media increases, a larger fraction of the incident acoustic energy is reflected at the interface, with the correspondingly smaller portion transmitted through the boundary [28, 31]. This is illustrated in Figure 2.1. The transmission is at its peak when $Z_2 = Z_1$. The impedance ratio is 1, and this suggests that the materials have the same properties and no energy is reflected (0 %). As the acoustic impedance ratio deviates from 1, whether below or above, the transmitted energy decreases, while the reflected energy increases. This principle underpins the fundamental application of ultrasonic wave for inspection.

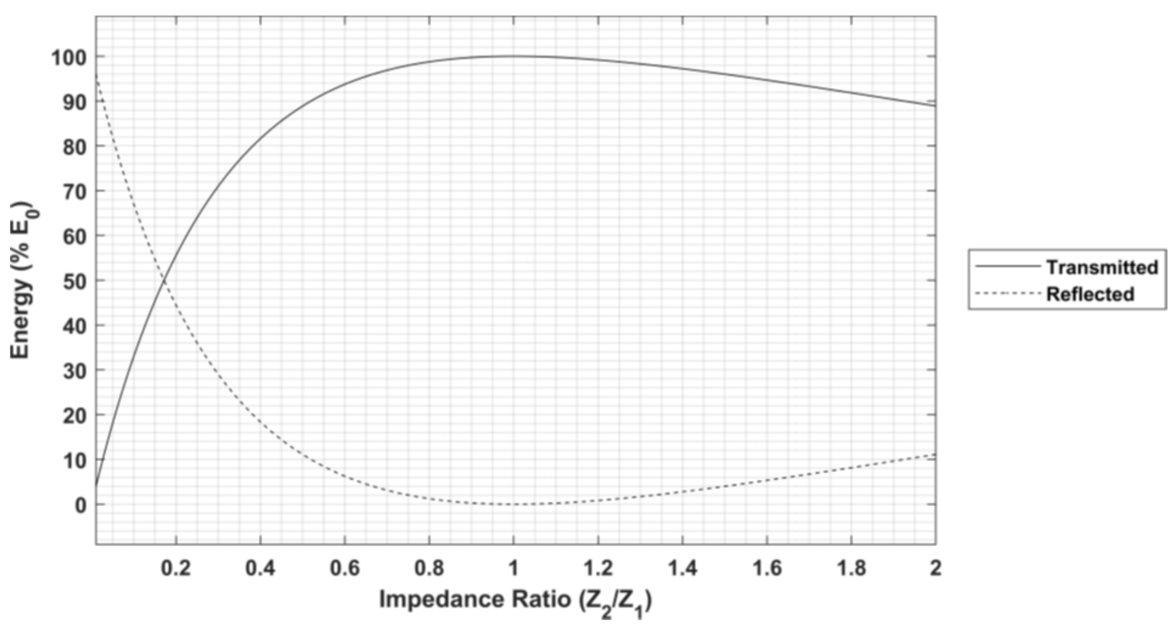

Figure 2. 1: Effect of impedance mismatch on transmitted and reflected energy [31].

When a wave is incident obliquely on a boundary, the situation becomes more complex and multiple factors considered, including reflection, refraction, and mode conversion. For an acoustic wave incident on a boundary between two materials with differing acoustic impedances at a non-zero angle of incidence, the angle of reflection equals the angle of incidence. The relationship governing the angles of incidence and refraction in this context is known as Snell's law, expressed through the equation provided in (2.5) [28]:

$$\frac{sin(\theta_i)}{sin(\theta_t)} = \frac{c_1}{c_2} \tag{2.5}$$

where θ_i is the angle of incidence; θ_t is the transmitted angle; c_1 is the sound wave speed at medium 1; c_2 is the sound wave speed at medium 2. According to Snell's law, for a given pair of media, the ratio of the sine of the angle of incidence to the sine of the angle of refraction equals the ratio of the respective wave speeds in the two media.

2.1.3. Attenuation

As ultrasonic waves propagate through a medium, their energy diminishes due to interactions with the material. This phenomenon, termed attenuation, results from combined effects of absorption, scattering and reflection. Absorption occurs when acoustic energy is converted into thermal energy. Scattering is the effect where acoustic energy is dispersed by structural inhomogeneities within the material, such as grain boundaries, voids, impurities, and crystalline structures. Reflection occurs when acoustic energy is redirected at interfaces with differing acoustic impedances. Furthermore, attenuation is proportional to the frequency of the acoustic wave and the thickness of the medium through which it propagates [30, 32].

2.1.4. Single-element and Array Transducers

Single-element transducers employ a single piezoelectric element to both transmit and receive ultrasonic waves. In NDT, for example, they are commonly used in direct contact with the test specimen, facilitated by a thin layer of liquid coupling – such as water, oil, or glycerine gel – to enhance energy transfer by eliminating air gaps between the transducer and the specimen. Moreover, these transducers can be paired with an angled delay line, known as a wedge, to direct sound propagation at an angle relative to the surface of the test specimen, facilitating the generation of refracted shear waves. This approach is commonly employed for inspecting industrial welded components, especially when direct examination of the rough weld cap is impractical [31].

Array transducers integrate multiple piezoelectric elements within a single housing, expanding the scope and versatility of transducer applications. In NDT and medical imaging settings, ultrasound transducers predominantly employ array configurations. They offer superior coverage, sensitivity, flexibility and adaptability compared to conventional single-element transducers, enabling independent control of individual elements to achieve electronic beam focusing and steering. Ultrasonic array transducers can be broadly categorised into One-Dimensional (1-D), Two-Dimensional (2-D), or annular configurations. While these configurations represent the simplest forms of array design, numerous alternative element patterns are possible. Among them, 1-D linear arrays remain the most prevalent in industrial applications [33]. Figure 2.2 shows a schematic of a 1-D linear array, with its elements distributed in the x direction. The element pitch or spacing (p) can be described by the summation of the element width (w) along the array axis and the gap between adjacent elements (a). The element length is usually termed elevation (e).

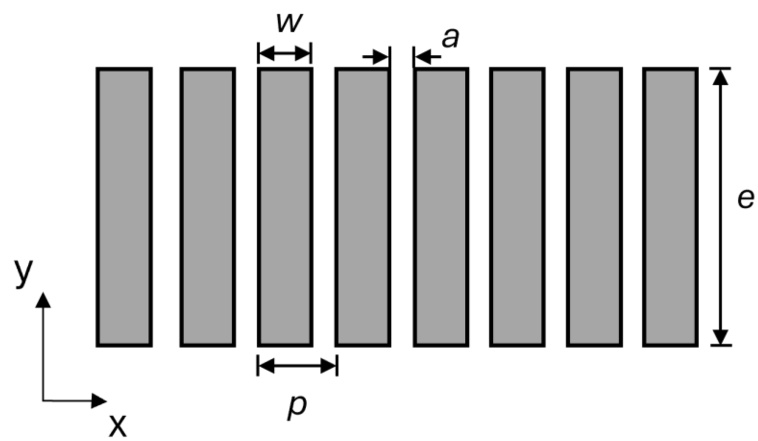

Figure 2. 2: Schematics of a 1-D linear array indicating its typical parameters including the element pitch (p), width (w), gap (a) and elevation (e).

The selection of pitch size is essential for the performance of linear phased array transducers. The optimal element pitch, adhering to the half-wavelength criterion (requiring it to be less than half a wavelength), is essential for supressing grating lobes. The ultrasonic beam is formed through the constructive interference of acoustic waves emitted by individual transducer elements, coherently aligned to reinforce propagation in the intended direction. In certain instances, this interference may also be constructive in unintended directions, resulting in secondary energy maxima, known as grating lobes, emitted beyond the electronically controlled direction. Grating lobes divert energy from the primary ultrasonic beam, potentially causing undesirable reflections and interference during inspection, which may degrade SNR and introduce artifacts [33-35]. This implies an inverse proportionality between the element pitch of an optimal phased array transducer and its operating frequency. Figure 2.3 shows an illustration of an ultrasonic phased array transducer deployed on a 70° wedge on a steel test specimen. The influence of the element pitch size on the generation of grating lobes is examined. No grating lobe generation is observed when the pitch is equal to half a wavelength. Grating lobe generation, at different levels, occurs when the pitch is equal to at least a wavelength.

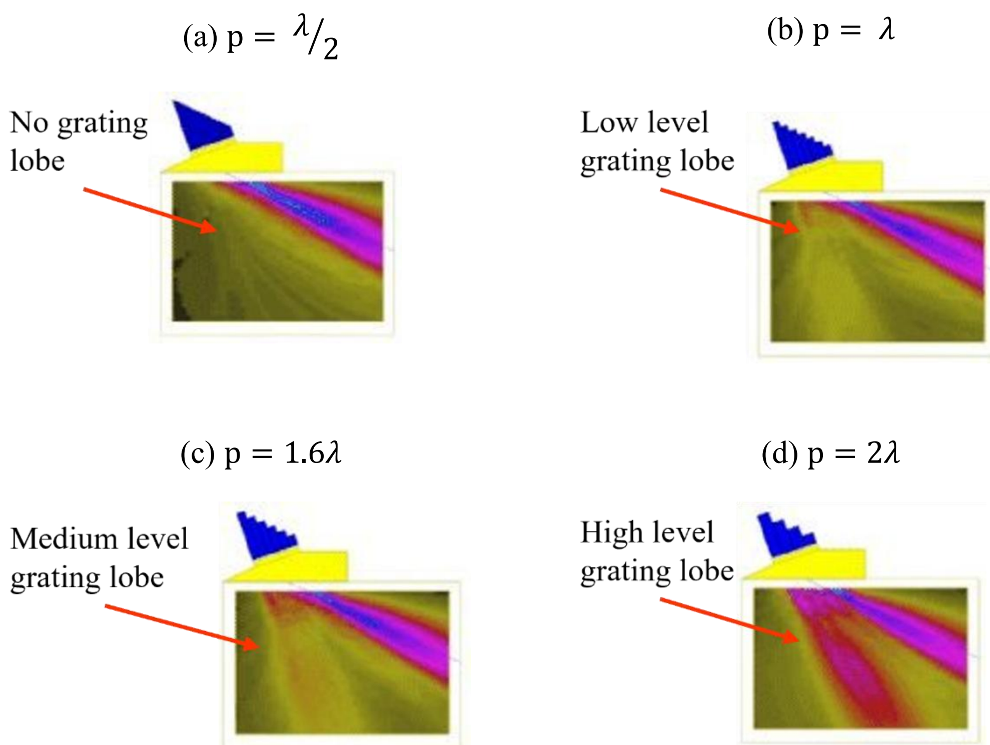

Figure 2. 3: Illustration of the impact of the element pitch size (p) on the generation of grating lobes [33]. (a) No grating lobe generated. The pitch is half a wavelength. (b) Low level of grating lobe generation. (c) Medium level grating lobe generation. The pitch is just over a wavelength. (d) High level grating lobe generation. The pitch is twice the wavelength.

Array transducers can be individually controlled using programmable differential time delays. This enables steering or focusing of the ultrasound beam to specific locations through constructive interference of phase-delayed waves. The differential time delays are commonly referred to as focal laws [31-33]. An unfocused normal plane wave can be transmitted by applying zero delay to the elements, enabling simultaneous firing (in-phase) as illustrated in Figure 2.4 (a). Ultrasonic beam steering can be achieved by applying a linear delay across the transmitting elements, as depicted in Figure 2.4 (b). The focusing capabilities of an ultrasonic array are demonstrated in Figure 2.4 (c). This can be achieved by applying symmetric delay laws to focus directly beneath the aperture centre. Steering and focusing can be integrated to focus the ultrasonic beam at a point offset from the aperture centre, as illustrated in Figure 2.4 (d).

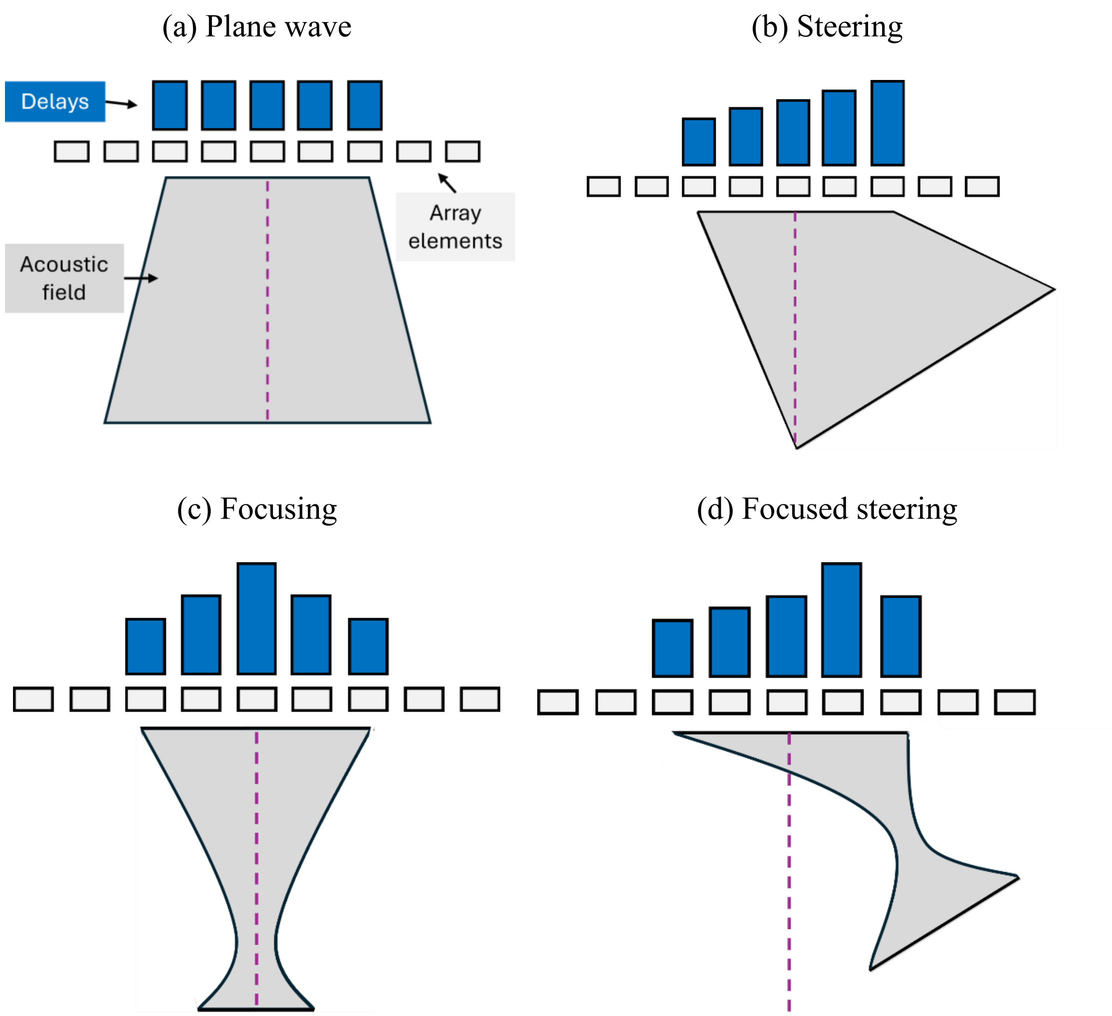

Figure 2. 4: Ultrasonic phased array transducer beamforming characteristics. (a) Unfocused plane wave. (b) Beam steering. (c) Focusing. (d) Focused steering. The delay, array elements and acoustic field are highlighted in (a).

In ultrasonic NDT and medical applications, data acquisition can be performed by either using a single transducer functioning as both transmitter and receiver, or by employing two distinct transducers, with one serving as the transmitter and the other as the receiver. The pulse-echo method is a well-established and easily implemented approach, where a single transducer performs both transmission and reception. In addition to pulse-echo mode, transducers can also be configured to operate in tandem for through-transmission and pitch-catch modes, enabling greater flexibility in inspection techniques depending on the application requirements. Through-transmission configurations position the test specimen between a transmitting and a receiving transducer. Pitch-catch configurations involve the use of two separate transducers positioned on the same side of the test specimen, one functioning as the transmitter and the other as the receiver. Figure 2.5 shows an illustration of the different configurations used in ultrasound data acquisition. In all scenarios, the data acquired by the transducer is presented as a time series plot known as an A-scan. A key advantage of the pulse-echo approach is that it requires access to only one side of the sample. However, its effectiveness depends on material characteristics with sufficiently low acoustic attenuation to allow sound to travel twice the sample thickness while maintaining an adequate energy to provide the SNR required for detection at the receiver. In the through-transmission method, precise alignment is essential, necessitating meticulous calibration of the scanning paths for each transducer. This poses particular challenge when dealing with components with complex geometries. As sound waves only need to pass through the sample once, through-transmission is frequently employed for highly attenuating components or air-coupled ultrasound applications, where low SNR values present significant challenges. In the pitch-catch setup, the transmitter and receiver transducers are maintained at a fixed distance and firing angle relative to each other, enabling them to be scanned together across the surface of the sample. This configuration is particularly effective for detecting defects that are not orientated normally with respect to the beam propagation path (and reception), crack-tip diffractions, as cracks on the bottom surface of the material will reflect ultrasonic waves differently compared to reflections from a defect-free backwall, thereby aiding the identification and characterisation of such defects [31, 32, 36].

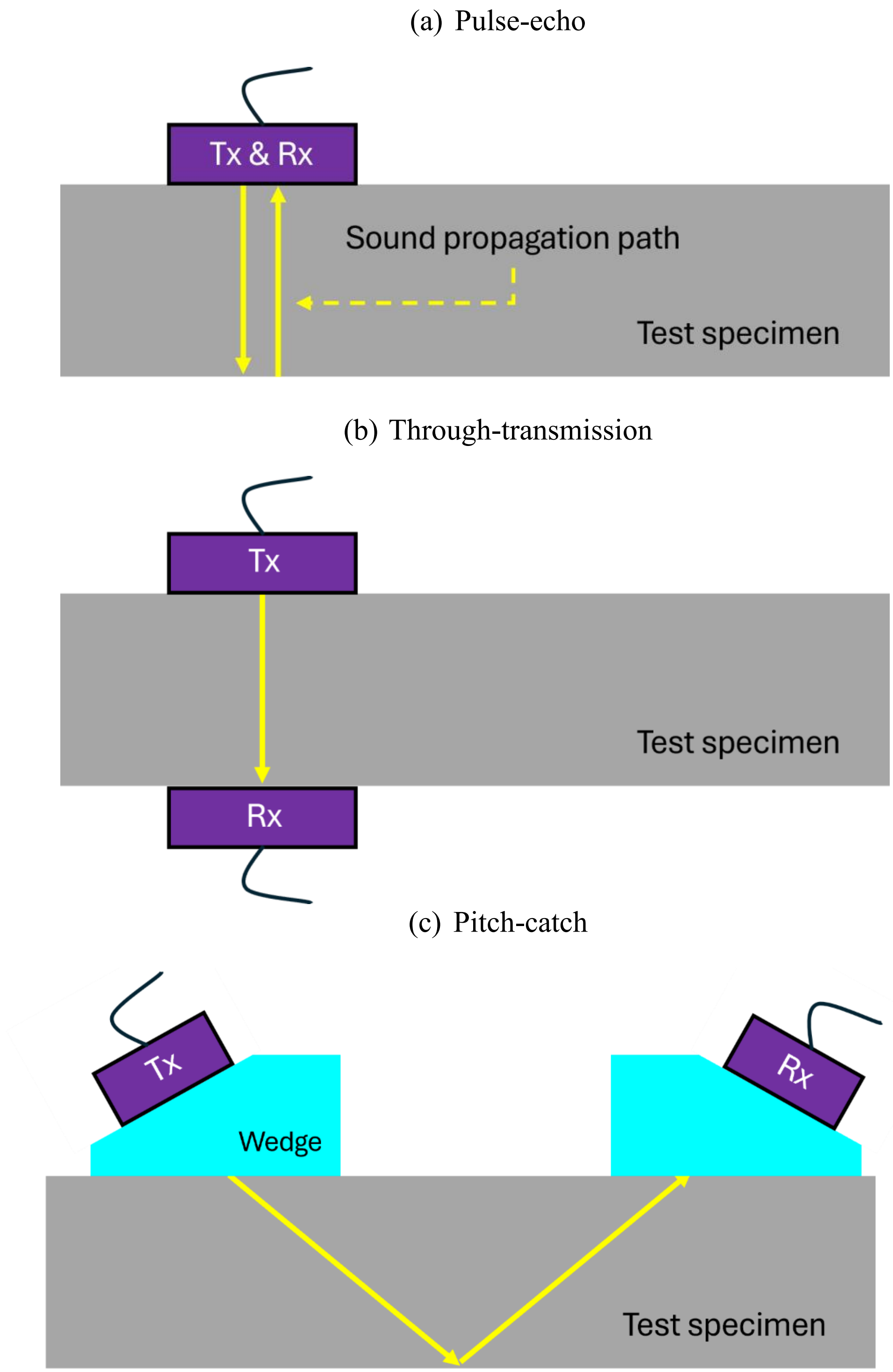

Figure 2. 5: Schematic of different configurations for data acquisition. (a) Pulse-echo configuration. (b) Through-transmission configuration. (c) Pitch-catch configuration. Tx represents the transducer used for transmission and Rx corresponds to the transducer used for reception. The sound propagation path is highlighted in yellow.

2.2. Inspection of Complex-Geometry Components

2.2.1. Overview

To improve the compliance and suitability of the applied ultrasonic inspections for the increasingly complex designs of industrial components, flexible ultrasonic arrays have been introduced to enable efficient inspections without the necessity for time taking and costly manufacturing of custom-designed wedges to conform to irregular surfaces. These wedges, as illustrated in Figure 2.6 (a), must be precisely engineered to match the specific curvature and geometry of each component, requiring detailed measurements and bespoke design. Thus, this can be time-consuming and expensive, particularly for components with varying diameters or non-standard shapes. Moreover, this introduces limitation in reusability, as they become incompatible with other components, lacking versatility. Multiples wedges are therefore required to allow inspection of a variety of curvatures, escalating maintenance costs [37]. Furthermore, the use of a standard rigid ultrasonic phased array probe, either alone or paired with a flat wedge to direct the acoustic beam toward the region of interest in components with complex geometries, faces significant limitations. These include difficulties in achieving contact with intricate surfaces, limitations posed by small pipe diameters, and spatial constraints arising from adjacent structures. Consequently, limited accessibility, and surface conformity, as depicted in

Figure 2.6 (b), leads to ultrasound beam distortion, reduced sensitivity, and challenges in quantitative defect analysis and evaluation [38].

(a)

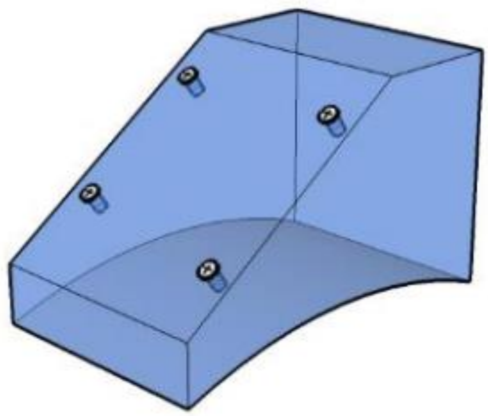

(b)

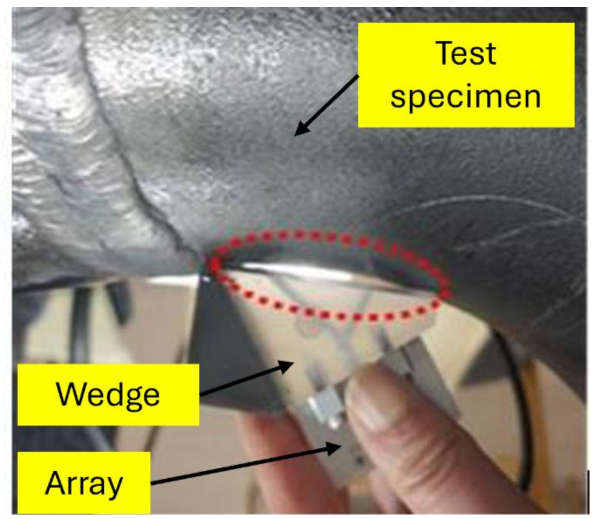

Figure 2. 6: (a) Illustration of a custom-designed wedge to fit the curvature of the outer diameter of a pipe [37]. (b) Accessibility limitation when inspecting complex-geometry components. The dashed red region highlights the difficulty in achieving surface conformity. While a custom wedge could be engineered to conform to the surface, this case highlights the requirement for multiple specialised designs and fabrication processes [38].

2.2.2. Existing Solutions

To overcome the challenges associated with custom-designed wedges, the potential of manufacturing/using flexible ultrasonic arrays to conform to and effectively inspect complex surface geometries has been investigated. For example, the Commissariat à l'énergie et aux énergies alternatives (The French Alternative Energies and Atomic Energy Commission, CEA List, Saclay, France), developed a flexible array transducer to inspect components with complex geometries, as depicted in Figure 2.7. The array comprises 24 mechanically interconnected piezoelectric elements, configured into a flexible linear array arranged with overall dimensions of approximately 50 × 20 mm, operating at a centre frequency around 2.5 MHz, and exhibiting a bandwidth of approximately 50–60%. The array elements are configured to conform to radii as small as 15 mm. The ultrasonic sensor is integrated with two complementary sub-systems: a mechanical apparatus that ensures contact of the 24 elements to the inspection surface and an instrumentation module that measures the irregular surface profile encountered by the transducer. Real-time processing of profile measurements is executed by an algorithm that computes delay laws optimised to the specific surface profile [15], [39-41].

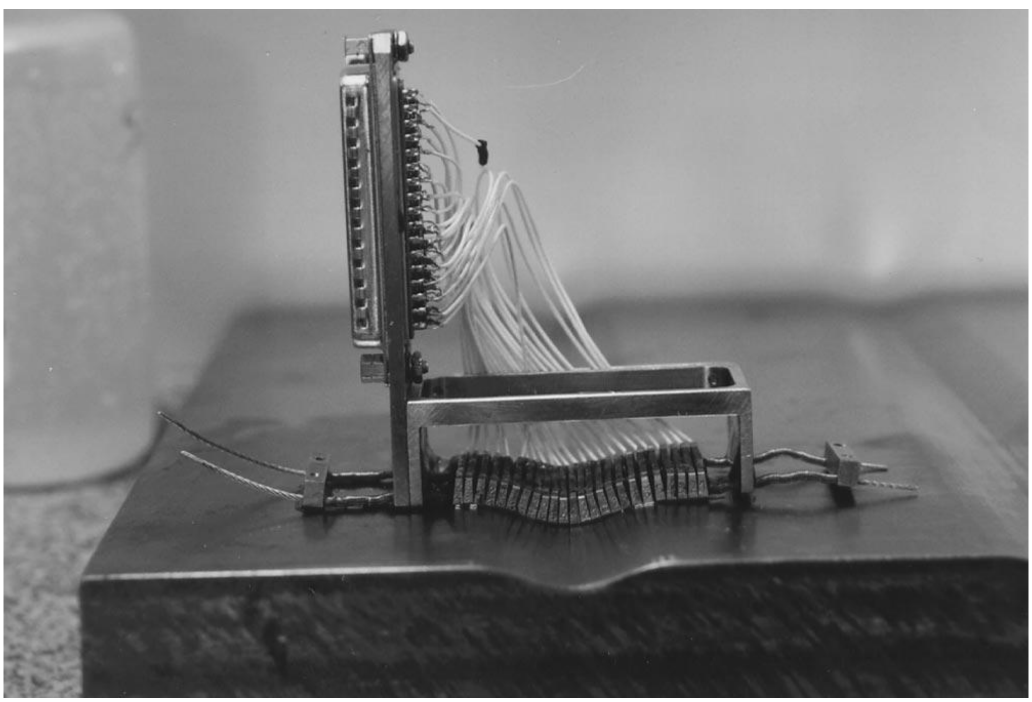

Figure 2. 7: Flexible linear array developed by the French Alternative Energies and Atomic Energy Commission [39]

The underlaying concept of these transducers, which enables real-time delay law adaption based on the precise positioning of individual elements, is protected by a patent registered with the CEA. Imasonic SAS (Voray sur l'Ognon, France) possesses the exclusive licence to utilise this patented technology for the design and fabrication of these transducers [42]. Hence, enhanced robustness and suitability for industrial applications was achieved with these transducers. Figure 2.8 shows examples of these flexible array transducers manufactured by Imasonic SAS (Voray sur l'Ognon, France) which are available commercially.

(a)

(b)

Figure 2. 8: Commercially available spring-loaded flexible ultrasonic arrays manufactured by Imasonic SAS (Voray sur l'Ognon, France) [42].

An alternative strategy to inspect components with complex geometries, developed with support from Rolls-Royce, employs a membrane-coupled phased array device. The initial method leverages the phased array for surface profiling, followed by adjusting the delay laws to conform to the variable geometry. Developed for operation with FMC acquisition, the device has undergone multiple iterations. Its second-generation design incorporates a rigid standard ultrasonic phased array with a water-filled standoff encased in a polyurethane rubber membrane. Figure 2.9 depicts a visual representation of the second-generation membrane-coupled conformable phased array device. The system incorporates a linear 80-element transducer with a 1.25 mm pitch and a 2 MHz centre frequency, integrated with a header tank arrangement to maintain consistent water pressure within the standoff. The housing is designed to improve device robustness and facilitates rapid membrane replacement [43].

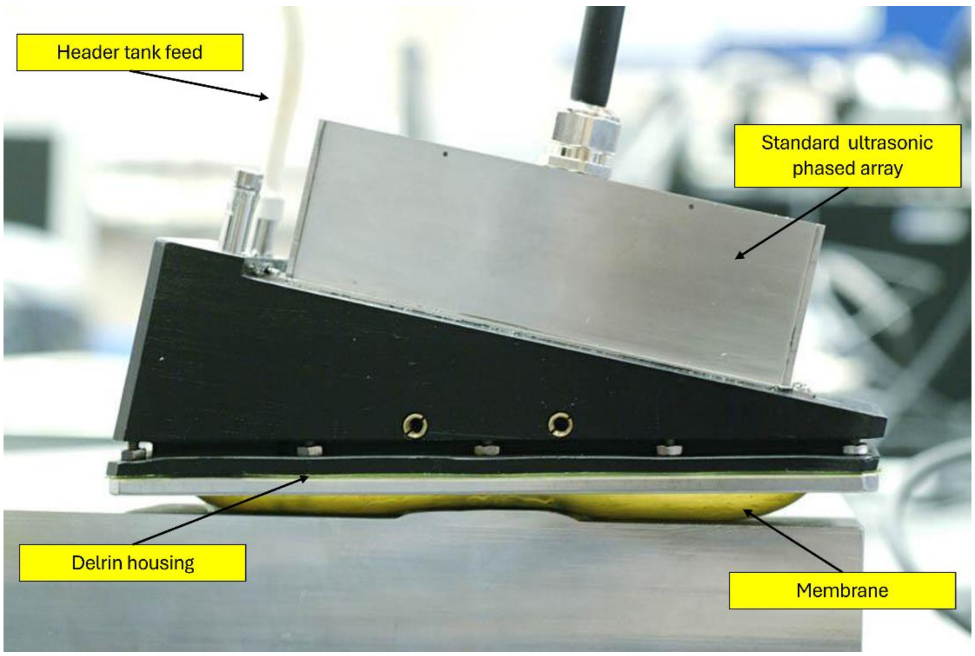

Figure 2. 9: Photograph of the second-generation membrane coupled conformable phased array device [43].

Further alternative approaches for inspecting complex components utilise low-profile ultrasonic arrays. These arrays provide numerous advantages, notably their suitability for in situ inspections in environments with restricted access. In [11], a 1-3 Lead Zirconate Titanite (PZT) composite linear ultrasonic array was employed to obtain high-resolution TFM images of defects in components with irregular surfaces. The 1-3 refers to the connectivity pattern in piezoelectric composites where piezoelectric ceramic pillars, aligned in the vertical axis, are embedded within a polymer matrix, connected in all three dimensions surrounding and supporting the piezoelectric pillars. Relative to isotropic piezoelectric ceramics, the incorporation of a polymer matrix in the 1-3 piezocomposite configuration reduces the overall density and enhances the thickness-mode vibration, which optimises the conversion of electrical energy into mechanical vibrational energy [8]. Figure 2.10 shows an illustration of a 1-3 connectivity pattern. Characterised as narrowband, the probe response operates at a peak frequency of approximately 5.5 MHz, and consists of 64 elements with a 1 mm element pitch and measures 2 mm in thickness.

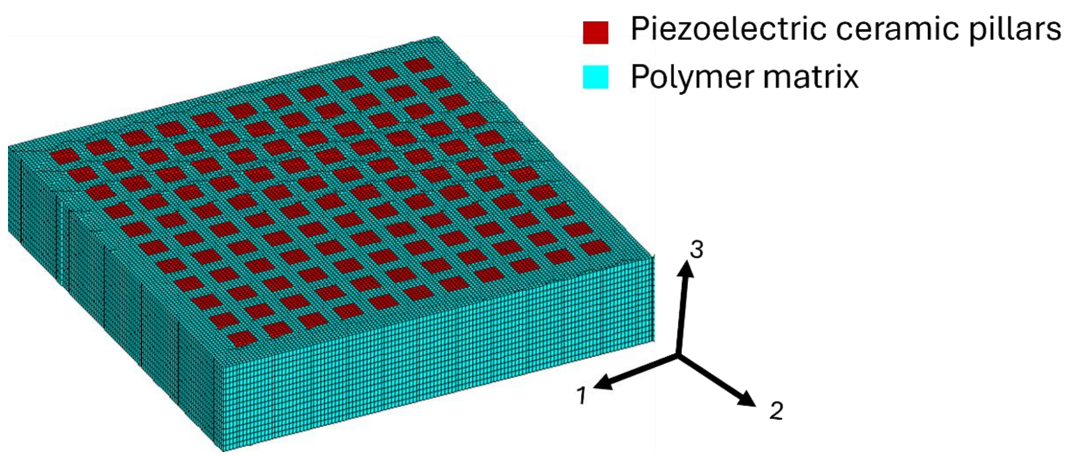

Figure 2. 10: Illustration of a 1-3 connectivity pattern in piezocomposites. The piezoelectric ceramic pillars are aligned in one direction, the vertical axis "3", and the polymer matrix is connected in all three directions, axes "1", "2" and "3".

In [9], a shape-sensing optical fibre was integrated into a low-profile 1-3 PZT composite linear flexible ultrasonic array to image a component with a curved surface. The probe features a centre frequency of 5 MHz, comprising 64 elements, with a 1 mm element pitch and a total thickness of 2 mm. It is noteworthy that all cases use a 1-3 PZT composite configuration. In relation to the isotropic PZT, the anisotropic structure of 1-3 composites offers enhanced electromechanical coupling coefficients in thickness mode, enabling efficient transduction of electrical energy into mechanical vibrations (acoustic output) [8]. Figure 2.11 displays the low-profile arrays. Furthermore, another existing solution to inspect complex structures is water jet (squirter) ultrasonic inspection. This consists of a non-contact method that uses controlled water stream to couple ultrasonic waves from the transducer to the test specimen [44].

(a)

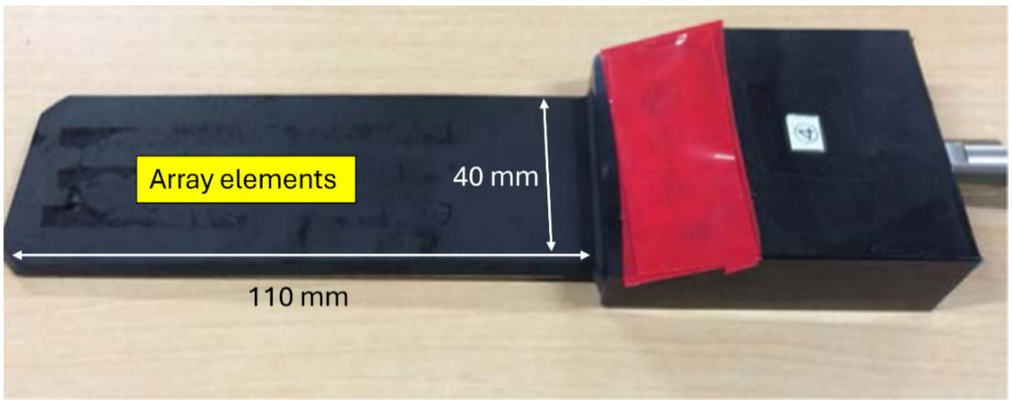

(b)

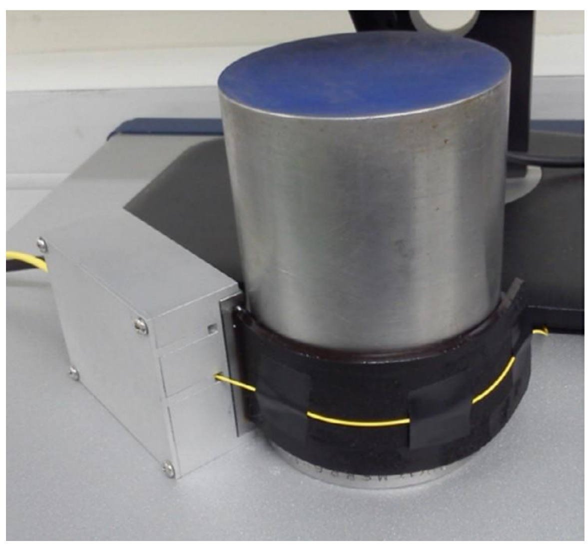

Figure 2. 11: Low-profile ultrasonic arrays employed for inspecting complex-geometry components. (a) Flexible ultrasonic array transducer as detailed in [11]. (b) Shape-sensing fibre (in yellow) integrated with the flexible ultrasonic array (in black) deployed on a cylindrical test specimen [9].

2.3. Intravascular Ultrasound

2.3.1. Atherosclerosis

Atherosclerosis is a long-term vascular disease that typically remains asymptomatic during its initial stages. It is characterised by the buildup of cholesterol, fibrous tissues, inflammatory cells, and monocytes in arterial walls, resulting in progressive narrowing and stiffening of the arteries [45, 46]. In the management of coronary artery disease, Percutaneous Coronary Interventions (PCI) are a common therapeutic approach, utilising minimally invasive catheter-based ballon dilatation and subsequent stent deployment to re-establish arterial patency and enhance blood flow [45, 46]. Figure 2.12 shows an illustration of this approach.

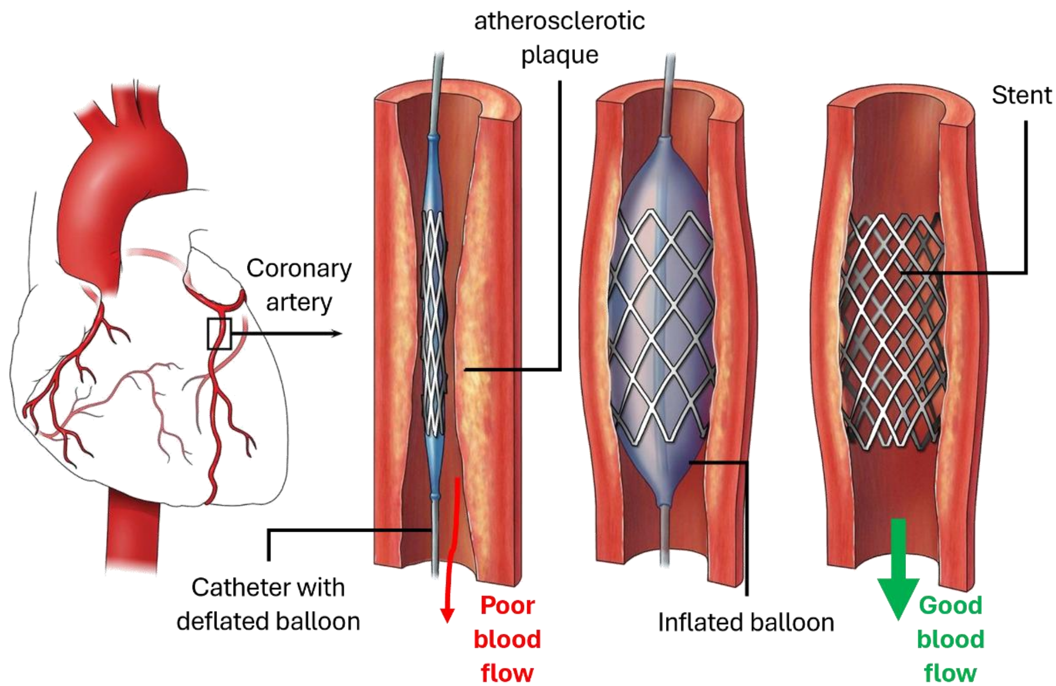

Figure 2. 12: Illustration of the PCI approach [47]. The procedure is designed to restore optimal blood flow by reopening blocked coronary arteries. The illustration

highlights a catheter-mounted deflated balloon positioned at the site of atherosclerotic plaque-induced narrowing within a coronary artery. The balloon is then inflated to deploy a stent, expanding the artery, thereby re-establishing good blood flow.

2.3.2. Overview of Intravascular Ultrasound

Intravascular Ultrasound (IVUS) currently serves as a pivotal diagnostic modality for the comprehensive assessment of Coronary Artery Disease (CAD), offering detailed insights into the pathophysiology of coronary lesions. This advanced imaging method allows clinicians to meticulously evaluate the morphology of atherosclerotic plaques within the coronary arteries, thereby facilitating diagnosis and treatment planning. By providing real-time, high-resolution cross-sectional images of the arterial wall, IVUS plays an essential role in guiding PCI, ensuring optimal stent deployment, and assessment of post-procedural outcomes, as documented in multiple studies [27, 16], [48-51]. IVUS employs a catheter-mounted transducer to generate detailed visualisation of the coronary vessel wall and atherosclerotic plaques, delivering important information about the coronary arteries, including the degree of luminal stenosis, the structural characteristics of the vessel wall, and compositional attributes of the plaques, such as their calcific, fibrous, or lipid-rich nature [46, 52, 53]. Moreover, the integration of IVUS into PCI procedures has been associated with substantial clinical benefits, notably a remarkable 50% decrease in cardiovascular mortality following the procedure, as evidenced by prior research [45, 54]. Additionally, its widespread clinical adoption is underscored by its integration into over 85% of PCI procedures in Japan, reflecting its significant importance in modern interventional cardiology practices [27]. This further reinforces that IVUS has solidified its position as an indispensable tool in the management of coronary artery disease, with demonstrated contributions to improved patient survival and procedural success across diverse healthcare settings.

2.3.3. System Components

An IVUS diagnostic system is primary composed of three essential components: an imaging catheter, a Motor Drive Unit (MDU), and a controller. The imaging catheter is equipped with an ultrasound transducer that radially emits ultrasonic signals, typically operating within a frequency range of 10 to 60 MHz to capture detailed images of coronary vasculature. The MDU facilitates precise catheter rotation and pullback, ensuring stable and controlled movement to acquire sequential cross-sectional images. The controller processes raw ultrasound data, converting it into high-resolution, real-time images displayed for clinical interpretation [27]. IVUS systems employ two conventional catheter configurations (Figure 2.13) utilised in clinical practice. The first uses a mechanically rotating transducer probe, where a single-element transducer (generally spanning $0.33 \times 0.33\, mm^2$ to $0.5 \times 0.5\, mm^2$ in aperture [16]), driven by the MDU, rotates to emit and receive ultrasound signals at approximately $1°$ increments. The second configuration is the electronically switched multi-element array transducer (typically comprising 64 elements [46, 48], with diameters ranging from 0.9 – 1.2 mm, enabling deployment through standard 5 or 6 French gauge guiding catheters, as dictated by clinical requirements [54]), which activates individual elements within the array transducer using precise time delays to achieve radial scanning [54, 55, 27, 51].

(a)

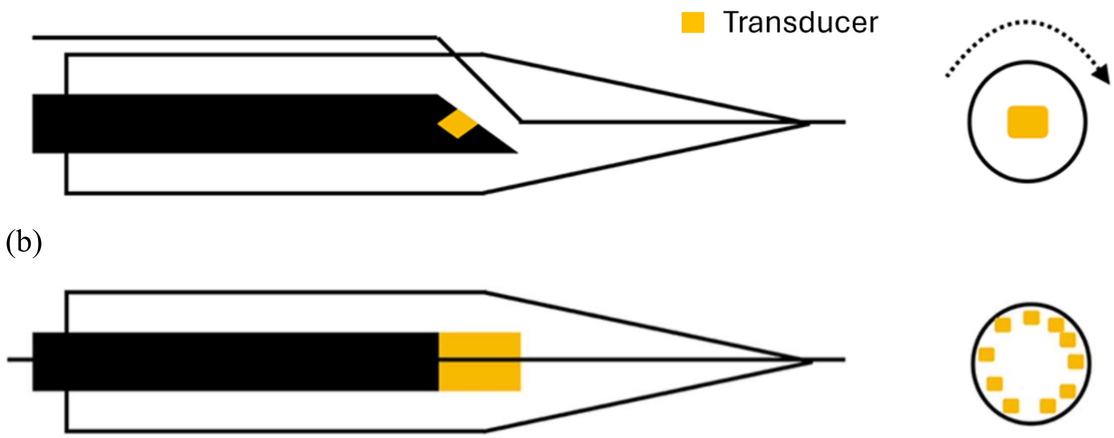

(b)

Figure 2. 13: Conventional catheter configurations used in IVUS systems [54]. (a) The mechanical-rotating catheter with a single-element transducer. (b) The electronic-scanning catheter with the multi-element array transducer sending phased ultrasonic pulses.

2.3.4. Considerations of Transducer Materials in Catheters

Piezoelectric transducers, most notably those based on Lead Magnesium Niobate-Lead Titanate (PMN-PT), continue to dominate commercial IVUS catheter designs due to their superior piezoelectric and electromechanical properties. However, the incorporation of lead in these materials poses significant environmental challenges and raises human health concerns associated with toxicity and bioaccumulation. These issues underscore the urgent necessity for sustainable, lead-free alternatives to mitigate ecological impacts and ensure safer clinical applications while maintaining the high-resolution imaging capabilities essential for effective coronary disease assessment [17, 16]. The adoption of lead-free alternatives is both essential and timely, aligning with global regulatory frameworks such as the Restriction of Hazardous Substances (RoHS) directive [2-4], alongside analogous legislation in China and Japan. These initiatives underline the pressing need to advance environmentally sustainable piezoelectric materials, fostering the development of eco-friendly technologies that mitigate the health and environmental risks associated with lead-based materials while supporting the continued evolution of high-performance medical imaging systems. Despite extensive research over the past two decades on the piezoelectric properties of lead-free materials, significant obstacles persist in translating these scientific advancements into scalable, commercially viable production processes. These challenges encompass optimising material performance to match or exceed lead-based counterparts, ensuring cost-effective manufacturing at scale, and maintaining consistent quality and reliability. Moreover, high raw material costs arise from specialised compositions and complex fabrication processes, while limited global supply chains constrain availability [5-7].

2.4. Zinc Oxide-Based Ultrasonic Transducers

A novel manufacturing method has been developed to enable scalable fabrication of high-frequency, lead-free, flexible ultrasonic array transducers. This innovative approach leverages advanced processing techniques to achieve precise control over thickness, composition and scalability, aligning with the growing demand for environmentally sustainable piezoelectric technologies in applications such as NDT and medical imaging, while overcoming the limitations of traditional lead-based transducers. The ultrasonic arrays introduced in this work utilise Zinc Oxide (ZnO) as its piezoelectric material, manufactured via a sophisticated thin-film deposition process. As a lead-free and environmentally sustainable thin-film material, ZnO represents a widely adopted alternative in the development of next-generation ultrasonic devices. Alongside aluminium nitride (AlN), it is among the most extensively explored thin-film piezoelectric materials. The intrinsic resonant frequencies of piezoelectric thin-films, typically 1 GHz, render them unsuitable for ultrasonic medical imaging and NDT applications that typically require much lower operational frequencies. By integrating a thin, flexible metallic substrate, in conjunction with mass loading to the piezoelectric film, lower operating frequencies (to below 50 MHz) were attained. This advancement improves the practical deployment of these lead-free materials for a wide range of applications, including medical imaging and NDT [1, 18, 20].

Figure 2.14 shows two ZnO-based arrays employed for industrial and medical settings, respectively. In Figure 2.14 (a), a commercial low profile, flexible linear ultrasonic array (Novosound Ltd., Motherwell, Scotland), capable of conforming to complex-geometry components is depicted. Characterised as wideband, with approximately 60% of -6 dB bandwidth, the probe features a centre frequency of 20 MHz, consisting of 64 elements, with 1 mm element pitch, 5 mm elevation, a total thickness of 0.5 mm, and a bend radius of 5 mm. Figure 2.14 (b) shows a multi-element ultrasonic array transducer, constructed using a 3D-printed composite resin tube as the inner core. The tube was secured in place via epoxy bonding, resulting in a compact diameter of 5 French gauge, approximately 1.67 mm. This design optimises the flexibility of the transducer and miniaturisation, making it suitable for integration into minimally invasive intravascular applications. This configuration facilitates radial scanning by selectively activating individual array elements with programmable time delays. The array comprises 32 elements, with an element pitch of $163\ \mu m$ and an elevation of 3.82 mm.

(a)

(b)

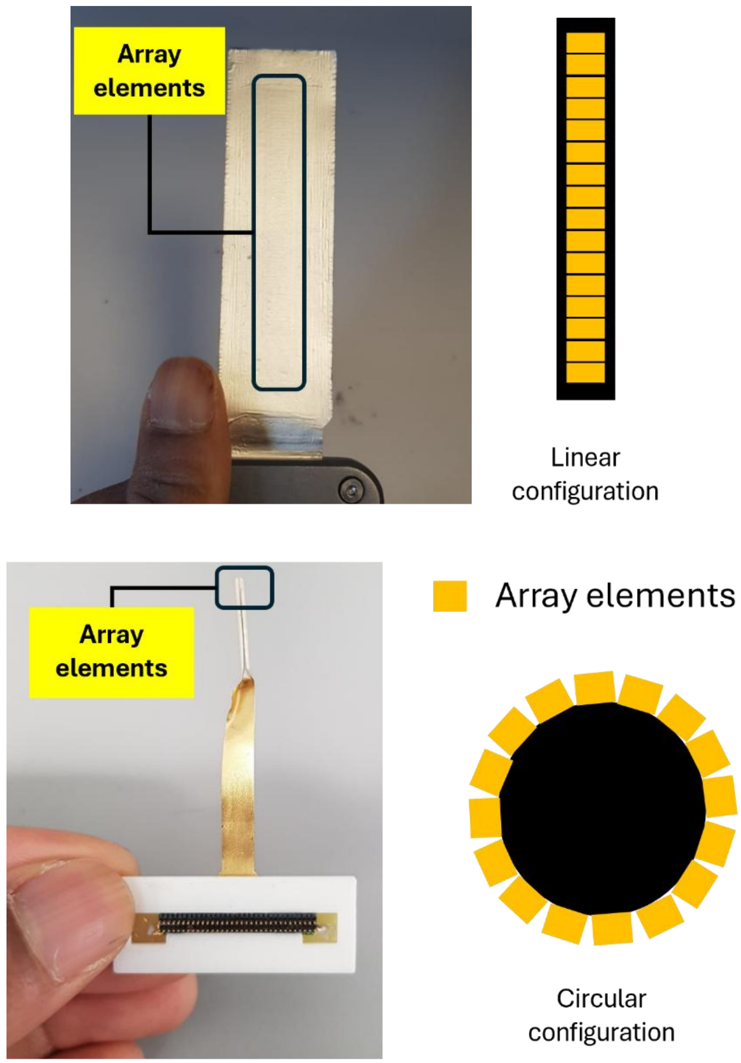

Figure 2. 14: Photograph of Zinc Oxide-based ultrasonic arrays. (a) Commercial low profile (0.5 mm in thickness), flexible (5 mm bend radius) linear ultrasonic array employed to inspect industrial components with complex geometries. The array elements arranged in a linear configuration. (b) Multi-element ultrasonic array capable of performing radial scanning, and employed to image coronary vessel wall and plaques. The array elements arranged in a circular configuration.

2.5. Ultrasonic Excitation Strategies

2.5.1. Modulated Signals

The signal excitation trade-off between axial resolution, fundamentally determined by the bandwidth of the transducer, and penetration depth is well established in ultrasound imaging. Short-cycle pulses, as illustrated in Figure 2.15 (a), deliver reduced energy into the medium, thereby achieving superior axial resolution due to their ability to resolve closely spaced targets. However, this comes at the cost of limited penetration depth, as the reduced transmitted energy restricts the ability of the ultrasound beam to propagate deeper into the medium due to elevated noise floor. Conversely, multi-cycle pulses, as depicted in Figure 2.15 (b), with longer durations impart greater energy into the medium, facilitating improved penetration depth, enabling imaging deeper targets into the medium. This increased penetration, however, compromises axial resolution, as the longer pulses diminishes the ability to distinguish fine structural details [56].

(a) (b)

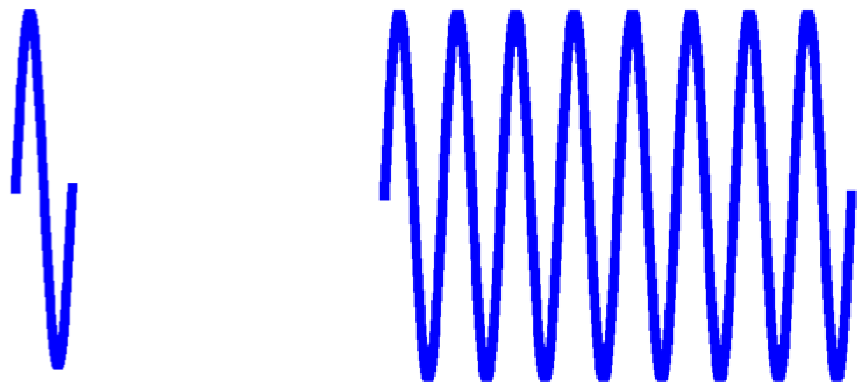

Figure 2. 15: Traditional signal excitation trade-off in ultrasound imaging between axial resolution and penetration depth. (a) One cycle representing a short pulse. Less energy is transmitted, achieving good axial resolution and poor penetration depth. (b) Eight cycles representing a long pulse. More energy is transmitted into a medium, attaining poor axial resolution and good penetration depth.

The limitations imposed by the inherent signal excitation trade-off between axial resolution and penetration depth can be effectively mitigated through the use of coded excitation in combination with pulse compression methods. By employing longer coded signals, which encode specific patterns, a greater amount of acoustic energy can be transmitted into the medium, improving penetration depth. Upon reception, these signals undergo compression, a process that shortens their duration. This enables the simultaneous achievement of high axial resolution, comparable to that of the short-cycle pulses, and improved penetration depth, similar to that of the longer multi-cycle pulses. Consequently, coded excitation, in conjunction with pulse compression, expands the conventional operational limits of ultrasound systems [56-60]. Coded excitation techniques have been extensively explored to enhance the signal quality across diverse applications, including radar [61-64], medical imaging [65-75] and NDT [76-84]. For instance, in radar research,

[62] proposed a coded excitation approach that improved the depth resolution of thermal wave radar in relation to conventional methods. Moreover, in a medical imaging study, [72] used coded excitation methods in transcranial imaging across ten adult participants, demonstrating a mean SNR improvement of 17.91 ± 0.96 dB. Furthermore, [84] investigated the use of coded excitation, in an NDT study, as a means to preserve SNR under conditions of significant signal attenuation. These methods are broadly categorised based on the number of transmissions (single or multiple), and the modulation strategy employed, which may involve either phase or frequency modulation. In single-transmission coded excitation schemes, a single, carefully designed code sequence is employed, inherently possessing the desired pulse compression properties. In contrast, multiple-transmit coded excitation strategies rely on the transmission of two or more distinct code sequences, which must be collectively processed and combined to achieve effective pulse compression. Table 2.1 shows phase and frequency coding strategies. The typical phase codes are Barker and Golay with code symbols ± 1, and the most common frequency code is chirp [56]. M-sequences are single-transmission phase codes that have also been reported in literature [56]. The details on the specific modulated signals used in this work, along with the construction process, considering each application (industrial or medical) and the parameters of the ultrasonic array utilised, will be discussed in chapters 3, 4, and 5.

Table 2. 1: Types of codes in coded excitation.

Type	Single transmission	Multiple transmissions
Frequency	Chirp	-
Phase	Barker, M-sequence	Golay

2.5.2. Pulse Compression

Pulse compression techniques leverage temporally-extended modulated excitation signals to concentrate or compress the received acoustic energy into a shorter time window. By employing carefully designed, longer duration signals with specific modulation patterns, this approach allows for increased energy transmission into the medium, without sacrificing axial resolution [84]. The modulated excitation signals (phase or frequency) possess favourable compression properties. The decoding filter, commonly a matched filter, is designed to temporally compress the received signal into a short time interval. Figure 2.16 illustrates the pulse compression principle. A long-modulated chirp signal is presented and used for excitation, allowing increased energy in transmission. Pulse compression occurs when the received signal, $R(t)$, is convolved with a compression filter, $F_c(t)$. In this case, the compression filter employed was a matched filter (time-reversed modulated excitation signal), compressing the signal in time. A matched filter is designed to maximise the SNR for optimal signal detection, irrespective of the specific modulation signal employed. Alternative compression filters exist. For example, mismatched filters, consisting of the time-reversed excitation signal weighted by a Chebyshev window, have been investigated as a strategy to suppress axial sidelobes, which can degrade image quality. However, this improvement is accompanied by a trade-off, as mismatched filtering typically results in a broadened mainlobe, which compromises axial resolution compared to that achievable with matched filtering [56, 85].

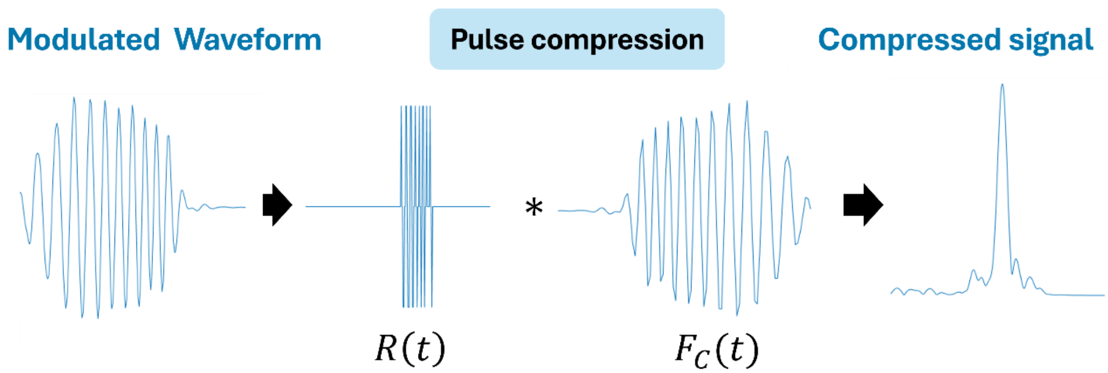

Figure 2. 16: Pulse compression principle. The modulated signal used for excitation is a chirp waveform. Pulse compression occurs through a matched filter, compressing the received signal to a short time interval.

2.6. Ultrasonic Data Presentation

The data acquired by the receiving element in a transducer can be presented to a user in diverse formats and levels of complexity, tailored to meet specific application requirements or to facilitate enhanced interpretation. Frequently, these data representations are integrated to create novel imaging modalities or customised for particular use cases. Several such approaches, which are widely employed across various ultrasound applications, are elaborated in the subsequent sections to provide foundational insight into the principles of ultrasound inspection. Moreover, more advanced techniques for post-processing and data visualisation enabled by ultrasonic arrays are also discussed.

2.6.1. A-scan

The term A-scan, short for amplitude scan, represents the most fundamental and straightforward method for presenting received ultrasound data, offering a one-dimensional profile of the received signal. Specifically, this format displays the amplitude of the reflected/scattered ultrasonic energy as a function of time, typically measured in microseconds. The majority of the ultrasound instruments designed to present A-scan data offer the capability to display the received signal in its unprocessed, raw form as a Radio Frequency (RF) waveform [86]. The time-domain signal typically contains distinct peaks, which correspond to echoes reflected from internal features within the medium. The temporal positions of these peaks can be utilised to calculate the depth of these features by leveraging the calibration process and gaining the knowledge of the wave propagation time to arrive at known features and bulk acoustic velocity of the material. This relationship allows for localisation of structural variations, based on the time it takes for the ultrasonic wave to travel to and reflect back from these features to return to source. An example of an A-scan in its raw RF format with added random noise is illustrated in Figure 2.17. This response corresponds to a reflection from a simulated single-point target, modelled as an ideal, dimensionless, scatterer as defined by the simulation software parameter.

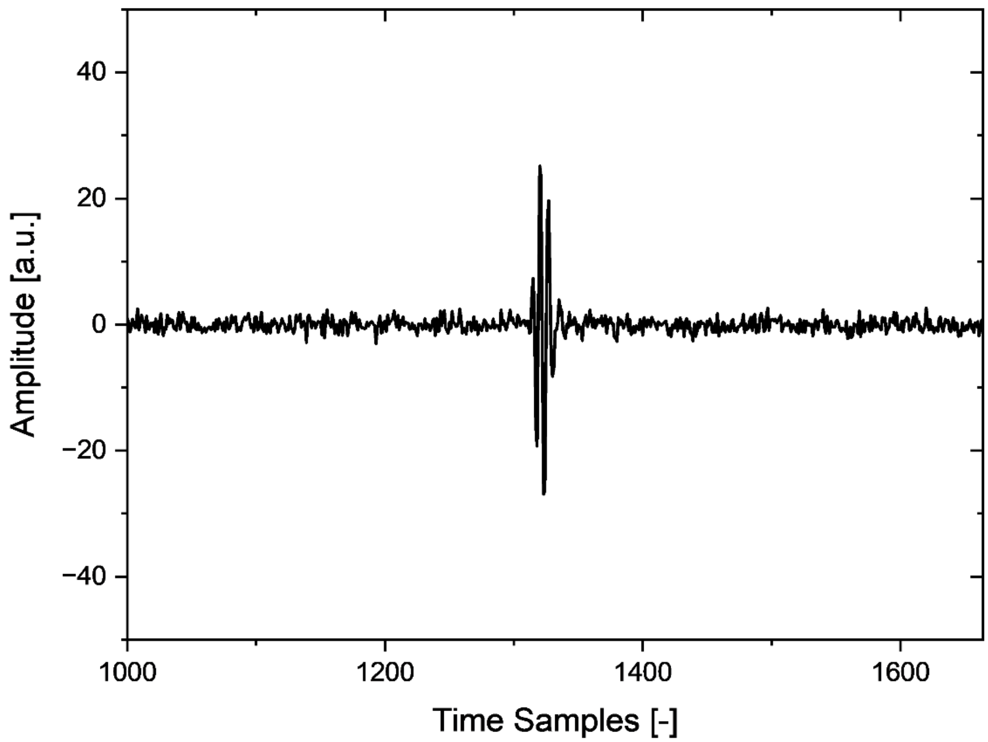

Figure 2. 17: Example of an amplitude scan on its raw RF format.

2.6.2. B-scan

The B-scan, an abbreviation for brightness scan, refers to a two-dimensional representation of aggregated ultrasonic A-scan data. While a single-element transducer requires mechanical scanning to produce a B-scan image, an array transducer only requires electronic scanning for image formation. Mechanical scanning involves physically moving the single-element transducer to cover the region of interest, leading to reduced imaging speeds. Electronic scanning leverages multiple elements in an array transducer, activated in a precisely controlled sequence to steer and focus the ultrasound beam without mechanical motion, thereby facilitating higher scanning speeds. Typically, the horizontal axis denotates the lateral position (reflecting the spatial progression of the ultrasound probe, for the single-element transducer case) while the vertical axis represents the ultrasonic path length or time-of-flight. Depending on the specific requirements of the application, the orientation of these axes can be inverted to optimise the display for improved interpretability. Fundamentally, a B-scan is constructed by compiling a series of A-scans, each capturing the amplitude of the reflected ultrasonic pulses at successive positions, effectively stacking these one-dimensional signals to form a cohesive cross-sectional image [86].

For ultrasonic arrays, B-scans can be visualised in various formats, depending on the scanning methodology employed to acquire the underlying A-scan data. The simplest approach is the electronic scanning, where a two-dimensional image is generated through the linear translation of an element or a group of elements across the array transducer. This technique leverages sequential activation of array elements to capture a series of A-scans. The ultrasonic beams in such scans can be electronically focused and steered to target specific regions, improving image resolution. However, electronic scans are frequently employed to image a region of interest directly beneath the array, as depicted in Figure 2.18 (a). The setup employed a 64-element ultrasonic array coupled to a type B steel calibration block to image side-drilled holes (SDHs), using a focused sub-aperture of 16 elements during the scanning process [31]. The second type of B-scan, known as sector scan, typically employs the full aperture of the array transducer to transmit ultrasonic beam across a range of angles, enabling a comprehensive imaging of a sectorshaped region within the medium, as depicted in Figure 2.18 (b). To enhance beam steering, sector scans frequently incorporate a physical angled wedge in NDT applications. The wedge positions the array transducer at an inclined angle relative to the surface of the specimen, thereby optimising directionality of the ultrasonic beam and improving the detection of features. In this configuration, a 64-element ultrasonic array coupled to a 55° shear wedge was employed to transmit shear ultrasonic beams at angles spanning from 10° to 75°, facilitating the imaging of SDHs in an ASTM E2491 phased array assessment block constructed from 1018 steel [31].

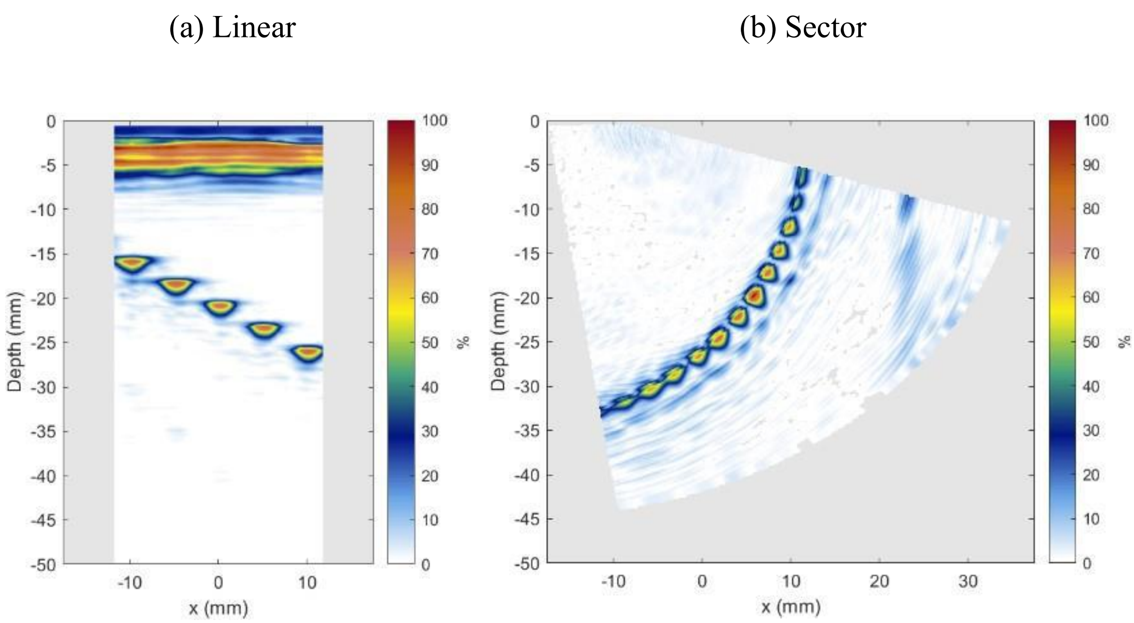

Figure 2. 18: B-scan in two different formats. (a) Linear scan. (b) Sector scan [31].

2.6.3. C-scan

A C-scan provides a top-down, two-dimensional visualisation of the test specimen, representing a planar slice parallel to the sample surface. A C-scan image can be generated by systematically acquiring B-scan data at regular spatial intervals across the sample. C-scans represent the results of an ultrasonic examination as a two-dimensional image depicting a cross-sectional view of the test specimen, oriented parallel to the scanning surface. However, unlike a singular cross-sectional slice, C-scans often integrate measurements acquired across the entire thickness of the specimen, providing a comprehensive top-down map of internal features [31, 32, 86, 87].

2.6.4. Full Matrix Capture and Total Focusing Method

The fundamental methods for presenting ultrasonic data, namely A-scans, linear B-scans, and C-scans, as previously described, are equally applicable to array probes as they are to single-element probes. However, the enhanced versatility provided by array probes extends beyond the conventional data presentation strategies of A-scans, linear B-scans, and C-scans, enabling a broader range of advanced imaging techniques. Ultrasonic arrays enable precise electronic focusing and steering of the acoustic beam, allowing targeted interrogation of specific regions within a sample.

Advancements in phased array technology have enabled the selective or concurrent excitation of individual array elements during both ultrasonic transmission and reception, an essential capability underpinning the implementation of Full Matrix Capture (FMC) acquisition. This technique involves capturing the complete set of time-domain signals from every possible transmitter-receiver pair within the array. Each element of the array transducer is sequentially activated to transmit an ultrasonic pulse, while all elements simultaneously serve as receivers for each transmission event. This process is iterated until every element in the array has transmitted once, generating a comprehensive matrix of time-domain signals that capture all possible transmit-receive pair of combinations across the array. For example, in an array comprising N elements, the FMC process generates N^2 A-scans per frame. The FMC comprehensive dataset offers significant advantages over conventional phased array ultrasonic testing (PAUT), as most PAUT imaging can be synthetically reconstructed through post-processing. However, this benefit comes at the cost of slower acquisition and data transfer rates due to the large volume of data, along with computationally intensive post-processing requirements, which may pose challenges for real-time applications. The FMC acquisition facilitates the application of a number of imaging algorithms during post-processing. The Total Focusing Method (TFM), widely recognised as the gold standard in post-processing algorithms in ultrasonic imaging, represents an advanced imaging technique that capitalises on the comprehensive dataset acquired through FMC. The algorithm computes the propagation path length from each transmitting element to every pixel and subsequently from each pixel to every receiving element. The FMC-TFM imaging technique, an amplitude-based delay-and-sum approach, provides uniform full-aperture focusing during both transmission and reception at every point within a discretised imaging region [88, 89]. A schematic representation of the TFM is provided in Figure 2.19.

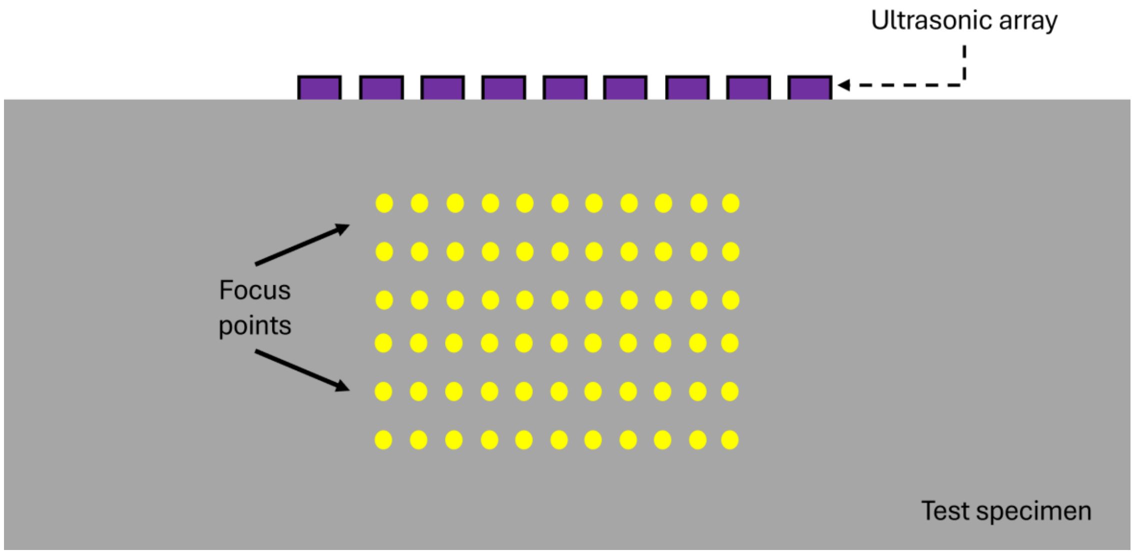

Figure 2. 19: Schematic illustration of the TFM

The intensity of the image, $I(x, z)$, at any point can be expressed as presented in Equation 2.6. The coordinate x denotates the direction along the ultrasonic array, while the z-axis corresponds to the propagation direction, extending into the sample. This results in high-resolution image reconstruction with improved sensitivity to features [88, 89].

$$I(x,z) = \left| \sum_{tx=1}^{N_{tx}} \sum_{rx=1}^{N_{rx}} h_{tx,rx}\left(\frac{\sqrt{(x_{tx}-x)^2+z^2}+\sqrt{(x_{rx}-x)^2+z^2}}{c_l} \right) \right| \quad (2.6)$$

where c_l represents the estimated constant longitudinal wave speed in the test specimen, x_{tx} and x_{rx} consist of the x-coordinates of the transmit and receive array elements, respectively. The complex Hilbert transform of the time-domain signal transmitted from element tx to element rx is denotated as $h_{tx,rx}$. N_{tx} and N_{rx} are vectors containing the active element numbers for the transmit and receive elements, respectively.

2.6.5. Hilbert Transform Considerations

The Hilbert transform is a mathematical operation commonly used to extract the envelope of ultrasonic signals, thereby facilitating the analysis of amplitude variations over time and enabling clearer visualisation of features. For an A-scan signal $s(t)$, derived from an FMC dataset, it represents the real component of a complex analytical signal $c(t)$, which can be expressed as shown in Equation 2.7 [90, 31].

$$c(t) = s(t) + is'(t) = |c(t)|e^{i\theta(t)} \tag{2.7}$$

where $s'(t)$ represents the imaginary component of the analytical signal $c(t)$, while $\theta(t)$ denotates its instantaneous phase. The signal envelope is defined as the magnitude (or norm) of the complex analytical signal, and is expressed in Equation 2.8 [90, 31].

$$|c(t)| = \sqrt{s(t)^2 + s'(t)^2} \tag{2.8}$$

Figure 2.20 presents an exemplar A-scan signal $s(t)$, experimentally acquired via FMC. The real component of the signal $s(t)$ is depicted in black, while its imaginary component $s'(t)$, derived through the Hilbert transform, is shown in red. The resulting signal envelope, represented as the magnitude $|c(t)|$ of the complex analytical signal, is illustrated in blue. As indicated by Equation (2.8), the envelope $|c(t)|$ remains independent of the instantaneous phase $\theta(t)$ of the signal.

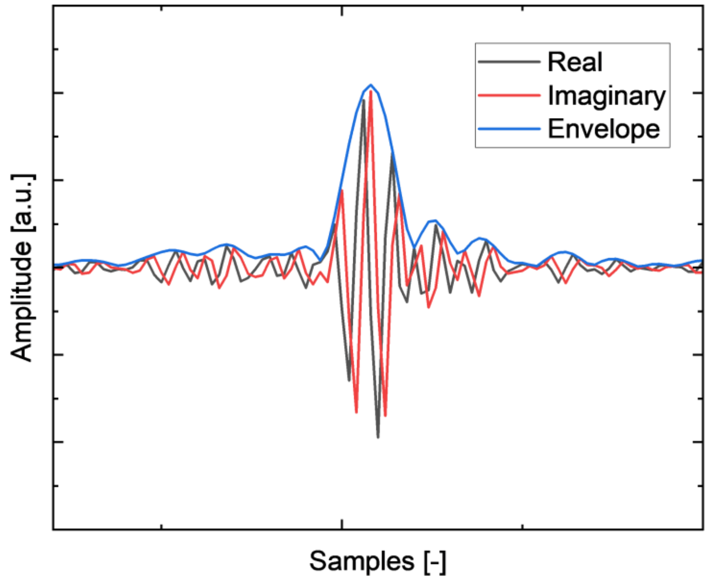

Figure 2. 20: A-scan signal example, acquired through FMC experimentally. The real, the imaginary and the envelope are highlighted.

The Hilbert transform is an essential tool in the processing of ultrasonic data for imaging applications. Figure 2.21 presents a TFM image of an SDH, comparing reconstructions with (part b) and without (part a) the application of the Hilbert transform. The use of the signal envelope significantly improves the clarity of the feature visualisation. This approach helps minimise interpretation errors in ultrasonic imaging, as the intermittent response of the non-analytic signal image can be erroneously identified as complex features such as multi-faceted cracks or porosity, leading to inaccurate characterisations. By extracting the magnitude of the complex analytical signal, the Hilbert transform ensures a more robust and interpretable visualisation of features, enhancing diagnostic accuracy in settings including NDT and medical imaging. Accordingly, unless otherwise specified, the Hilbert transform is applied as a standard procedure for image generation throughout this work. In practical implementation, the signal envelope is computed following the completion of the imaging process to preserve phase information during the focusing stage.

(a) Without Hilbert envelope (b) With Hilbert envelope

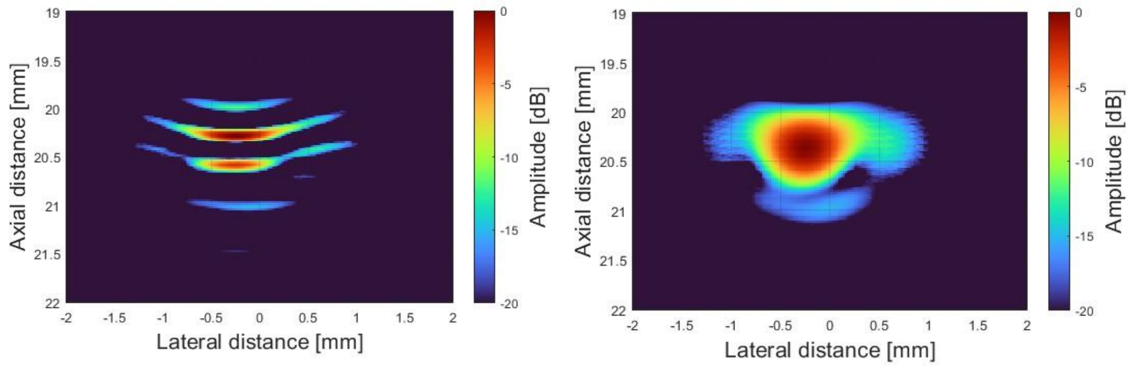

Figure 2. 21: TFM imaging of a SDH. (a) TFM image without the Hilbert envelope. (b) TFM image with the Hilbert envelope.

2.7. Conclusion

Chapter 2 has provided essential background information for the findings presented in the subsequent chapters while also establishing the rationale for the overall research. Sub-section 2.1 presented the fundamentals of ultrasonic inspection, with details on piezoelectricity, wave propagation, attenuation and ultrasonic transducers, including single-element and arrays. Sub-section 2.2 discussed the considerations on the inspection of complex components, where flexible ultrasonic arrays were explored to allow efficient inspections. Current solutions include a flexible linear array developed by CEA List, with Imasonic SAS holding the exclusive licence to employ this patented technology for the design and manufacture of such transducers. Alternative inspection strategies employed a membrane-coupled phased array device developed with support from Rolls-Royce. Further alternative approaches utilised low-profile ultrasonic arrays and water jet ultrasonic inspection systems. In sub-section 2.3, the background on IVUS was presented, with details on atherosclerosis, an overview of IVUS, its system components, and considerations of transducer materials in catheters. Sub-section 2.4 provides information on the ZnO-based transducers used in this work. This encompassed description on the manufacturing method and the two array configurations employed in this study. The ultrasonic excitation strategies are detailed in sub-section 2.5, with information on modulated signals and pulse compression techniques. Sub-section 2.6 shows different data presentation options with considerations of the Hilbert transform at the end. The subsequent chapters build on the comprehensive background to apply coded excitation combined with imaging techniques using the ultrasonic arrays presented for inspection of industrial components and IVUS settings.

Chapter 3

Golay-Based Total Focusing Method for Inspection of Thick Non-Planar Industrial Components

3.1. Chapter Overview

The compromise between axial resolution and penetration depth in ultrasound imaging poses a challenge for high-frequency ultrasonic arrays, limiting their ability to effectively inspect thick components in industrial applications. In this chapter, a commercial 20 MHz, 64 element, 1 mm pitch lead-free flexible linear array was characterised in terms of its performance. The array was subsequently evaluated using Golay-coded excitation techniques to enhance the SNR and operability on non-planar thick components. The SNR improvement verification results were acquired with the array deployed on a 100 mm thick flat aluminium test specimen. The imaging strategy employed a combination of FMC and TFM to assess the performance variations between the conventional pulse excitation and Golay-coded excitation. The Golay-based TFM demonstrated superior performance compared to the conventional pulse-based TFM, with an SNR improvement of 4.95 dB when using the full array aperture to inspect the non-planar steel S355 specimen. A sub-aperture selection approach, based on the effect of the array element beam spread, offered additional SNR improvement of up to 8.2 dB. Greater imaging penetration depth was achieved, with an increase of >40 % compared to conventional pulse-based TFM. Thus, for inspection of thick non-planar industrial components using a lead-free high-frequency array, Golay-coded excitation schemes show excellent potential to enhance SNR, penetration depth and imaging quality.

3.2. Introduction

High-frequency ultrasonic arrays have gained significant attention in recent years due to their ability to provide images with superior spatial resolution, offering higher sensitivity to small targets in non-destructive testing (NDT) and medical imaging applications [91-93]. In NDT, for instance, these arrays enable the detection of defects in materials or structures at earlier growth stages as compared to lower frequency counterparts. Conversely, high-frequency sound waves have limited penetration depth which can hinder the inspection of thick components.

The growing complexity of industrial components has driven development of conformable ultrasonic probes that enable efficient inspection without the necessity of custom-designed wedges. In line with this development, with considerations for medical contexts, flexible ultrasonic arrays have been investigated for their ability to examine complex and intricate surfaces [8-15]. For instance, the effectiveness of a flexible lead-based 2-D array in inspecting both flat and non-planar test specimens has been demonstrated [8].

Additionally, FMC and TFM imaging strategies with a flexible lead-based linear array have been utilised to detect flaws in planar and complex-geometry aluminium specimens [11].

Research is ongoing into lead-free alternatives to lead zirconate titanate (PZT), the most widely used piezoelectric material because of its high performance, to comply with the Restriction of Hazardous Substances (RoHS) regulation set by the European Union [2-4] and similar legislations in China and Japan, as well as environmental concerns. Although many promising results of the piezoelectric properties of lead-free materials have been reported over the last two decades, it is still challenging to transfer to large-scale production [5-7]. Achieving optimal ultrasound imaging using lead-free materials continues to pose a persistent challenge, particularly with respect to transducer sensitivity.

The constraints of traditional probe technology in the NDT industry, particularly regarding material composition, flexibility and operational frequency, have driven the development of a new manufacturing approach. This technique enables the production of a high-frequency, lead-free, flexible, linear ultrasonic array, allowing it to adapt to non-planar shapes commonly encountered in nuclear, aerospace, and other industries [94, 95]. A pliable metal substrate is the core material of the array. Using vacuum deposition methods, a piezoelectric thin film material is subsequently applied onto it. This enables precise management of thickness, composition, and scalability for large-scale, cost-effective production [1, 18, 20]. The practical operation of the array has been showcased [18], in which experiments were undertaken using steel tubing and industrial samples that featured common curvatures encountered in real-world structures.

The benefits of using coded excitation strategies have been demonstrated [82, 83, 85] [96-98]. Higher sensitivity was observed in defect detection when imaging thick carbon fibre reinforced polymer samples with traditional NDT arrays [82]. Moreover, the most common strategies to maintain the signal-to-noise ratio (SNR) in challenging applications are either to reduce the frequency of the ultrasound array or to average the results over multiple transmissions. However, these approaches compromise resolution and acquisition rate, respectively [19]. In coded excitation schemes, the prevalent techniques for phase modulation include Golay and Barker, while the commonly employed method for frequency modulation is based on chirp signals [56]. For the scope of this study, Golay complementary sequences (GCS) will be exclusively examined, as they minimise anomalous effects from the inverse processing [56].

This chapter presents novel work on the combination of coded excitation schemes with high-frequency, lead-free, flexible ultrasonic arrays. This improves the SNR and penetration depth, allowing the inspection of thick components, especially those with intricate surface geometries. The remaining organisational structure of this chapter is as follow: Section 3.3 presents the methodologies of the flexible array characterisation, followed by the inspection study, which included information on the phased-array controller, theoretical information of the phase-modulated Golay-coded excitation and details about the imaging strategy adopted. The experimental results and discussions are detailed in Section 3.4. The performance of the array was evaluated, comparative analysis in axial resolution at two different frequencies was performed, changes in the SNR as a result of coded excitation was studied, and TFM imaging comparisons are shown for the conventional pulse excitation as well as the Golay excitation cases. A conclusion of this chapter is presented in Section 3.5.

3.3. Methodology

3.3.1. Flexible Array Characterisation

A traditional pulse-echo technique was used to evaluate the performance of a 20 MHz, 64 element, 1 mm pitch flexible linear array (Novosound Ltd., Motherwell, United Kingdom) with overall dimensions of 110 x 30 x 0.5 mm [99], as detailed in the photograph of the array in Figure 2.14 (a). The schematic diagram of the geometry of the array transducers in the x-y plane is shown in Figure 3.1 (a). The experimental setup is depicted in Figure 3.1 (b) and included a 6 mm thick flat aluminium plate, which functioned as a reflector, a three-dimensional (3-D) printed Polylactic Acid (PLA) transducer holder to allow 4 mm delay line between the array elements and the reflector in a small water tank. To facilitate array characterisation, it was connected to a 128/256 MicroPulse 6 controller (Peak NDT, Derby, United Kingdom) using an ipex female to Hypertronics male adapter. The system was controlled by a separate laptop using a Gigabit Ethernet connection. The ArrayGen software platform (Peak NDT, Derby, United Kingdom) was used to define the configuration parameters including the array, sample and the acquisition strategy for transmission and reception. A custom LabVIEW platform was employed for data acquisition.

(a) (b)

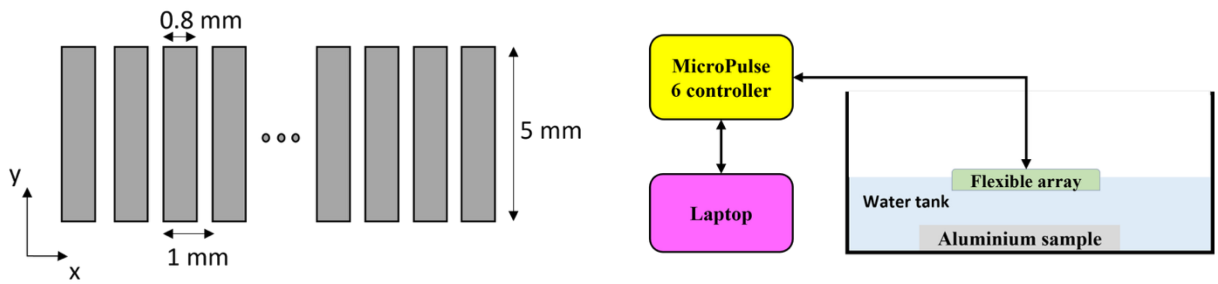

Figure 3. 1: Flexible array configuration and characterisation configuration. (a) Schematic of the geometry of the array transducers in the x-y plane; (b) Schematic of the conventional pulse-echo setup in a water tank used for array characterisation.

3.3.2. Inspection study

3.3.2.1. Phased Array Controller

To facilitate the investigation of coded excitation, a programmable ultrasonic research system with tri-level excitation [+ V, 0, -V] capability (Vantage 128^{TM}, Verasonics Inc., Kirkland, USA) that can generate complex arbitrary waveforms was employed. The Vantage 128^{TM} has a programmable pulser amplitude ranging from 2 to 190 V p-p. The receive frequency range is from 1 – 50 MHz in the high-frequency configuration and an interleaved sampling acquisition scheme was used in this work to achieve an equivalent sampling frequency of 125 MHz [100, 101].

The 14-bit analogue to digital converters (ADCs) offer a sample rate of 62.5 MHz. The standard receive data acquisition scheme that the system uses is data sampling rate set to 4 times the transmit frequency. This is designated as 4 samplesPerWave. This leads to an upper limit of 15.625 MHz for the centre frequency in the received data, with a Nyquist bandwidth limit covering from direct current (DC) to 31.25 MHz. In instances where the target bandwidth aligns within this spectrum for a given probe and application, the proposed acquisition scheme can be employed, yielding good outcomes by configuring the bandpass filter coefficients to correspond with the intended centre frequency and bandwidth. Interleaved sampling is an acquisition strategy that doubles the sample rate of the ADCs by merging samples from two consecutive transmit-receive sequences. The sampling points in the second acquisition are shifted by half of the analogue to digital sampling period in relation to those in the initial sequence. For instance, two acquisitions at the 62.5 MHz sample rate can be combined or interleaved to produce a sample rate of

125 MHz. The Vantage software automatically interleaves the data acquired with the two transmissions provided the sample mode is set accordingly [101]. Figure 3.2 shows the schematic diagram of the interleaved sampling principle. The Vantage 128™ can only sample every 16 ns. Implementing two transmissions, each delayed by 8 ns from the other, allows the acquisition of interleaved values. The purple curve is 8 ns later from the green curve. It is simply shifted in time. To ensure functionality, the transmission of the purple curve (representing the delayed transmission) preceded that of the zero transmission (green curve). Subsequently, interleaved sampling mode was activated on the receive structure within the acquisition file. The acquired data is automatically interleaved by the Vantage software.

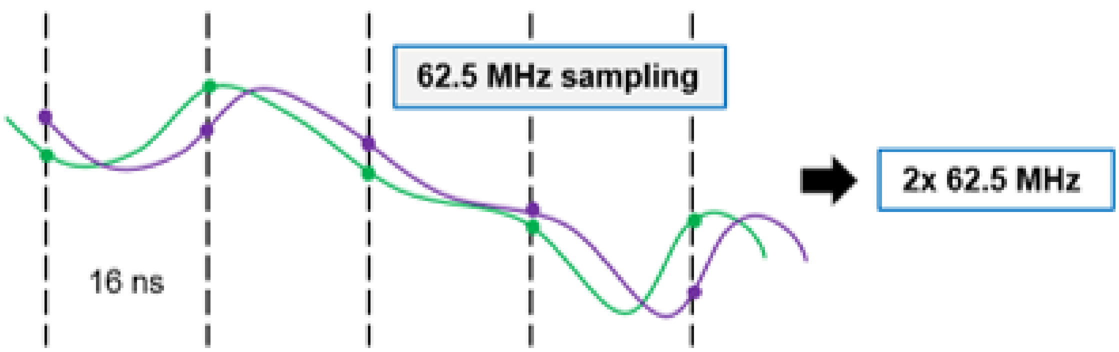

Figure 3. 2: Interleaved sampling schematic diagram. The purple curve, delayed by 8 ns relative to the green curve, reflects a mere temporal shift. To ensure functionality, the transmission of the purple curve – denotating the delayed signal – was executed prior to that of the zero-delay transmission, represented by the green curve.

The array was connected to the Vantage 128™ using an IPEX female to Hypertronics male adapter that interfaced to a Universal Transducer Adapter (UTA) 160-DH/32 LEMO. The acquisition data flow occurs from the array to the host memory of the computer. The signals are sampled and digitised in 14-bit ADCs. They are then conditioned in the digital front end, with two digital filters and decimators providing low-pass or band-pass filtering. The signals are locally stored and, subsequently, transferred to the host memory via peripheral component interconnect express (PCIe) cables [100, 101].

3.3.2.2. Golay-Coded Excitation

Golay complementary sequences (GCS) belong to a subset of binary code pairs found in a larger collection of signals referred to as complementary pairs. These sequences encompass two codes with the same length, $L = 2^n$ cycles, where n represents an integer with a minimum value of 1. Their auto-correlation functions exhibit side-lobes of equivalent magnitudes but opposite polarities. Adding them together yields a combined auto-correlation function featuring zero sidelobes [56, 19, 33]. The sequence, or code, is transmitted to a transducer, and a decoding filter is applied during the reception phase. The received data is compressed through cross-correlation, using a matched filter derived from the initial excitation pulse. The summation is then performed on the pair of cross-correlated signals.

Sets of GCS were constructed using a recursive method. The approach involves starting with two shorter sequences that are subsequently combined through a prescribed method to create longer sequences. Consider the variables $a(k)$ and $b(k)$ as the elements ($k = 0, 1, 2, 3, \dots, 2^n - 1$) of two complementary codes of length 2^n, with the elements equal to either +1 or -1

$$a_0(k) = \delta(k) \tag{3.1}$$

$$b_0(k) = \delta(k) \tag{3.2}$$

$$a_n(k) = a_{n-1}(k) + b_{n-1}(k - 2^{n-1}) \tag{3.3}$$

$$b_n(k) = a_{n-1}(k) - b_{n-1}(k - 2^{n-1}) \tag{3.4}$$

where $\delta(k)$ is the Kronecker delta function. In the case where $n = 1$, the variable k assumes values of 0 and 1. Solving Equations 3.1 – 3.4 results in the complementary sequences $A = [1, 1]$ and $B = [1, -1]$. Longer sequences can now be created. Another Golay pair of length twice that of the pair A and B can be formed by concatenation [AB, A(-B)]. For example, when $n = 2$, the complementary sequences become $A = [1, 1, 1, -1]$ and $B = [1, 1, -1, 1]$. Executing these operations iteratively enables the generation of more extended sequences. Table 3.1 displays GCS with lengths up to 32. A compromise for achieving optimal range of sidelobe cancellation is the necessity for two consecutive firings, thereby introducing motion-dependent decoding errors [56, 102].

Instead of employing direct transmission, the established technique for integrating binary coded excitation encompasses modulation with a waveform [56, 103]. Thus, Golay-coded pulse trains were programmed in the Vantage 128™ and modulated with a waveform at 20 MHz. The resulting waveforms were utilised to excite the array and for data acquisition.

Table 3. 2: Golay complementary sequences with different lengths.

Length ($L = 2^n$)	n	Sequence A	Sequence B
2	1	[1, 1]	[1, -1]
4	2	[1, 1, 1, -1]	[1, 1, -1, 1]
8	3	[1, 1, 1, -1, 1, 1, -1, 1]	[1, 1, 1, -1, -1, -1, 1, -1]
16	4	[1, 1, 1, -1, 1, 1, -1, 1, 1, 1, 1, -1, -1, 1, -1, 1, -1]	[1, 1, 1, -1, 1, 1, -1, 1, -1, -1, -1, 1, 1, 1, -1, 1]
32	5	[1, 1, 1, -1, 1, 1, -1, 1, 1, 1, 1, -1, -1, 1, -1, 1, -1, 1, 1, 1, -1, 1, 1, -1, 1, -1, 1, -1, -1, 1, 1, 1, -1, 1]	[1, 1, 1, -1, 1, 1, -1, 1, 1, 1, 1, -1, -1, -1, 1, -1, -1, -1, -1, 1, -1, -1, 1, -1, 1, 1, 1, -1, -1, -1, 1, -1]

A simulation using the Verasonics Vantage software was employed to demonstrate the principle of sidelobe cancellation. The ultrasonic array was positioned on an acoustic medium (longitudinal velocity of 6320 m/s) with only a single target. An illustration of the imaging plane is shown in Fig. 3.3 (a). It highlights the location of the array elements and the target. The excitation employed a single cycle, used for reference, and 4 cycles of Golay waveforms, as depicted in Fig. 3.3 (b) – (d), with all signals in tri-level representation as defined by the instrumentation. The green arrows for the Golay case indicates the phase of the complementary sequences of length 4. Full matrix acquisition was simulated and random noise was deliberately introduced to the received signals. The response of a single cycle is depicted in Fig. 3.3 (e). For the Golay case, the received signals undergo compression via convolution, employing a matched filter generated from the excitation pulse, as shown in Fig. 3.3 (f). The A-scan of interest is derived from the summation of the pair of convolved signals, as depicted in Fig. 3.3 (g).

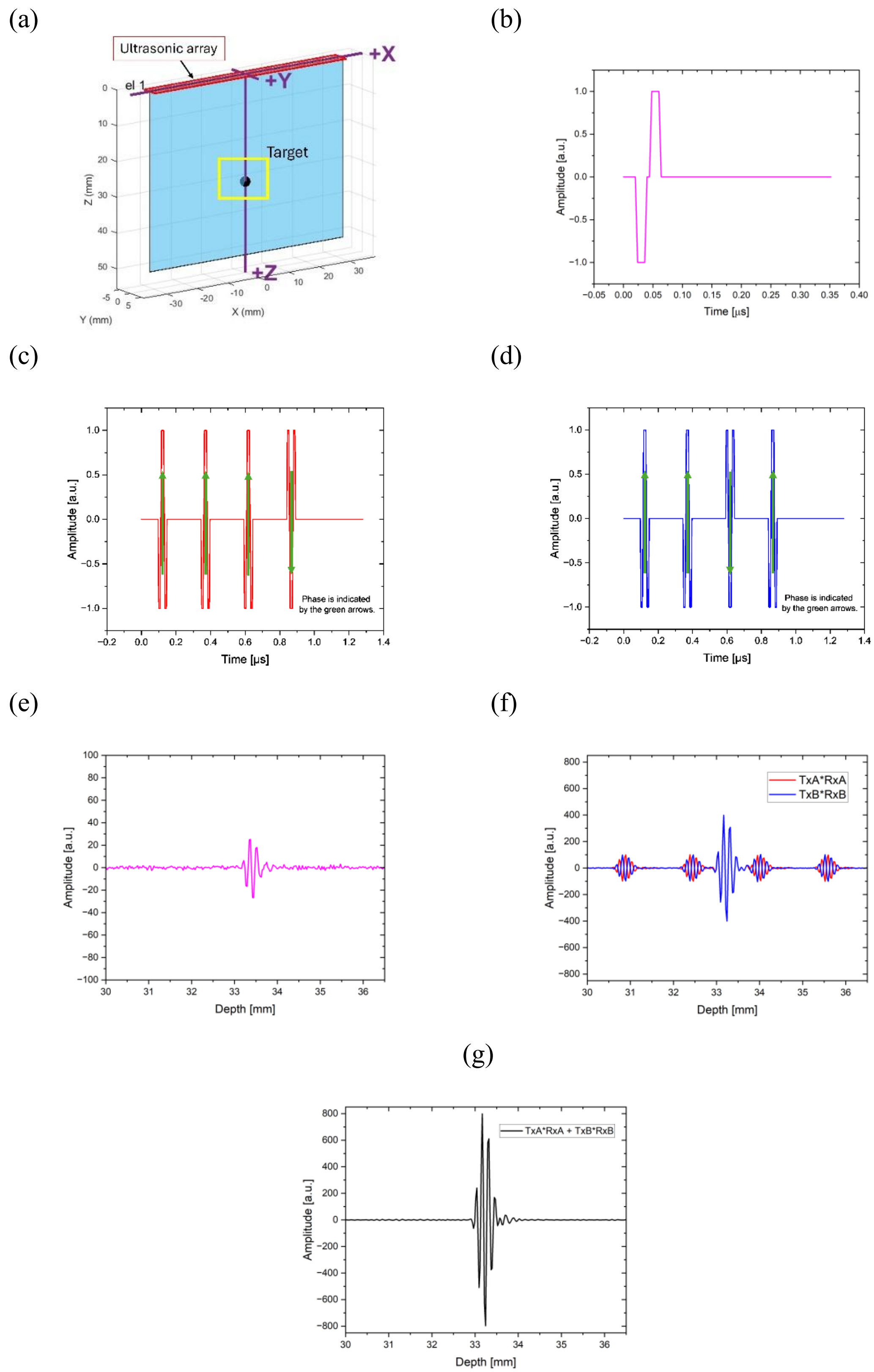
(a)
Ultrasonic array
el 1
+X
+Y
+Z
Target
Z (mm)
X (mm)
Y (mm)
(b)
Amplitude [a.u.]
Time [µs]
(c)
Amplitude [a.u.]
Time [µs]
Phase is indicated by the green arrows.
(d)
Amplitude [a.u.]
Time [µs]
Phase is indicated by the green arrows.
(e)
Amplitude [a.u.]
Depth [mm]
(f)
TxA*RxA
TxB*RxB
Amplitude [a.u.]
Depth [mm]
(g)
TxA*RxA + TxB*RxB
Amplitude [a.u.]
Depth [mm]

Figure 3. 3: Simulation work to demonstrate the sidelobe cancellation principle. (a) Illustration of the imaging plane showcasing the array with emphasis on the position of its elements and the target location. (b) Single cycle excitation waveform (tri-level representation) utilised as reference. (c) Golay A excitation waveform (tri-level representation). (d) Golay B excitation waveform (tri-level representation). (e) Response of the single cycle excitation. (f) and (g) Demonstration of the principle of sidelobe cancellation using the pair of complementary Golay sequences (Golay A and Golay B) of 4 cycles. The convolution operator is represented by the "" symbol. TxA and TxB are the transmit signals in Fig. 3.3 (c) and Fig. 3.3 (d), respectively. RxA and RxB are the receive signals A and B, respectively. The term "a.u." means arbitrary units.*

3.3.2.3. Full Matrix Capture and Total Focusing Method

To implement the CGS, two transmissions are required. A MATLAB-based platform was developed to interface with the Vantage 128™ and allow FMC acquisition. In FMC, each array element transmits in turn and all array elements receive on each transmission event. This allows all possible transmit-receive combinations to produce a complete set of A-scans. For each transmission, the dataset contains $N \times N$ matrix of A-scans, where N is the number of elements in the array. The primary limitation of the FMC method is the reduced acoustic power output from individual elements during transmission. This leads to a decrease in SNR for each transmit-receive pair compared to conventional multi-element aperture imaging techniques. The data was stored in a MAT-file format, and subsequently processed in MATLAB. Following data collection, the principle of sidelobe cancellation, where the pair of Rx signals are converted to a single A-scan and where the sidelobes from the pair are removed, was applied and the resulting decoded signal was further processed with a TFM imaging algorithm. In TFM, the beam is focused at each point within the image region on both transmit and receive. This region is initially discretised into a grid. Each point in the grid is estimated by summing the pathcompensated amplitudes over the set of transmit-receive pairs, hence, producing a focus at each point [89].

3.4. Experimental Results and Discussions

3.4.1. Flexible Array Characterisation

The array was excited with a 24 ns 80 V p-p electrical pulse, generated by the MicroPulse 6 controller, as depicted in Fig. 3. 1 (b), which was the closest the software permitted to the ideal 25 ns for 20 MHz. The custom LabVIEW platform is set to acquire FMC data, which was subsequently stored in a HDF5 Multi-Frame Matrix Capture (MFMC) file format [104]. Data was then processed using MATLAB and the FMC diagonal, representing each element pulse-echo response, was examined. Figure 3.4 represents the average measured pulse-echo response of the array from the front face of the reflector, indicating the typical time domain, Figure 3.4 (a), and frequency domain, Figure 3.4 (b), responses of the array. The frequency spectrum was obtained from the individual time-domain waveforms using the Fast Fourier Transform (FFT) method and then averaged. The average peak frequency and the -6 dB bandwidth were determined, with the average of all the peak frequencies (measured from 64 A-scans of the matrix diagonal) determined to be 24.15 MHz, with a standard deviation of 1.88 MHz, and the average -6 dB bandwidth calculated to be 64.70%. Notably, this novel lead-free, flexible array complies with the BS EN ISO 18563-2:2017 standard [99].

(a) (b)

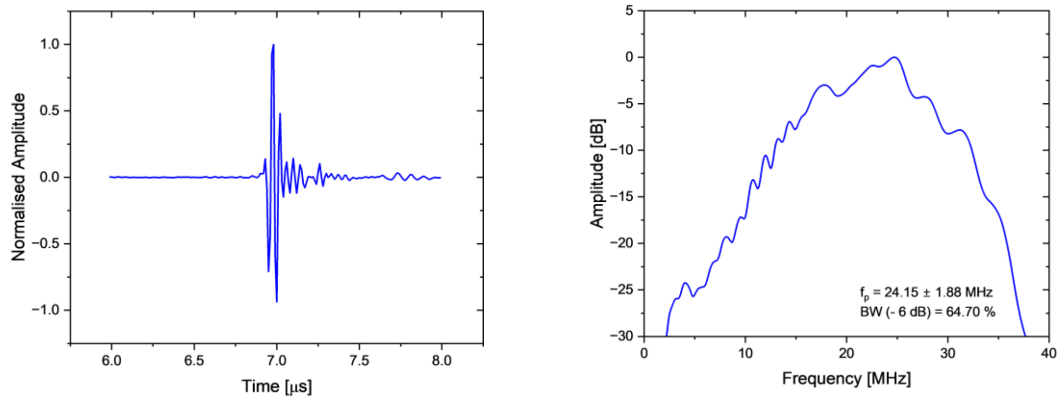

Figure 3. 4: Pulse-echo response of the array. (a) Time-domain response and (b) corresponding frequency spectrum from the front wall reflection of the aluminium test specimen. The schematic of the data acquisition setup is shown in Fig. 3.1 (b).

3.4.2. Inspection Study

3.4.2.1. Resolution

Next, the theoretical improvement in axial resolution offered by high-frequency ultrasonic waves was examined. The performance of a 5 MHz, 64 element, 1 mm pitch Olympus flexible linear array was evaluated against the 20 MHz 64 element 1 mm pitch lead-free flexible linear array. The arrays were in direct contact with a 300 x 20 x 100 mm planar aluminium test specimen through EchoPure ^{TM}couplant gel (Echo Ultrasonics®, LLC, Bellingham, USA). In TFM imaging, it is usual to include A-scan contributions from all element pairs for each pixel. However, it is essential to ensure that the directivity of each element is wide enough for its emitted beam to contribute usefully to the signal, rather than simply adding noise. This is particularly important when imaging close to the array, but applies more widely when performing TFM where the pitch of the array is greater than the conventional λ/2 criterion [89]. One approach that addresses this issue is to mask contributions from elements where the path of the ray exceeds a specified angle with respect to the normal to the element. This threshold angle would typically be derived from the element directivity angle [105-107]. Therefore, by considering the predicted array element beam spread angle (or directivity angle), a sub-aperture imaging configuration can be determined for each array experimental set-up and subsequently employed to improve SNR. Figure 3.5 (a) shows a schematic of a single array element, highlighting the beam spread angle for the arbitrarily selected threshold of –6 dB with respect to the maximum at that range. This angle consists of the total angular extent measured from one side to the other of the main lobe of the ultrasound beam in the far field. A beam computation model of an unfocused longitudinal transmission was produced using the NDT simulation software package CIVA [108] for the 20 MHz array case. Beam computation models using CIVA have previously been employed for weld inspection applications [109]. Hence, the beam spread angle (-6dB) obtained from a representative single array element model is 22.63°. This compares favourably with the theoretical value of 23.43° calculated using Equation 3.5 [110].

$$\theta_{-6dB} = 2\sin^{-1}(0.514\lambda/A) \tag{3.5}$$

where λ is the wavelength in the specimen and A is the aperture of the array element. The -6 dB width can then be obtained by applying trigonometry principles at the desired imaging depth in the sample (z-axis). For example, at the depth corresponding to the location of the second target (17 mm), the -6 dB width is 7.05 mm, thus, an 8-element sub-aperture was employed. This the sub-aperture selection methodology is illustrated in Figure 3.5 (b).

(a)

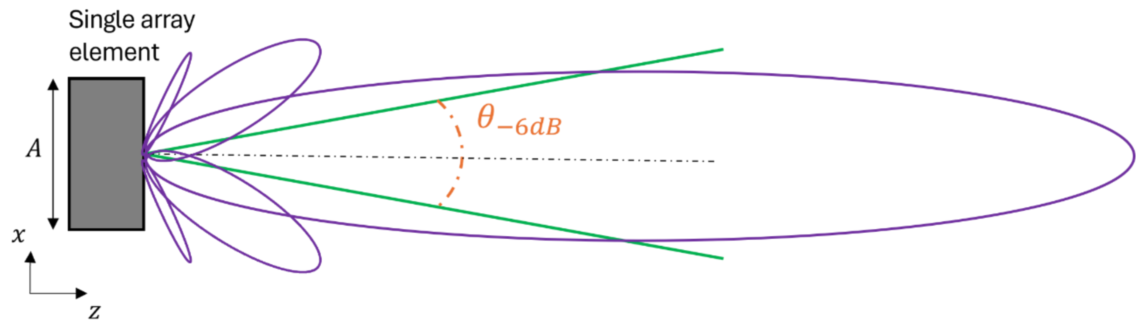

(b)

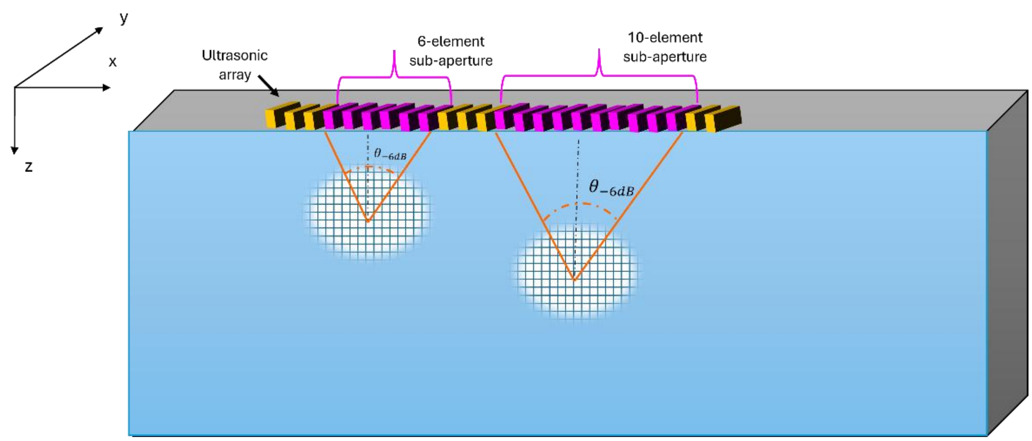

Figure 3. 5: Beam spread analysis. (a) Single array element schematic with emphasis of the beam spread angle. (b) Principle of sub-aperture selection based on the beam spread or element directivity analysis. The element size is 0.8 mm.

Figure 3.6 (a) shows the schematic of the acquisition setup. A 64 g PLA block was positioned on the array elements to ensure uniform pressure, thus facilitating consistent signal acquisition. The test specimen featured four side-drilled holes (SDHs) machined from the side, each with a diameter of 1 mm and a length of 20 mm. The SDHs were positioned 8-17 mm into the sample with the centres spaced 3 mm apart along the axial direction. The Vantage 128^{TM} was used to acquire FMC dataset. The arrays were excited using half a cycle at 80 V, with the receive gain set to 40 dB. Figure 3.6 (b) and (d) depict

TFM images formed using the 5 MHz array (using a 48-element sub-aperture, by considering the beam spread effect. The calculated -6 dB beam spread angle was 108.61^{o}) and the 20 MHz array (employing an 8-element sub-aperture), respectively. The SNR for each target is higher for the 5 MHz, with a maximum value of 24.8 dB, compared to the 20 MHz array, which achieved a maximum value of 18.6 dB. The observed increase in SNR at 5 MHz is consistent with expectations, attributed to the material properties of the transducer, larger aperture and the resultant higher transmission energy. As anticipated, the 20 MHz array demonstrated higher axial resolution compared to the 5 MHz array. The SDHs can be clearly distinguished along the axial direction for the 20 MHz case, as shown in Figure 3.6 (e). In contrast, in the 5 MHz case, shown in Figure 3.6 (b), as expected from the lower operating frequency, the SDHs are less well resolved and it would be challenging to separate them at 5 MHz if the holes were positioned any closer.

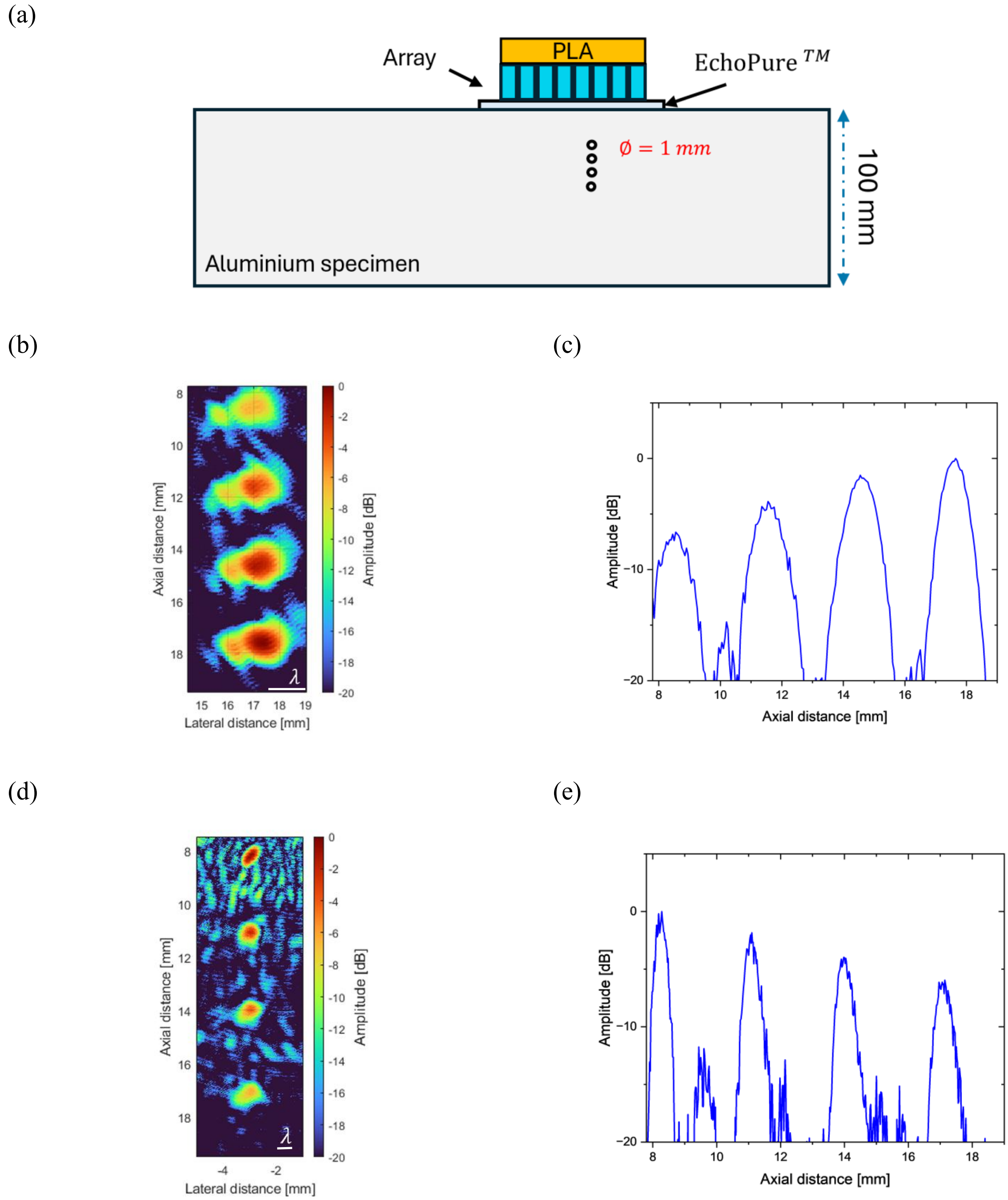

Figure 3. 6: Axial resolution evaluation. (a) Schematic of the axial resolution setup. The 5 MHz and the 20 MHz arrays were directly coupled to the aluminium specimen in turn. A PLA block (64 g) was placed on top of the array elements to ensure alignment; (b)

TFM image corresponding to the 5 MHz array using a 48-element sub-aperture; (c) Cross-section of the TFM image of the 5 MHz array through the central axis of the SDHs; (d) TFM image corresponding to the 20 MHz array using an 8-element sub-aperture; (e) Cross-section of the TFM image of the 20 MHz array through the central axis of the SDHs. The element size of each array is 0.8 mm. The pattern observed in the cross-section of the TFM images arises as a consequence of the sub-aperture selection.

3.4.2.2. Evaluation of SNR Improvement

This experimental study aimed to verify improvement in SNR experimentally as the length of the Golay codes increased. Golay-coded excitations comprising of 2, 4 and 8 cycles were used. The 20 MHz array was directly coupled to the 100 mm thick flat aluminium sample (as depicted in Fig. 3.6) using EchoPure ^{TM}couplant gel. In this case, the target was an SDH with a 1.5 mm diameter, located at a 30 mm depth from the top surface of the sample. To ensure consistent pressure is being employed on the array, a PLA block (64 g) was placed on top of the array elements. The Verasonics Vantage 128^{TM} was operated to acquire FMC data. The array was excited with an excitation voltage of 60 V and the receive gain was set to 40 dB. The beam spread effect was considered and a sub-aperture of 14 elements was utilised. TFM images were subsequently produced and Equation 3.6 [88] was used to quantify the SNR. Given the known locations of defects, the SNR value was computed within a specified region surrounding each defect. Moreover, the noise level was determined as the root mean square (RMS) of the image noise, excluding any indication of defects [88].

$$SNR = 20\,log_{10}\left(\frac{A_{max}(r)}{\sqrt{\left(A_{noise}(I_n)^2\right)}}\right) \tag{3.6}$$

The SNR of the echo was evaluated across a series of acquisition modes, commencing with the reference point of single-cycle excitation. The second instance used the same setup but with a two-pulse excitation. Subsequent modes involved Golay acquisition and processing for 2, 4, and 8 cycles each in sequence. Figure 3.7 shows the measured SNR for the different excitation modes. As anticipated, improvement in SNR was observed as the length of the Golay codes increased. It should be noted that extending the length of the transmitting signals results in an increased dead zone before the detection of the first receive signals. Figure 3.8 displays experimentally acquired A-scans obtained using Golay-coded excitation, clearly demonstrating the progressive increase in dead zone duration with the increasing code length. The dead zone extends to approximately 0.7 µs for Golay 2, 1.2 µs for Golat 4, and 2.2 µs for Golay 8. Therefore, selection of the appropriate Golay length relies on the specific application and will be a compromise between acceptable SNR and ensuring that the length of the dead zone does not compromise the near-surface defect detection performance [19].

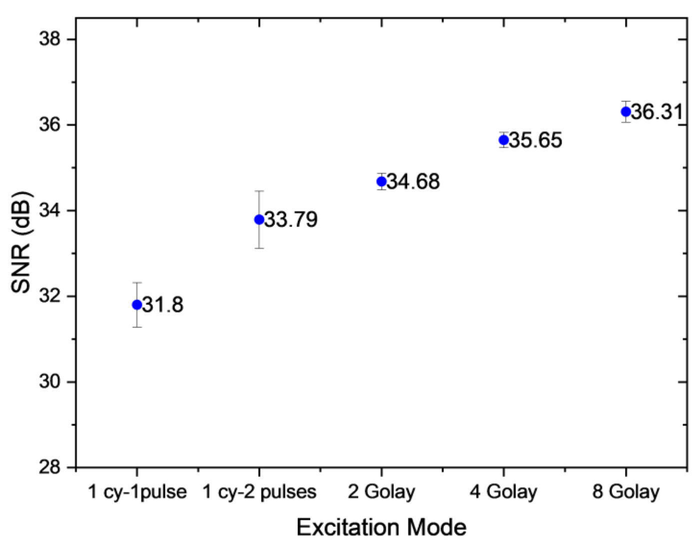

Figure 3. 7: Measured SNR with respect to different excitation modes. Enhancement in SNR noted with increase in the length of the Golay codes. The term "1 cy-1 pulse" indicates one cycle with a single pulse, while "1 cy-2 pulses" indicates one cycle with two pulses.

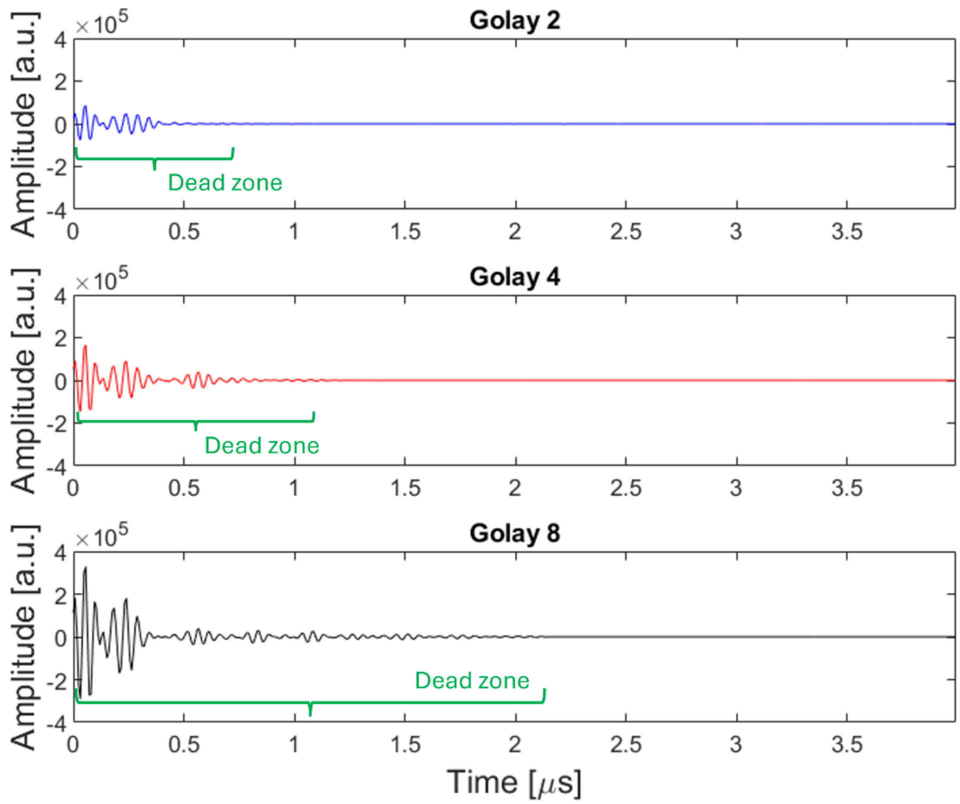

Figure 3. 8: Dead zone analysis using experimentally acquired data for Golay coded excitation of 2, 4, and 8 cycles.

3.4.2.3. Imaging a Non-Planar Component

The aim of this study was to evaluate the improvement in SNR on a non-planar component using the designed Golay complementary sequences to excite the lead-free array. An imaging comparison is presented in terms of the Golay-based TFM and the conventional pulse-based TFM. Experimental work was conducted on a 150 x 20 x 70 mm non-planar steel S355 specimen with a radius of curvature of 150 mm to represent non-planar industrial components. The specimen is depicted in Figure 3.9 and has machined defects, which consist of three SDHs, 2 mm in diameter, 20 mm long, drilled from the side of the sample. The SDHs are positioned 15 mm apart from each other laterally and 10 mm apart axially.

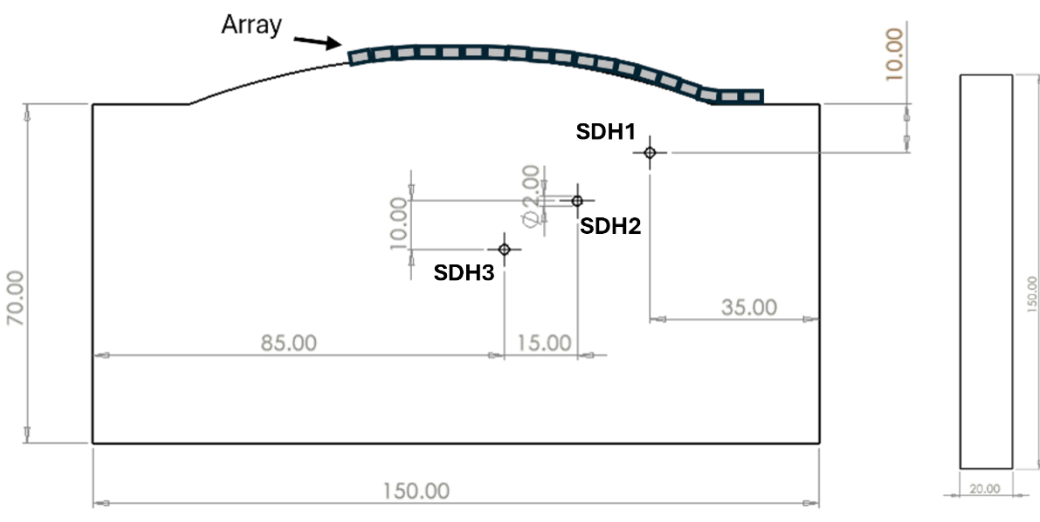

Figure 3. 9: Schematics of the steel S355 sample displaying the arrangement of side-drilled holes at various depths. Bottom view is depicted on the right. All dimensions are in millimetres (mm).

Pulse-echo measurements were conducted using the 20-MHz, lead-free, flexible ultrasonic array. The array was in direct contact with the sample using

EchoPure ^{TM}couplant gel. It was magnetically attached to the sample by means of two 10 mm diameter, 5 mm thick neodymium magnetic discs, carefully positioned to avoid coverage of the array elements. The key acquisition parameters of the experimental setup included 80 V for excitation, a receive gain of 40 dB and the sample rate set to 125 MHz. A single cycle was initially used to excite the array and produce the conventional pulse-based TFM image. Then, in the context of this particular application, where the positions of the defects are known, and considering the enhancement in SNR as well as the impact of the dead zone, 8 cycles of Golay excitation were employed to excite the array and the Golay-based TFM image was produced. Figure 3.10 shows TFM images utilising all 64 array elements during FMC data acquisition for both scenarios corresponding to the region of interest. To assess the enhancement in image quality, the SNR was quantified using Equation 3. 6. Table 3.2 shows the measured SNR values from each TFM image depicted in Figure 3.10. Figure 3.10 (a) and (d) show SDH1 being detected for both excitation cases, with an improvement of 4.95 dB calculated for the Golay result when compared to the conventional pulse excitation. Transmitting 8 cycles of Golay sequences allowed deeper penetration into the sample, as shown in Figure 3. 10 (e), enabling SDH2 to be detected, with an SNR of 16.28 dB. The targets in Figure 3. 10 (b), (c) and (f) were not detected.

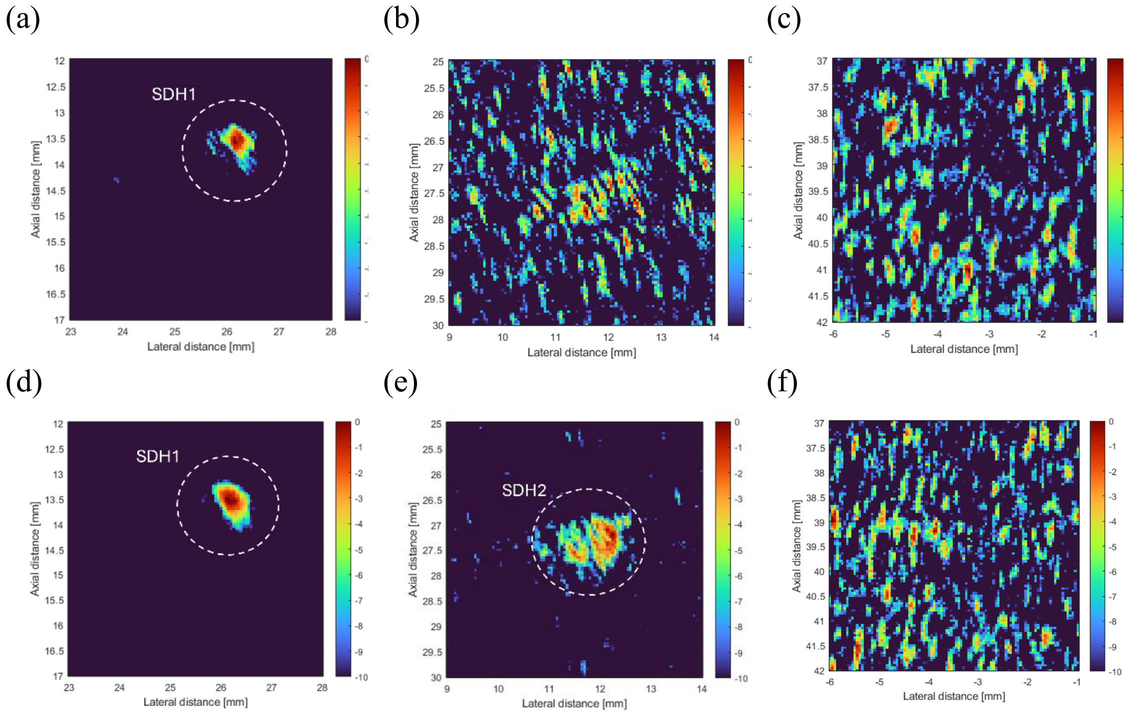

Figure 3. 10: TFM images employing all 64 elements for FMC data acquisition. (a) Conventional pulse-based TFM image for SDH1. (b) Conventional pulse-based TFM image for SDH2. (c) Conventional pulse-based TFM image for SDH3. (d) Golay-based TFM for SDH1. (e) Golay-based TFM for SDH2; (f) Golay-based TFM for SDH3. Golay-based TFM exhibits superior imaging contrast and higher SNR compared to the conventional pulse-based TFM, indicating improvement in imaging quality.

Table 3. 3: SNR measurement from TFM images using all 64 elements. Golay-coded excitation offers improved detection capability with higher SNR.

Targets	SNR (dB)		Improvement
	Pulse	Golay	
SDH1	19.57	24.52	4.95 dB
SDH2	Not detected	16.28	Detection
SDH3	Not detected	Not detected	Not detected

3.4.2.4. Effect of the Element Directivity

It has been noted (in sub-section 3.4.2.1.) that in TFM imaging, it is standard practice to incorporate A-scan contributions from all possible element pairs for each pixel. This can introduce unnecessary noise if the directivity of each element is not wide enough for its emitted beam to contribute meaningfully to the signal. Hence, by accounting for the beam spread angle of the array element, a sub-aperture from the initial FMC dataset can be selected, resulting in an improved SNR. Figure 3.11 depicts the TFM images employing a 6-element sub-aperture for the SHD1 region, a 12-element sub-aperture for the SHD2 region and a 16-element sub-aperture for the SDH3 region. The calculated beam spread angle was $\mathbf{22.23}^{\circ}$. SDH1 and SDH2 were detected in both excitation scenarios, as depicted in Figure 3.11 (a), (b) (d) and (e). The selected sub-aperture, leveraging the element directivity effect, enabled the detection of SDH2 in the pulse excitation case, as shown in Figure 3.11 (b), which was otherwise undetectable with all 64 array elements, as shown in Figure 3.10 (b). The Golay case also detected SDH2, with an SNR improvement of 2.74 dB. Importantly, the detection of SDH3 was now successfully achieved in the Golay case, as illustrated in Figure 3.11 (f), whereas the pulse excitation case did not detect SDH3 (Figure 3.11 (c)). Table 3.3 displays the measured SNR values corresponding to each TFM image depicted in Figure 3.11. The element directivity effect resulted in further SNR improvement overall. For the Golay case, 8.2 dB of SNR improvement was observed for the SDH2. For all cases, improvement in imaging quality was obtained. The Golay-based TFM outperforms the conventional pulse-based TFM.

Improved imaging penetration depth using a combination of a lead-free, flexible ultrasonic array with coded excitation strategies has been demonstrated.

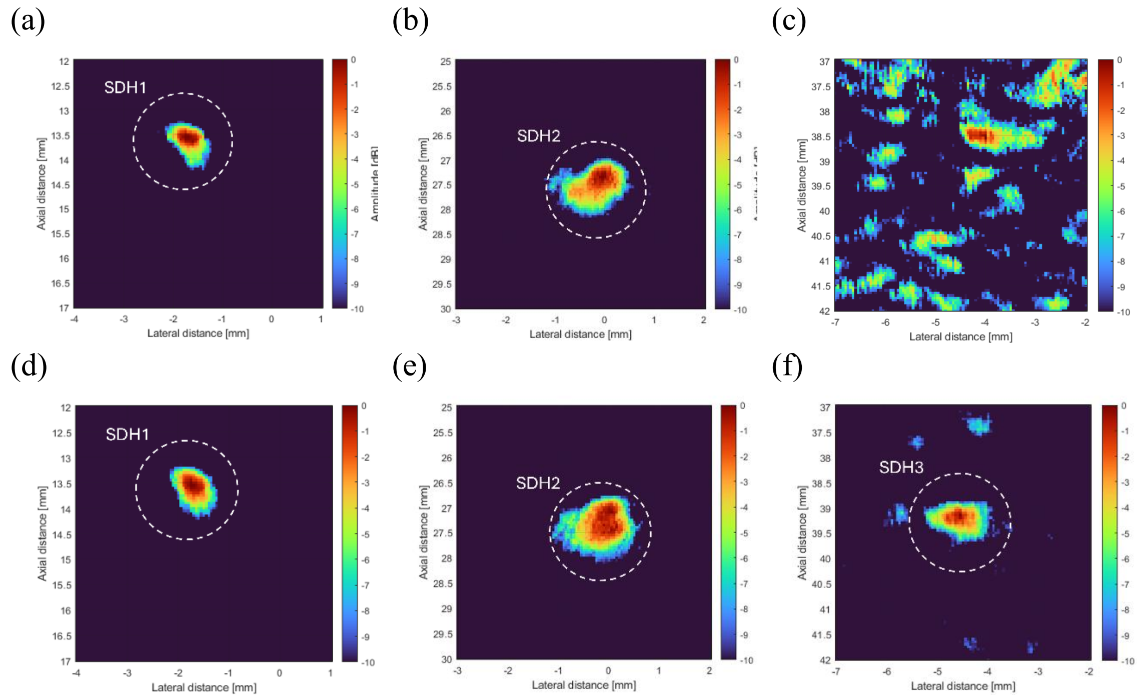

Figure 3. 11: TFM images employing different sub-aperture considering the beam spread effect. (a) Pulse-based TFM image for SDH1. (b) Pulse-based TFM image for SDH2. (c) Pulse-based TFM image for SDH3. (d) Golay-based TFM for SDH1. (e) Golay-based TFM for SDH2. (f) Golay-based TFM for SDH3. Improved imaging depth observed.

Table 3. 4: SNR measurement from the TFM images in Fig. 3.11. The selected sub-aperture, exploiting the element directivity effect offered enhanced detection capability for both the pulse and the phase-modulated Golay excitation cases.

Targets	SNR (dB)		Improvement
	Pulse	Golay	
SDH1	23.16	24.67	1.51 dB
SDH2	21.74	24.48	2.74 dB
SDH3	Not detected	17.15	Detection

3.5. Conclusion

In this chapter, a 20-MHz, lead-free, flexible ultrasonic array has been characterised. The array complies with the BS EN ISO 18563-2:2017 standard, with an average -6 dB bandwidth of 64.70 %. Golay-coded excitation schemes have been designed and implemented to overcome the limit associated to the axial resolution and penetration depth trade-off. An improvement verification study has been conducted and as expected, increase in SNR was observed as the length of Golay codes increased. The appropriate length of the Golay codes depends on specific application, including acceptable SNR as well as the dead zone not compromising the near-field defect detection performance. The FMC technique for acquisition and the TFM algorithm for imaging were employed to compare the performance of the conventional pulse excitation against Golay-coded excitation strategies. Using the full-array aperture and in direct contact to a non-planar steel S355 test specimen, the Golay-based TFM outperformed the conventional pulse-based TFM, with 4.95 dB of SNR improvement observed. The selected sub-apertures based on the beam spread effect provided further SNR improvement (> 8 dB) and greater imaging penetration depth was achieved, surpassing the conventional approach by more than 40 %, successfully detecting SDH3 with an SNR of 17.15 dB, which was undetectable under the conventional excitation condition. The approach described in this chapter, integrating a high-frequency lead-free flexible ultrasonic array with Golay-coded excitation, holds promise for improving the SNR, penetration depth and imaging quality for the inspection of thick section components with a complex surface profile.

Chapter 4

Single Transmission Phase- and Frequency-Modulated Signals for Enhanced Inspection of Thick Complex Industrial Components

4.1. Chapter Overview

In this chapter, a scalable, RoHS-compliant, flexible ultrasonic array was employed to improve operability in thick convex and concave components. However, the lead-free array exhibits lower piezoelectric coefficient compared to its lead-based counterparts, resulting in reduced signal quality. To tackle this shortcoming, single transmission phase-modulated Barker and frequency-modulated chirp excitation schemes, in conjunction with pulse compression, were employed to improve the signal quality. Subsequently, their impact was studied in terms of imaging quality, through FMC acquisition methodology and TFM imaging, and SNR measurements. A novel SNR method was presented. Existing SNR approaches evaluate image quality by calculating it within a designated area surrounding the target, where the noise level is quantified as the root mean square of the image noise, omitting any indication of the target. In addition to the noise level, artifacts from matched filters and sidelobes require quantitative evaluation. The new SNR technique was proposed to automate the selection of regions when characterising the SNR. The SNR was calculated across regions of varying size, with the region size where the SNR values converged being selected. This technique was utilised in a comparative analysis including a single-cycle pulse excitation, modulated Barker and chirp excitation schemes with equivalent energy levels in simulation and experimentally. The simulated and experimental results showed good agreement, with some discrepancies attributed to imperfections in the experimental conditions. The flexibility of the array was assessed in the subsequent two experiments to determine its effectiveness in improving operability in complex-geometry samples. The convex and concave samples pre-aligned the array to promote a converging and diverging ultrasonic beam, respectively. In all cases, the array demonstrated excellent conformity with the components, and the coded excitation schemes consistently achieved better imaging quality relative to the pulse excitation case.

4.2. Introduction

Chapter 3 has demonstrated the application of advanced phase-modulated dual transmission Golay coded excitation scheme combined with FMC/TFM strategies using the high-frequency, lead-free, flexible ultrasonic array for inspection of thick non-planar industrial components. This chapter redirects this emphasis to examine and compare the performance related with single transmission phase-modulated Barker signal and frequency-modulated chirp signal excitation techniques, as Golay excitation schemes result in slower data acquisition and frame rate (by a factor of two), when compared to single transmission schemes, and introduce motion-dependent decoding errors [56, 102].

Coded excitation techniques are categorised based on the use of single or multiple transmissions, and whether their encoding depends on phase or frequency modulation. The most common single transmission phase-modulated signal is Barker, while the most common frequency-modulated signal is chirp [56]. Coded excitation strategies, in conjunction with pulse compression, have been examined as a means to enhance signal quality [61-84]. The traditional approaches to improve SNR involve either reducing the frequency of the ultrasonic array or averaging the results across multiple transmissions. Nevertheless, these methods can lead to compromises in resolution and acquisition rate, respectively [19]. This chapter presents novel work on the performance examination and comparison associated with the single transmission Barker and chirp signal excitation schemes. Existing SNR approaches evaluate image quality by calculating it within a designated area surrounding the target, where the noise level is quantified as the root mean square (RMS) of the image noise, omitting any indication of the target. In addition, the noise level, artifacts from matched filters and sidelobes require quantitative evaluation. The SNR technique used in this work was proposed to automate the selection of regions when characterising the SNR. The SNR was calculated across regions of varying size, with the region size where the SNR values converged being selected. Moreover, a flexible, lead-free ultrasonic array fabricated from zinc oxide is employed to improve operability in thick convex and concave test specimens.

The structure of this chapter is organised as follows: Section 4.3 covers the methodology including information on the array controller and the ultrasonic array used in this study, along with details of the chirp and Barker excitation signals. This is followed by considerations on the transmitted energy of each excitation signal, accompanied by an example on how the energy was computed using a trapezoidal method. An introduction on pulse compression is subsequently provided. Section 4.4 offers a detailed account of the results and discussions. In all scenarios, a sub-aperture selection method was applied, accounting for the influence of the array element directivity angle. The new SNR approach is introduced, where the image noise region is characterised and the parameters at which the SNR convergence occurs are identified. This technique was utilised in a comparative analysis including the single-cycle pulse excitation, Barker and chirp coded excitation strategies with equivalent energy levels in simulation and experimentation. The last sub-section investigated two experiments examining the flexibility of the lead-free array to enhance its operability on thick convex and concave S355 steel samples. Section 4.5 presents the conclusion of this work.

4.3. Methodology

This work employed the phased array controller described in sub-section 3.3.2.1., the programmable ultrasonic system (Vantage 128^{TM}, Verasonics Inc., Kirkland, USA). The 20 MHz, 64 element, 1 mm pitch linear array (Novosound Ltd., Motherwell, United Kingdom) was interfaced with the Vantage 128^{TM} system via an IPEX female to Hypertronics male adapter, connecting with a UTA 160-DH/32 LEMO. The Vantage

128^{TM} system supports interleaved sampling acquisition scheme, which was used to increase the sampling rate to 125 MHz [101].

4.3.1. Chirp and Barker Excitation Signals

Phase- and frequency-modulated signals were used in this work to excite the array. The frequency-modulated signals consisted of linear chirps. They extend across a frequency range defined by the difference between the initial frequency, f_1, and the final frequency, f_2, resulting in a bandwidth $B = f_2 - f_1$. This relationship is described mathematically by Equation 4.1, which represents a linear chirp signal [96]:

$$x(t) = \omega(t)\cos(2\pi f_1 t + \pi b t^2) \qquad t \subset [0, T] \tag{4.1}$$

The signal transitions from f_1 to f_2 over a duration T. The function $\omega(t)$ serves as a windowing function, minimising sidelobes by gradually tapering the edges of the signal. The sweep rate, denotated by b, is given by $b = B/T$. Generally, the duration T is an order of magnitude longer than the impulse response of the array [93, 96]. In this study, the frequency range was set to 14-26 MHz, based on the centre frequency of the array and approximately 60% of -6 dB bandwidth. The impact of using a windowing function was investigated through the application of Tukey windows featuring tapering ratios between 10 % to 80 %. A tapering ratio, *r*, defines the proportion of the window that undergoes cosine-based amplitude tapering at its boundaries. Figure 4.1 illustrates Tukey windows with tapering ratios ranging from 0 to 1 (0 – 100%), in 10% increments. At ratio of r = 0 corresponds to a rectangular window with abrupt transitions, whereas r = 1 results in a fully tapered Hann window. Intermediate values produce progressively broader cosinetapered regions at each extremity. Tukey windows are commonly used with chirp signals due to their flexibility in tapering the waveform [68, 45, 96]. The primary aim of employing a windowing function in a chirp signal is to eliminate Fresnel ripples and suppress sidelobes in the frequency spectrum. However, this results in reduced overall transmitted energy [56, 68, 96, 93]. Fig.4.2 (a) and (b) show examples of nine chirp signals of 1.34 μs duration, and their respective frequency spectra. Fresnel ripples and high sidelobe levels are observed with chirp signals with no window and with Tukey windows from 10 % to 40 %. Chirps modulated with Tukey windows having tapering ratios between 50 % to 80 % exhibit no Fresnel ripples while achieving reductions in sidelobe levels.

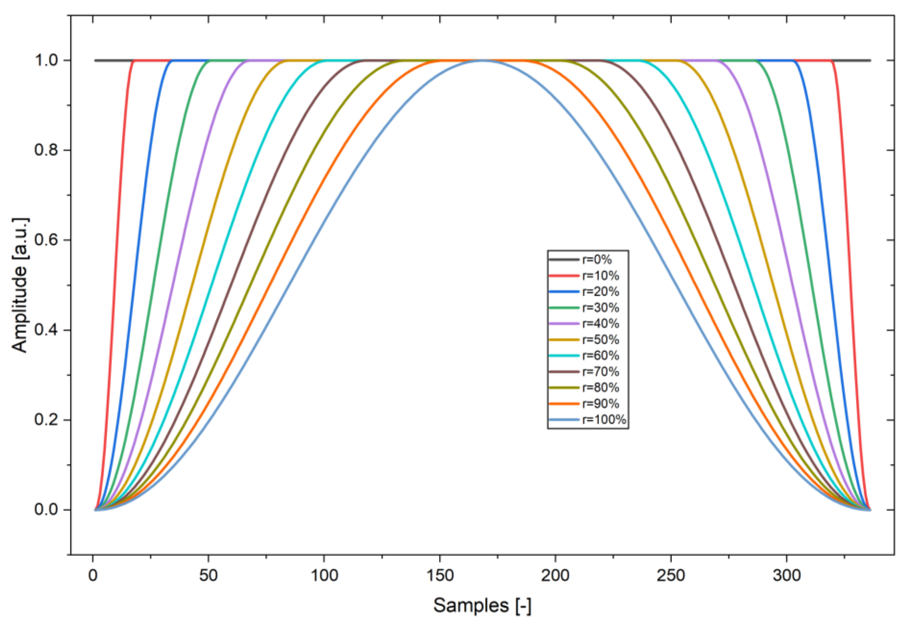

Figure 4. 1: Tukey windows with tapering ratios, r, ranging from 0 to 1 (0 – 100%), in increments of 10%.

Barker signals are the most commonly used single transmission phase-modulated excitation signals [56]. The codes are limited in number, with the longest available code having a length of 13 [56, 83]. Table 4.1 lists Barker codes with lengths between 5 to 13. These codes were modulated with a one cycle waveform at 20 MHz and used to excite the array. Fig. 4.2 (c) and (d) depict a Barker excitation signal of length 13 (0.74 μs) in tri-level representation, as defined by the instrumentation [101], and its corresponding frequency spectrum, respectively.

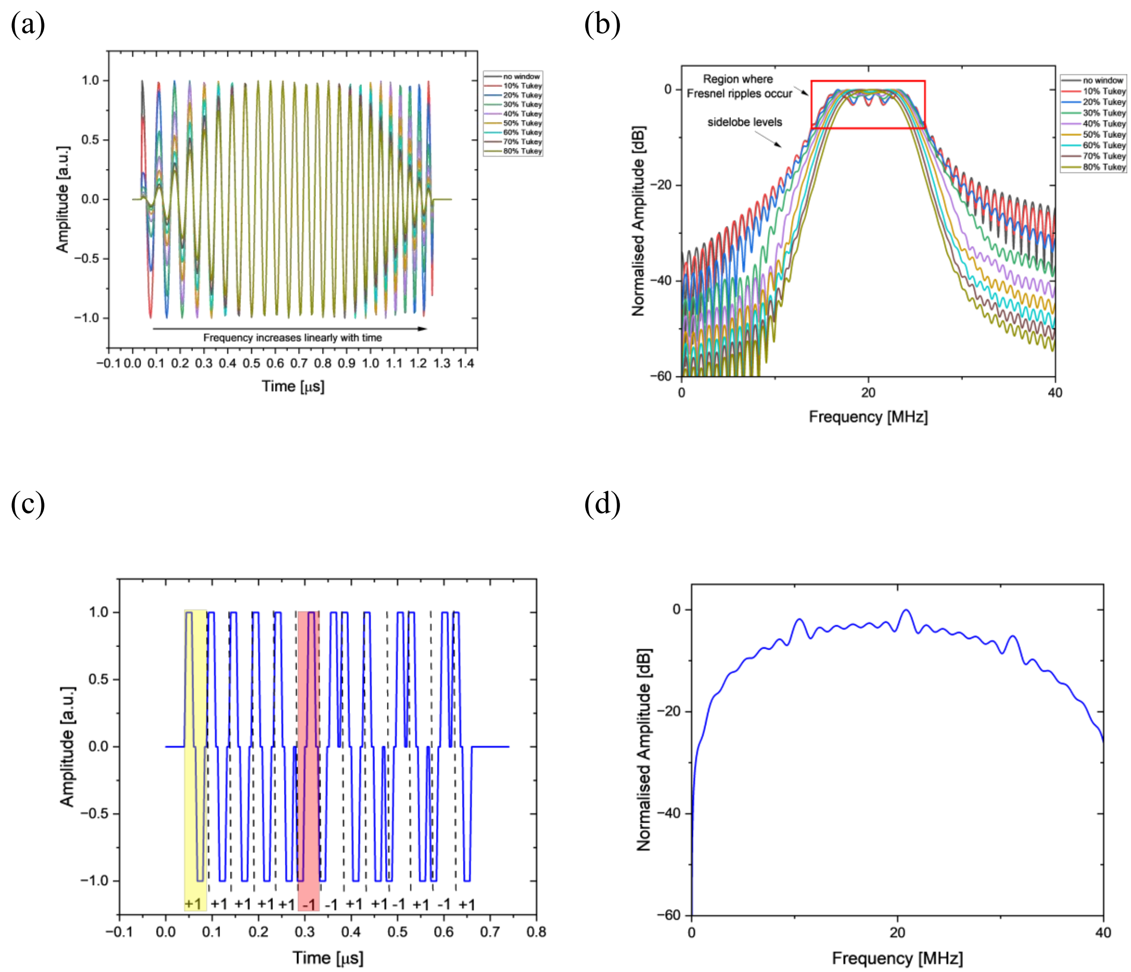

Figure 4. 2: Example of chirp and Barker excitation signals. (a) Frequency-modulated chirp signals of 1.34 µs duration. The signals use no window and Tukey windows with tapering ratios varying from 10 % to 80 % in steps of 10 %. (b) The corresponding spectra of the signals in (a). The red rectangle highlights the region where Fresnel ripples occur and sidelobe levels can be observed. The use of Tukey windows with tapering ratios between 50% and 80 % in chirp signals eliminate Fresnel ripples and reduce sidelobe levels. (c) Phase-modulated Barker excitation signal of length 13 (0.74 µs) in tri-level representation. The shaded yellow area highlights a positive phase and the shaded red area illustrates a negative phase. (d) Corresponding frequency spectrum of the signal in (c).

Table 4. 1: Barker codes with lengths between 5 to 13.

Length	Code
5	[+1,+1,+1,-1,+1]
7	[+1,+1,+1,-1,-1,+1,-1]
11	[+1,+1,+1,-1,-1,-1,+1,-1,-1,+1,-1]
13	[+1,+1,+1,+1,+1,-1,-1,+1,+1,-1,+1,-1,+1]

4.3.2. Energy Considerations

In this study, Barker 13, the longest Barker code, was employed as it offers superior SNR improvement over its length counterparts [56]. For comparative purposes, the frequency-modulated chirp signal was designed to possess the same energy to the Barker signal. A 14-26 MHz, 60% Tukey windowed chirp signal consisting of 1.34 μs duration was used, as it possessed the same energy to the Barker 13 (0.74 μs) signal. Moreover, the chirp signal effectively has reduced sidelobes and eliminates Fresnel ripples in the frequency domain, as shown in Fig. 4.2 (b). The selected Barker and chirp signals were utilised in both simulation and experimental work. In general, increasing the length of the transmitted signals inherently leads to an expansion of the dead zone. Selecting the optimal length is application-specific and requires balancing between achieving sufficient SNR with minimising the dead zone length to preserve near-surface defect detection performance [26].

The energy of the phase- and the frequency-modulated signals was calculated using a trapezoidal method. Numerical integrations using the trapezoidal method have previously been employed [111, 112]. The method was implemented by computing the integral of the squared waveform over time. The approach approximates the integral over a specified interval by discretising the region into trapezoidal segments, facilitating computationally efficient area estimation. Fig. 4.3 (a) shows an illustration of a sine function and Fig. 4.3 (b) depicts its squared waveform using sixteen uniformly spaced trapezoidal segments. The trapezoidal integration can be applied. The energy of the Barker 13 (0.74 μs) and the 14-26 MHz, 60% Tukey windowed chirp (1.34 μs) signals was 0.42 arbitrary units (a.u.).

(a) (b)

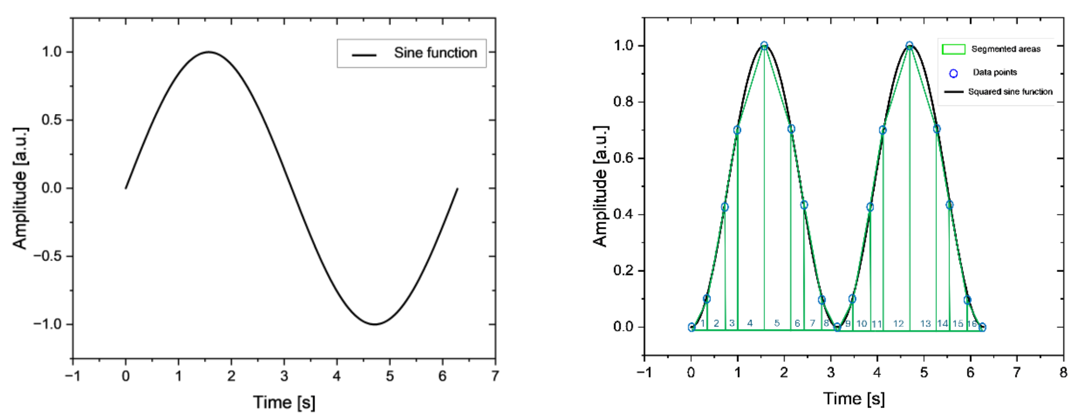

Figure 4. 3: Trapezoidal method representation. (a) Illustration of a sine function. (b) Squared sine waveform divided into sixteen uniformly distributed trapezoids. The trapezoidal approach can be employed by integrating the squared waveform with respect to time.

4.3.3. Pulse Compression

Pulse compression utilises temporally-extended modulated excitation signals to compress the received energy in time. This technique preserves high range resolution while enhancing SNR by increasing the transmission energy [84]. Long single transmission frequency- and phase-modulated excitation signals can be effectively compressed into a short time interval with minimal sidelobes through appropriate filtering techniques. The modulated signals exhibit the desired compression characteristics. The decoding filter is designed to compress the modulated signal energy into a short time interval. It is typically selected to be a matched filter as it provides the optimal detection SNR regardless of the modulation scheme (phase or frequency) [56]. In this work, the received signals undergo compression via convolution with a matched filter (time-reversed modulated excitation signal).

4.4. Results and Discussions

4.4.1. Signal-to-Noise Ratio Approach

Evaluation of the SNR of a given image is commonly conducted by calculating it within a specified region surrounding the target, with its location and size being predetermined [88, 26]. Equation 3.6 is usually employed to quantify the SNR, with the maximum amplitude within the region $\boldsymbol{r}$ surrounding the target denotated by $A_{\max}(r)$. To ensure accuracy, comparisons are subsequently conducted exclusively in regions where the image domain and target regions share the same area and pixel density [88].

Apart from the noise level, images can also possess artifacts due to matched filters [56] and sidelobes [113], all of which require quantification. The sidelobe artifacts are located in the lateral direction, at a similar range to the target. The sidelobes are secondary, lower-intensity lobes in the acoustic beam pattern that radiate at angles divergent from the mainlobe [114]. These undesirable signals appear laterally either side of the expected reflection from the target [8, 33,115]. The matched filter is designed to compress the coded waveform into a short-duration, high-amplitude pulse, however, its performance is inherently imperfect, introducing artifacts. These consist of small undesirable sidelobes in the time-domain signal located before and after the main pulse [56, 84]. A novel SNR method is proposed here to automate the selection of regions when characterising the SNR. The SNR is calculated for regions of varying size, and the region size at which the SNR values stabilised was ultimately selected. $A_{noise}(I_n)$ in Equation 3.6 is replaced by $A_{noise}(I_{nr})$, in which, $\boldsymbol{nr}$ is a region containing noise, excluding any indication of the target and artifacts, as defined in Equation 4.2. This sub-section reports on an experimental study to identify and characterise this region.

$$SNR = 20\, log_{10}\left(\frac{A_{max}(r)}{\sqrt{\overline{\left(A_{noise}(I_{nr})^{2}\right)}}}\right) \tag{4.2}$$

This experimental study focused on examining the characteristics of the image noise region and identifying the parameters where the SNR convergence occurs. The performance of a 5-MHz 96-element 0.55 mm-pitch 8 mm-elevation linear array (Imasonic SAS, Voray sur l'Ognon, France), a 10-MHz 128-element 0.25 mm-pitch 10 mm-elevation linear array (Imasonic SAS, Voray sur l'Ognon, France) and a 20-MHz 64-element, 1 mm-pitch 5 mm-elevation flexible linear array (Novosound Ltd., Motherwell, Scotland) was evaluated. Fig. 4.4 shows the schematic of the acquisition setup. The arrays were coupled to a 30 mm thick planar S355 steel specimen. For the 20 MHz array, owing to its flexible nature, it was secured in place using two neodymium magnetic discs, each 10 mm in diameter and 5 mm thick. The specimen featured an SDH with a diameter of 2 mm and a length of 20 mm. The SDH was located 20 mm in the axial direction away from the array. A threshold angle was determined based on the element directivity angle, as described in sub-section 3.4.2.1. This was particularly important for TFM imaging in close proximity to the array, to ensure that the directivity of each array element was sufficiently wide for its emitted beam to contribute meaningfully to the signal, rather than merely adding noise.

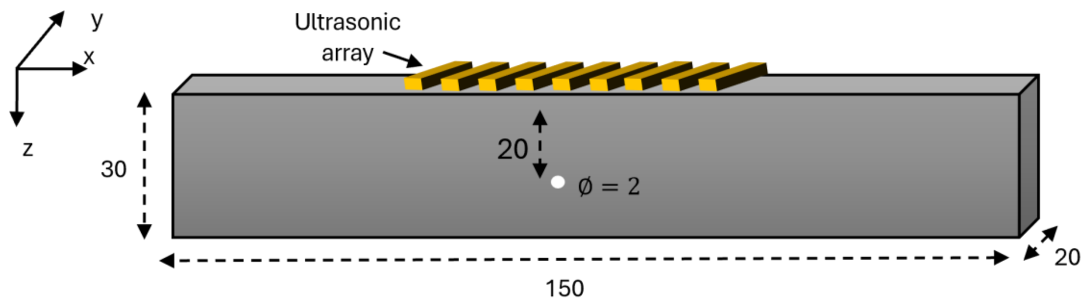

Figure 4. 4: Schematic of the SNR approach acquisition setup. All dimensions are in millimetres (mm).

The element spacing of the 5 MHz and the 10 MHz arrays adhere to the half a wavelength criterion, and therefore, this threshold angle will be excluded from consideration. For the 20 MHz case, the directivity angle was computed as $\theta_{-6dB} = 22.23°$. The -6 dB width, determined using trigonometric principles considering the location of the target (z) as defined in Equation 4.3, was measured to be 7.86 mm. Hence, an 8-element sub-aperture was used for the analysis. The schematics of the sub-aperture selection technique is shown in Fig. 3.5 (b). The -6 dB width ($w_{-6\,dB}$), which corresponds to the size of the sub-aperture, varies depending on the location in the z direction of the target.

$$w_{-6\,dB} = 2z\tan(\theta_{-6dB}/2) \tag{4.3}$$

The arrays were excited with a single-cycle excitation at 80 V p-p, with 40 dB of receive gain. TFM images were produced with the spatial pitch consistently maintained at 8 pixels per wavelength across all cases. Table 4.2 lists the key parameters considered in this evaluation. Fig. 4.5 (a) illustrates an example of the SNR approach for the 20 MHz case. To account for sidelobe artifacts, the noise level region ***nr*** was divided into two sub-regions, nr_u and nr_d, leading to a substitution of the SNR expression in Equation 4.2 with that in Equation 4.4. This approach averages the results from the two sub-regions in order to closely estimate the noise from the defect depth, while excluding the sidelobe artifacts in the noise calculations. The region $\boldsymbol{r}$ surrounding the target is highlighted by a white square in Fig. 4.5 (a), where $a_s = 40\,pixels$. The noise level was measured using a window size, b_n, that varied in size proportional to the wavelength. The SNR technique results are shown in Fig. 4.5 (b). In all cases, the SNR starts to stabilise at around 6 wavelengths. It can also be observed that the SNR of the 10 MHz array is higher than both the 5-MHz and the 20-MHz arrays. Compared to the 5 MHz array, this can be attributed to the smaller aperture. Although both arrays use 64 elements in data acquisition, the 5 MHz array has a pitch of 0.55 mm and the 10 MHz features a finer pitch of 0.25 mm. Moreover, an additional factor potentially contributing to the higher SNR of the 10 MHz array relative to the 5 MHz array may be the piezoelectric material used, although this is not specified in the datasheet provided by the manufacturer. In relation to the 20 MHz array, it can be attributed to the piezoelectric material and the operating frequency. The TFM images for the 5 MHz and the 10 MHz arrays are presented in Fig. 4.5 (c) and (d), respectively.

$$SNR = 20\,log_{10}\left(\frac{A_{max}(r)}{\frac{\sqrt{\left(A_{noise}(I_{nr_u})^2\right)} + \sqrt{\left(A_{noise}(I_{nr_d})^2\right)}}{2}}\right) \tag{4.4}$$

Table 4. 2: Parameters considered in the SNR evaluation approach evaluation. The spatial pitch was maintained at 8 pixels per wavelength. The longitudinal velocity of the steel was 6000 m/s. The wavelength was obtained from the longitudinal velocity relative to the array frequency.

Array frequency (MHz)	Wavelength (mm)	Pixel size (mm)
5	1.2	0.15
10	0.6	0.075
20	0.3	0.0375

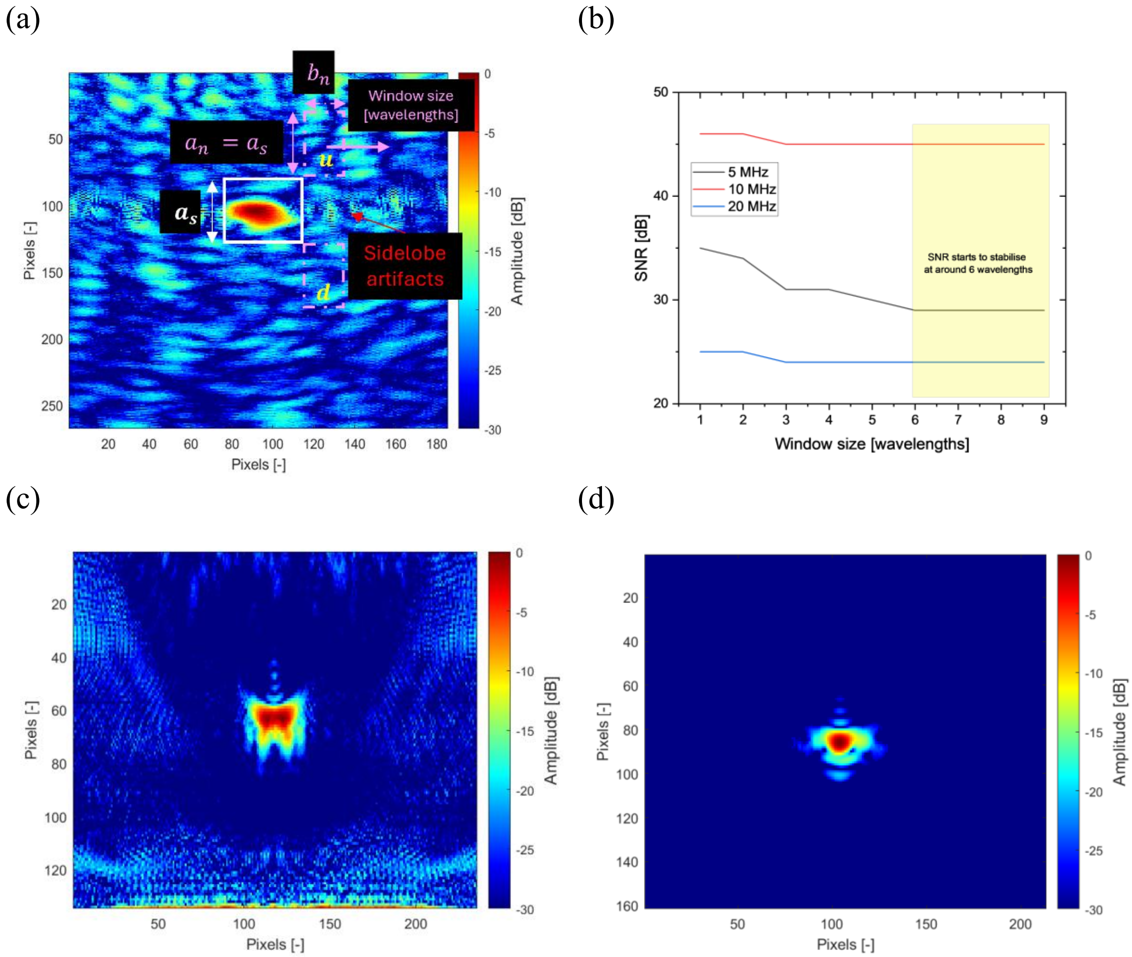

Figure 4. 5: SNR approach evaluation. (a) Example of the SNR approach for the 20 MHz array. The 5 MHz and the 10 MHz arrays followed the same approach. (b) SNR approach results for 5 MHz, 10 MHz and 20 MHz. SNR starts to converge at around 6 wavelengths. The 5 MHz and 10 MHz array used 64 elements in FMC acquisition due to the phased array controller capabilities. The 20 MHz array used an 8-element sub-aperture due to the array element directivity considerations. (c) TFM image for the 5 MHz array. (d) TFM image for the 10 MHz array.

4.4.2. Excitation Strategies: Performance Evaluation and Comparison

This sub-section addresses a comparative analysis involving the conventional pulse and the modulated Barker and chirp excitation strategies using the 20 MHz array. A simulation was conducted using the Verasonics Vantage software and used to compare with experimental results. The simulation involved the array deployed on an acoustic medium (longitudinal velocity of 6000 m/s) consisting of a single point target (dimensionless, modeled as an ideal scatterer, as defined by the software), as depicted in in Fig. 4.6. The experimental configuration involved the array coupled to the planar S355 steel specimen in the same manner as illustrated in Fig. 4.4. For both simulation and experimental cases, the excitation used a single-cycle pulse averaged over 9 frames, a 14-26 MHz, 60% Tukey windowed chirp (1.34 μs) and a Barker 13 (0.74 μs) signals. The Barker and chirp signals exhibited equivalent energy levels of 0.42 a.u. Using the trapezoidal method, a 9-cycle pulse excitation possessed an energy of 0.43 a.u., which closely matched the energy of the coded excitation signals. For a more robust comparison, a single-cycle excitation was averaged over 9 frames to represent the 9-cycle pulse excitation energy. Full matrix acquisition was employed in both simulation and experimental cases.

The received simulated signals were supplemented with noise aligned with the experimental noise data. The superimposition of experimental noise onto simulated ultrasonic signals has been previously employed to enhance the robustness of deep learning models in NDT [116]. Hence, for the pulse excitation case, the approach involved selecting A-scans from the FMC of the experimental data. Five hundred sample points from a region lacking meaningful information from those A-scan signals were extracted. For the coded excitation cases, the experimental uncompressed FMC data was first compressed through a matched filter. A-scan signals from the compressed experimental FMC data were then selected, with 500 sample points extracted from a region devoid of meaningful information. A histogram of the extracted experimental noise data was generated, as shown in Fig. 4.7 (a), overlayed with a fitted normal distribution curve. The next step obtained noise from the normal distribution of the experimental noise data, characterised by the specified mean and standard deviation, for example, -0.03 a.u. and 7.7 a.u, respectively, for the pulse excitation case. Each element of the noise matrix is a number that mimics the statistical properties of the experimental noise data, and is congruent with the simulated FMC matrix. This noise was subsequently superimposed onto the simulated data to improve its accuracy. Fig. 4.7 shows an example of relevant data to aid the readers understand this process.

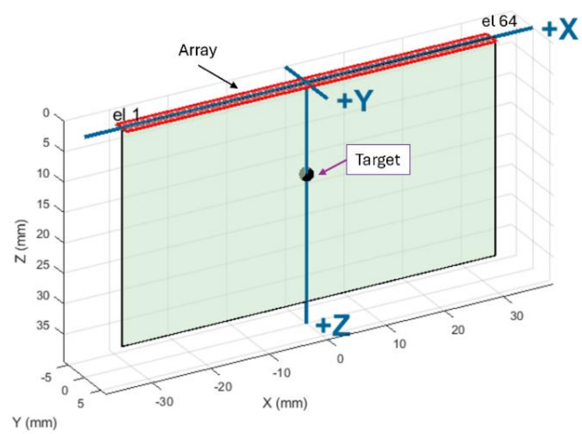

Figure 4. 6: Simulation configuration. The 20 MHz 64 element 1 mm pitch linear array deployed on an acoustic medium (longitudinal velocity of 6000 m/s) with one point target. Elements 1 and 64 are highlighted.

(a)

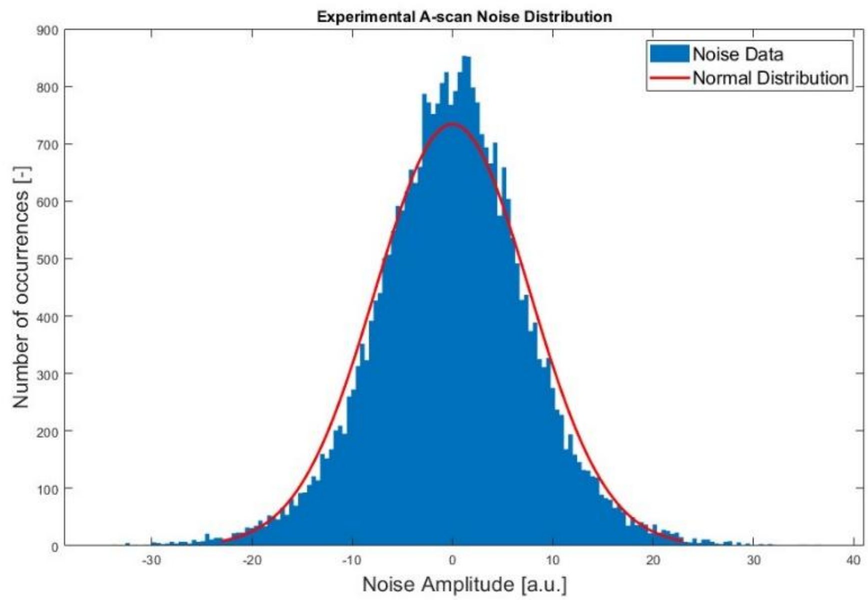

(b)

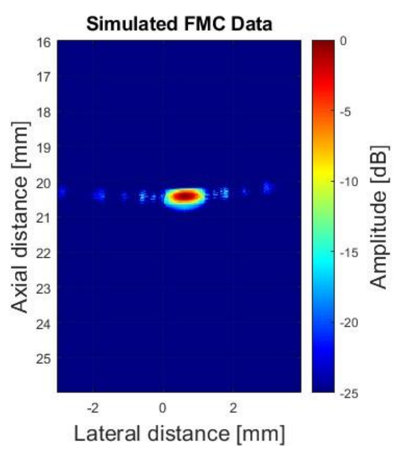

(c)

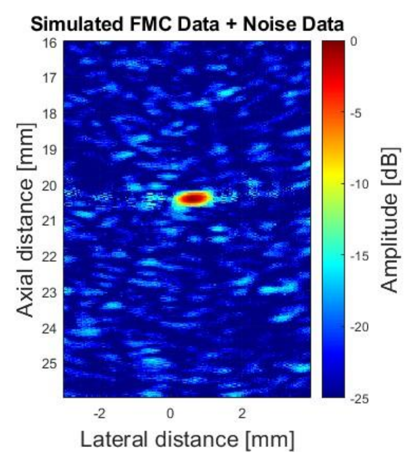

Figure 4. 7: Superimposition of noise onto simulated signals. (a) Histogram of the extracted experimental noise data. (b) TFM based on the noise-free simulated FMC data.(c) TFM of the simulated FMC data supplemented by the noise.

The TFM images for both the simulation and the experimental work corresponding to the 1 cycle pulse, Barker and chirp excitation signals are depicted in Fig. 4.8 (a) – (h). The dynamic range of the images was set to 25 dB to help assess the imaging performance of the excitation schemes. The characteristics of the simulated data agrees well with the experiments, in which all of the TFM images show sidelobe artifacts and the coded excitation cases show matched filter processing artifacts. Fig. 4.8 (c) and (g) show examples of the sidelobe artifacts in dashed pink rectangles and matched filter processing artifacts in dashed white rectangles. Fig. 4.8 (b) and (f) show TFM images of the simulated and experimental uncompressed chirp responses, respectively. The images show poorer axial resolution and lower imaging quality compared to when pulse compression is applied to the chirp signal, as shown in Fig. 4.8 (c) and (g) for the simulated and experimental cases, respectively. These highlight the limitations of not applying pulse compression in improving imaging performance. In comparison to the 1 cycle pulse excitation, the compressed coded excitation schemes demonstrated improvement in overall image quality.

Simulated images (a – d)

(a) 1 cycle excitation

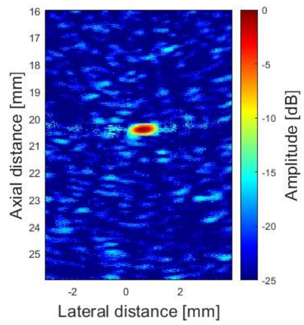

(b) Uncompressed chirp

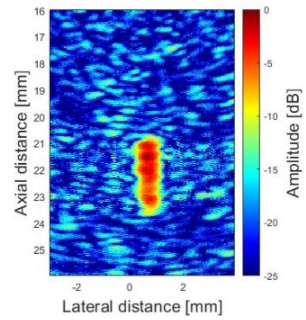

(c) Compressed chirp

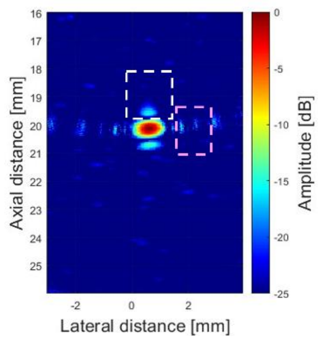

(d) Barker

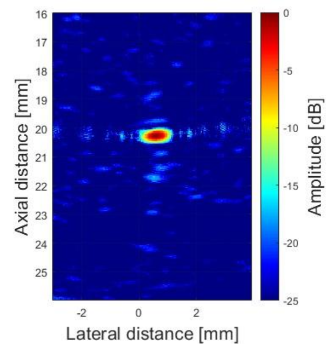

Experimental images (e – h)

(e) 1 cycle excitation

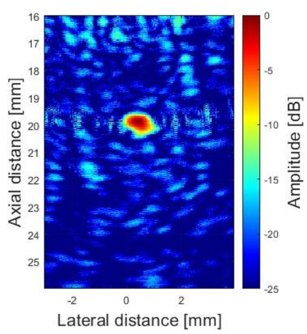

(f) Uncompressed chirp

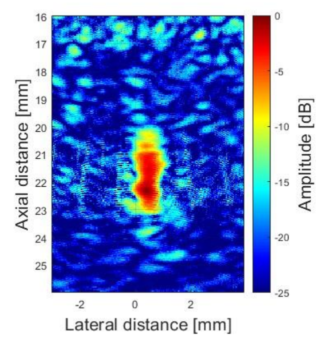

(g) Compressed chirp

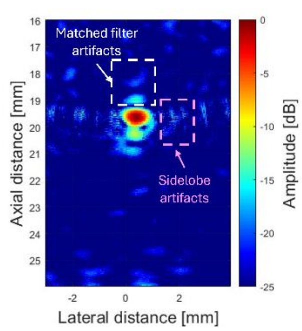

(h) Barker

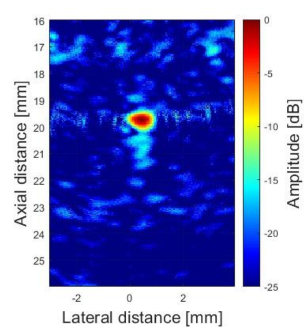

Figure 4. 8: Imaging performance evaluation. (a) – (d) TFM images of the simulated data of the 1 cycle pulse excitation, uncompressed chirp, compressed chirp and Barker, respectively. (e) – (h) TFM images of the experimental data of the 1 cycle pulse excitation, uncompressed chirp, compressed chirp and Barker, respectively. The signals used were a single-cycle pulse averaged over 9 frames, a 14-26 MHz, 60% Tukey windowed chirp (1.34 μs) and a Barker 13 (0.74 μs). An 8-element sub-aperture was employed to account for the array element directivity.

Equation 4.4 was employed to quantify the SNR and Fig. 4.9 depicts the experimental and the simulated SNR values corresponding to the 1 cycle pulse excitation, Barker and chirp coded excitation signals. The behaviour observed in the simulated data agrees well with that of the experimental results. The simulation accurately models the excitation signals and the matched filter. The model accounts for the longitudinal velocity of the inspected medium, however, it does not capture the microstructure of the polycrystalline material. The deviation in the response of the experimental chirp signal from the simulation is attributed to its inherently broadband nature, spanning an extensive frequency range. The experimental conditions may suppress higher frequencies, reducing certain components of the chirp signal, an effect that is not accounted for in the simulation model. For the Barker case, the phase structure of its code is essential for effective pulse compression. The experimental scenario may introduce imperfections in the transmitted signal, disrupting its integrity particularly during the pulse compression stage. This may impact the compression performance as well as resulting in an increase in matched filter processing artifacts. These imperfections contrast with the simplified assumptions in simulations. Other aspects that affect the experimental conditions and, thus, are not accounted for in the simulation include array transducer element performance variability. Due to manufacturing or aging effects, elements in the ultrasonic array will exhibit variations in performance – the simulation model assumes uniform element performance, ignoring these practical inconsistencies. In addition, direct contact between the ultrasonic array and the test specimen also introduces coupling-related losses in the experimental conditions that are not accounted for in the simulation model. The coded excitation schemes achieved higher SNR compared to the pulse excitation case. This results from the pulse compression by the matched filter in the coded excitation cases, which enhances the signal amplitude relative to the noise. Additionally, chirp outperformed the Barker case. The experimental pulse excitation case achieved an average SNR of 24 dB. In contrast, the Barker coded excitation yielded an average SNR of 26.6 dB, while the chirp excitation produced an average SNR of 28.5 dB. Compared to the pulse excitation case, the Barker scheme offered an SNR improvement of 2.6 dB, whereas the chirp strategy provided an enhancement of 4.5 dB. The higher performance of the chirp over Barker is attributed to its broadband characteristics, incorporating multiple frequency components during transmission as opposed to the single-frequency Barker signal. Although both excitation cases offer filter artifacts, these findings suggest that the filter artifacts are more pronounced in the Barker case relative to chirp. Overall, while averaging the single-cycle pulse excitation enhances SNR, it comes at the cost of reduced acquisition speed. Coded excitation techniques improve SNR without sacrificing acquisition speed by utilising extended coded pulses instead of repeated pulses.

The experimental and simulated data was also used to assess the performance of the target signal in relation to the imaging artifacts. Table 4.3 presents the summary of all the measurement results, which included the SNR, the signal-to-sidelobe artifact ratio (SSR), and signal-to-filter artifact ratio (SFR), all deriving from the TFM images of the planar sample. The filter refers to the matched filter used to compress the received coded excitation signals. Equation 3.6 was employed to quantify the SSR, except that the noise level was determined as the RMS from a region where the sidelobes were evident, as highlighted in the dashed pink rectangle in Fig. 4.8 (g). Equation 4.4 was employed to quantify the SFR, except that the two sub-regions nr_u and nr_d represented the locations of the matched filter artifacts, as depicted in the dashed white rectangle (for the upper case) in Fig. 4.8 (g). The experimental results corresponding to the SSR case indicate that the sidelobe artifacts do not degrade with the implementation of the coded excitation schemes. This agrees with the simulated data that was superimposed with noise derived from the normal distribution of the experimental noise data. With respect to the SFR, no response is reported for the pulse excitation case as it employs a conventional, non-modulated waveform that does not require pulse compression. Moreover, the reported experimental results show a comparable performance for both coded excitation schemes, which is attributed to experimental conditions effects. The simulated data, with the supplemented noise, indicates that chirp exhibits higher SFR in relation to the Barker case, implying that the matched filter artifacts are more prominent in the Barker case – this can be clearly observed in the simulated images TFM images in Fig. 4.8 (c) and (d) for the chirp and Barker cases, respectively. Overall, for both SSR and SFR measurements, variations, as discussed earlier, occur between the simulated and experimental data.

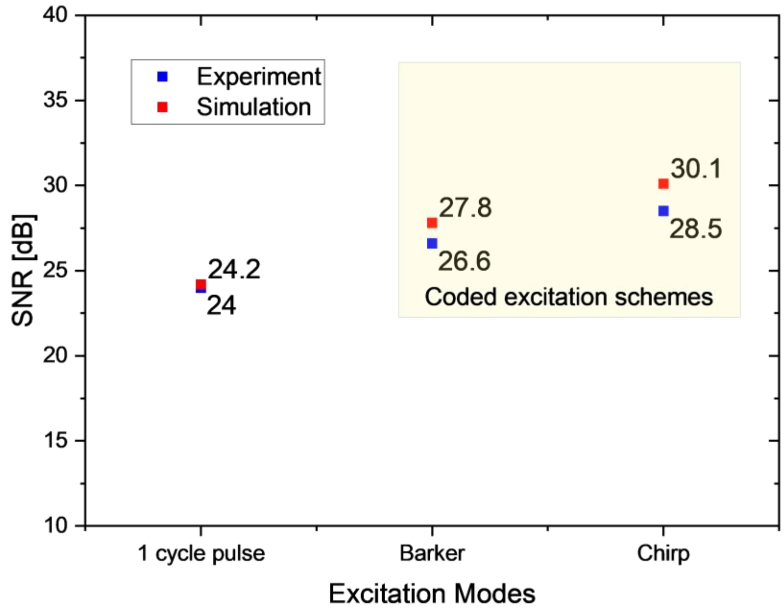

Figure 4. 9: Experimental and simulated SNR values measured for different excitation modes. The simulated data closely aligns with the experimental results, with coded excitation schemes achieving higher SNR compared to pulse excitation.

Table 4. 3: Experimental results of the SNR, the signal-to-sidelobe artifact ratio (SSR), and signal-to-filter artifact ratio (SFR), obtained from the TFM images of the planar test specimen. The filter corresponds to the matched filter utilised for compressing the received coded excitation signals. The terms "Ave" and "SD" represent the average and the standard deviation values, respectively.

Excitation modes	SNR			SSR			SFR		
	Experimental		Simulation	Experimental		Simulation	Experimental		Simulation
	Ave (dB)	SD (dB)	Value (dB)	Ave (dB)	SD (dB)	Value (dB)	Ave (dB)	SD (dB)	Value (dB)
Pulse	24	1.3	24.2	21.2	1.2	23.6	–	–	–
Barker	26.6	0.8	27.8	22.7	1.8	25.9	21	2.2	26
Chirp	28.5	0.5	30.1	22.8	1.6	26.3	21	2.2	28.9

An example of the evaluation of the imaging artifacts is presented in Fig. 4.10. A TFM image of the Barker case is shown with the lateral and axial cross-sections through the central axis of the target. The mainlobe, contributions from sidelobes, matched filter artifacts and noise are highlighted

The pulse compression filter utilised in this study is based on the matched filter, a widely adopted technique for pulse compression [85]. A comparative analysis was performed using the chirp coded excitation strategy, evaluating the matched filter against a mismatched filter. Mismatched filters have been studied and analysed for range (axial direction) sidelobe reduction [85]. However, these filters widen the mainlobe, leading to a reduction in axial imaging resolution relative to the matched filter [85]. Fig. 4.10 shows the pulse compression filter evaluation. TFM images of the chirp coded excitation signals processed with matched and mismatched filters are presented in Fig. 4.11 (a) and (b), respectively, with the axial profile indicated by a dashed white line. Their axial cross-sections are presented in Fig. 4.11 (c). The mismatched filter was designed using a time-reversed chirp signal weighted by a Chebyshev window. As expected, the mismatched filter resulted in a wider mainlobe, with a percentage difference of 13.3 %, in relation to the matched filter, consequently leading to a reduction in axial resolution.

(a) TFM of Barker excitation

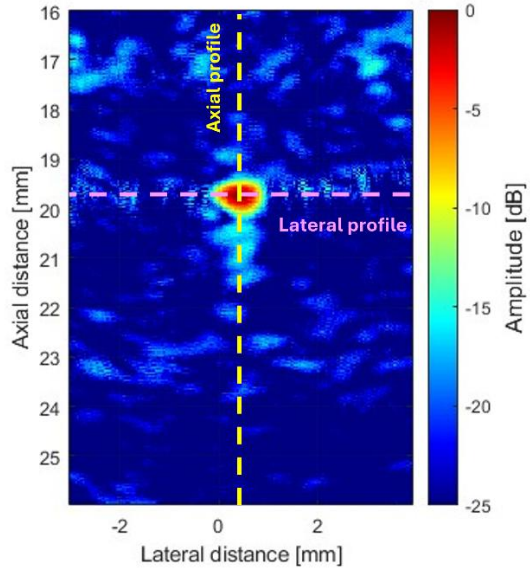

(b) Lateral profile

(c) Axial profile

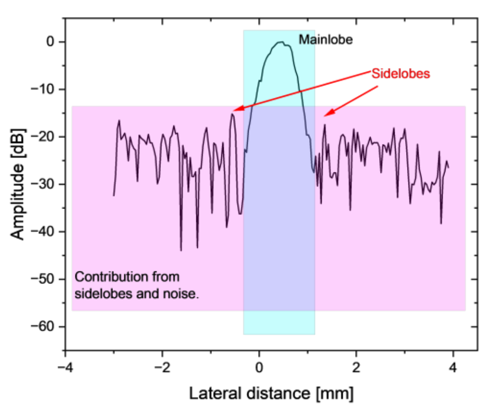

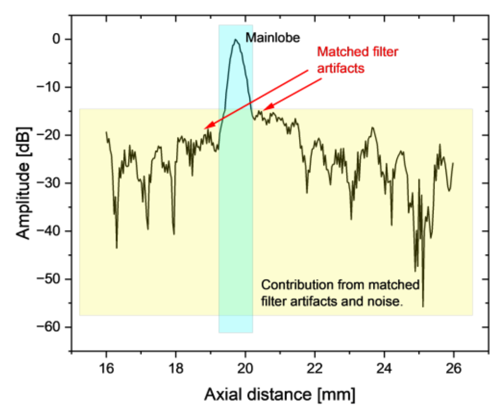

Figure 4. 10: Evaluation of imaging artifacts example. (a) TFM of the Barker coded excitation with the lateral and axial profiles highlighted in dashed pink and yellow lines, respectively. (b) Lateral cross-section of Fig. 4.10 (a) with the mainlobe and contribution from sidelobes and noise highlighted. (c) Axial cross-section of Fig. 4.10 (a) with the mainlobe and contribution from matched filter artifacts and noise highlighted.

(a) Chirp TFM matched filtered (b) Chirp TFM mismatched filtered

(c) Axial profile for matched and mismatched filters

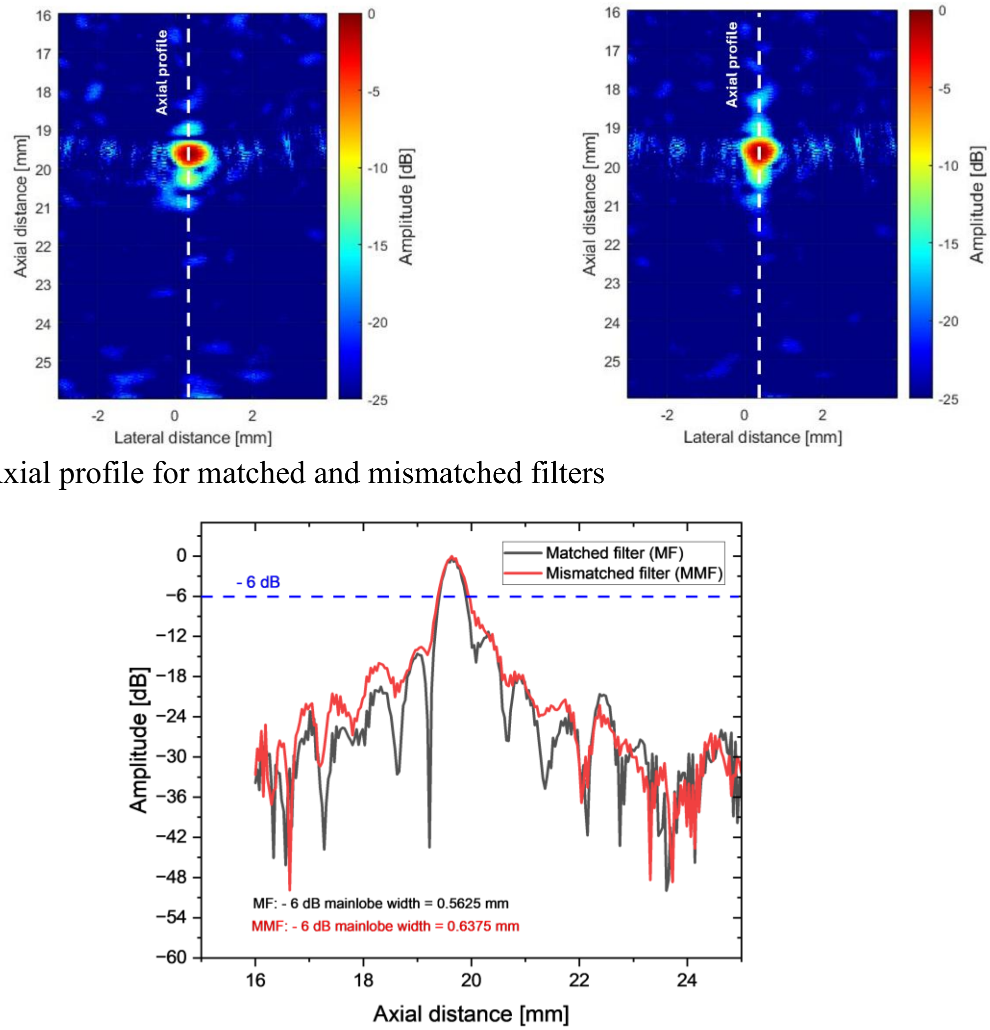

Figure 4. 11: Pulse compression filter evaluation. (a) TFM image of the chirp coded excitation signal processed with a matched filter. (a) TFM image of the chirp coded excitation signal processed with a mismatched filter. (c) Axial cross-section of the TFM images in (a) and (b). The matched filter resulted in a narrower mainlobe (0.075 mm) compared to the mismatched filter, which improves axial imaging resolution.

4.4.3. Complex-Geometry Test Specimens

This sub-section presents investigations conducted on a convex and a concave test specimens. This demonstrates a direct alignment with the increasing challenge of performing ultrasonic NDT on complex industrial components by employing flexible ultrasonic arrays as alternative option to bespoke wedges for surface conformity. To comply with the convex sample, the ultrasonic array should bend inwards in form of a concave array which promotes an increased overlap of beam directivity from the individual array elements leading to a converging beam. The concave sample however induces a divergent beam [8, 10, 117]. Given the difference in beam directivity of the two cases, it is important to investigate the array performance under the proposed coded excitation schemes for both geometric scenarios.

The first experiment compares qualitatively and quantitatively the phase and frequency coded excitation schemes on a convex S355 steel test specimen. The results of a single-cycle excitation averaged over nine frames are presented for reference. The schematics of the convex sample with two machined targets (side-drilled holes), each with a diameter of 2 mm and a length of 20 mm, drilled laterally into the sample, is illustrated in Fig. 4.12. The targets are located 10 mm apart axially and 15 mm apart along the lateral direction. Full matrix data was subsequently acquired in a pulse-echo configuration using the ultrasonic array. The array was magnetically placed in direct contact with the test specimen using two neodymium magnetic discs, each 10 mm in diameter and 5 mm thick. The primary acquisition parameters for this experiment comprised 80 V p-p and a receive gain of 40 dB. The single-cycle, along with the phase- and frequency-modulated signals were employed to excite the ultrasonic array and TFM images were produced.

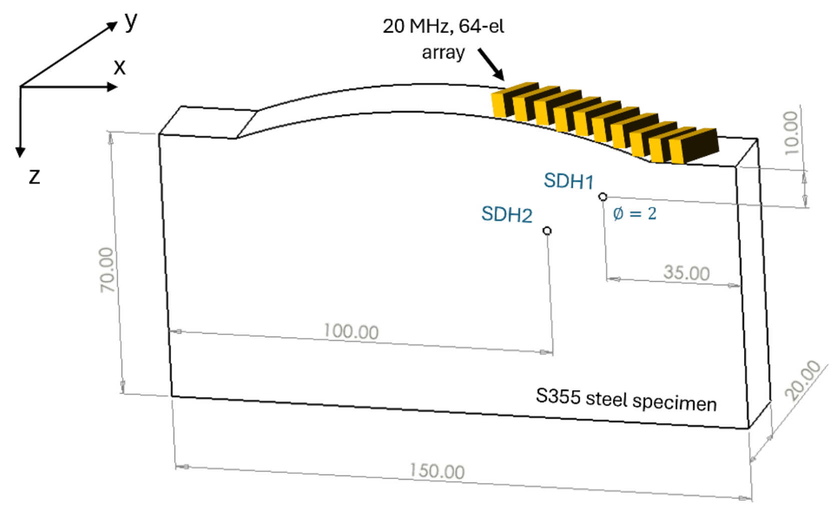

Figure 4. 12: Schematics of the S355 steel convex test specimen with a radius of curvature of 150 mm. The arrangement of the SDHs is displayed. The 20 MHz, 64-element array was magnetically placed in direct contact to the sample. The dimensions are in millimetres (mm).

Fig. 4.13 (a) – (f) depict TFM images corresponding to the region of interest. To evaluate the imaging quality for each excitation technique, the dynamic range was set to 25 dB. Using the sub-aperture calculation technique, as explained in sub-section 4.4.1. and detailed in [26], a 6-element and a 12-element sub-apertures were deduced to produce images at targets 1 and 2, respectively. For both targets, the coded excitation techniques offered better imaging quality compared to the 1 cycle excitation case. Lateral sidelobe artifacts, appearing at a comparable range to the target, are evident in the TFM images in Fig. 4.13 (a), (b) and (c) corresponding to the pulse, Barker and chirp excitations, respectively, at target 1. They arise due to the acoustic beam pattern and the spatial undersampling inherent to the ultrasonic array configuration. The TFM images corresponding to target 2 for all excitation modes, as depicted in Fig. 4.13 (d) - (f), exhibit sidelobe artifacts partially, however, the elevated noise level associated with increasing depth dominates the image noise. Moreover, matched filter processing artifacts, manifested as axial sidelobes within the image, were observed in the TFM images in Fig. 4.13 (b) and (c) corresponding to the Barker and chirp excitations, respectively, at target 1. Fig. 4.13 (e) and (f), corresponding to the Barker and chirp, respectively, at target 2, do not exhibit filter artifacts. This is caused by the rising noise level resulting from the increase in depth. The pulse excitation case, a non-modulated waveform, does not necessitate pulse compression, thereby eliminating the expectation of processing filter artifacts at either target location. The SNR, SSR, and the SFR were quantified, with the average results displayed in Fig. 4.16 and the complete measured values detailed in Table 4.4. For targets 1 and 2, the coded excitation schemes achieved superior SNR compared to the pulse excitation case. This improvement stems from the application of the matched filter in the coded excitation case, which compresses the signal and improves its amplitude in relation to the noise. The consistently higher SNR in target 1 compared to that of target 2, for all excitation cases, is attributed to the energy increase resulting from the converging arc of the convex sample, improving beam focusing. Furthermore, the lower SNR in target 2 is influenced by increased depth, introducing greater attenuation – an effect amplified by the 20 MHz operating frequency of the array. The SSR results indicate that the sidelobe artifacts do not degrade with coded excitation. The average SSR measured for target 1 for the pulse, Barker and chirp are 18.5 dB, 18.7 dB and 19 dB, respectively. No evident sidelobe artifacts were observed for target 2, as noted earlier. The SFR results indicate that chirp outperformed Barker. This is attributed to the performance of the chirp signals relative to the Barker, and suggests that the filter artifacts are higher in the Barker case relative to chirp.

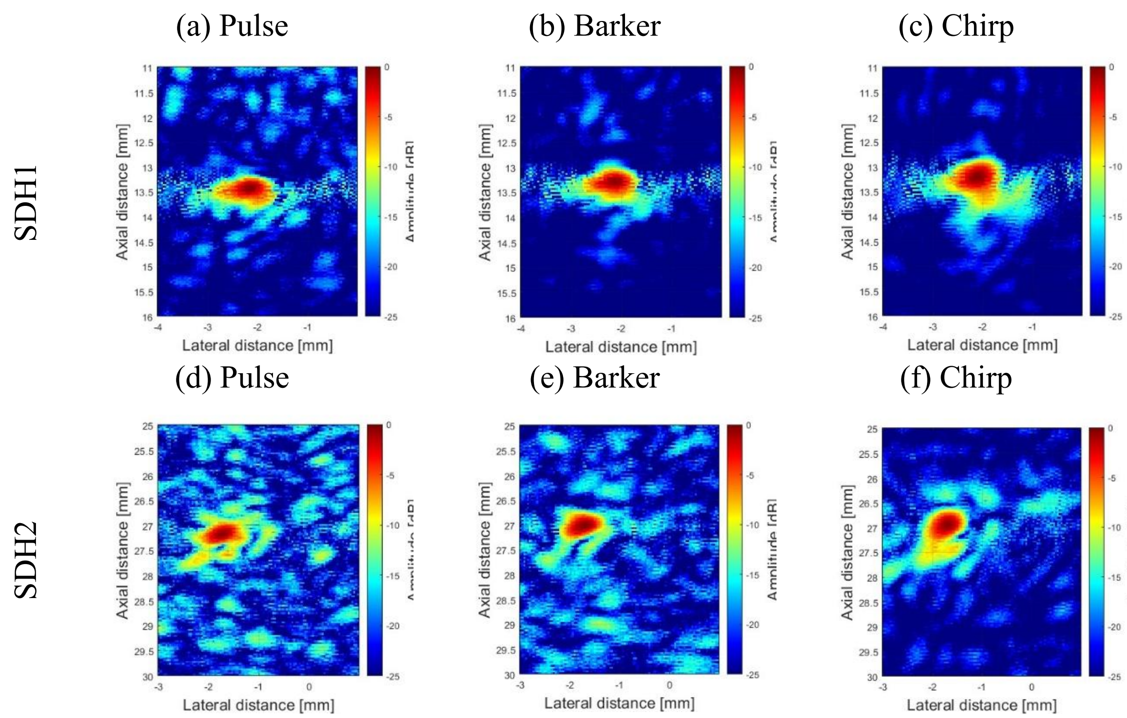

Figure 4. 13: TFM images of the convex sample for different excitation signals. (a) TFM image corresponding to target 1 for the 1 cycle excitation case averaged across nine frames. (b) TFM image corresponding to target 1 for the Barker case. (c) TFM image corresponding to target 1 for the chirp case. (d) TFM image corresponding to target 2 for the 1 cycle excitation case averaged across nine frames. (e) TFM image corresponding to target 2 for the Barker case. (f) TFM image corresponding to target 2 for the chirp case.

The second experiment in this sub-section compares qualitatively and quantitatively the phase and frequency coded excitation schemes on a concave S355 steel test specimen. Results from a single-cycle excitation, averaged over nine frames, are additionally provided for reference. The schematics of the concave test specimen is presented in Fig.

4.14. It includes two machined side-drilled holes or targets, each measuring 2 mm in diameter and 20 mm in length, drilled laterally into the sample. The targets are positioned 10 mm apart axially and 15 mm apart laterally. Similar to the convex sample, two neodymium magnetic discs were used to magnetically position the array in direct contact with the test specimen. The key acquisition parameters consisted of an excitation voltage of 80 V p-p and a receive gain of 40 dB. To drive the ultrasonic array, the single-cycle along with the phase-modulated Barker and the frequency-modulated chirp signals were utilised in collecting the FMC datasets in a pulse-echo setting, leading to the generation of TFM images.

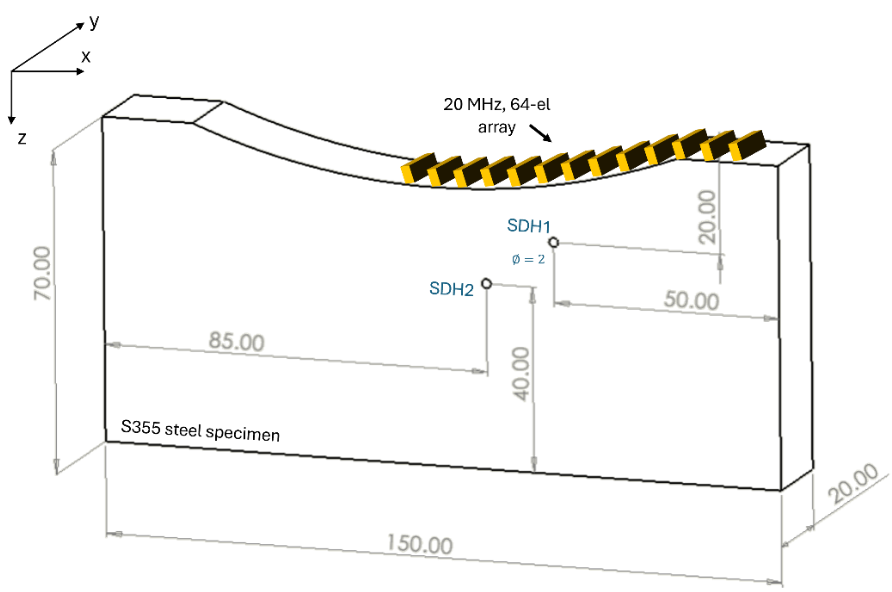

Figure 4. 14: Schematics of the S355 steel concave sample with a radius of curvature of 150 mm. The arrangement of the SDHs is shown. The dimensions are in millimetres (mm).

Fig. 4.15 (a) – (f) show TFM images of the region of interest. The dynamic range was set to 25 dB to assess the imaging quality of each excitation strategy. With considerations given to the sub-aperture selection method, a 5-element and a 7-element sub-apertures were utilised to produce images at targets 1 and 2, respectively. Better imaging quality is observed when employing coded excitation relative to the pulse excitation. Sidelobe artifacts are evident in TFM images in Fig. 4.15 (d) – (f), corresponding to the pulse, Barker and chirp cases, at target 2. These are attributed to the spatial undersampling of the array and its acoustic beam pattern. The elevated noise level, associated with the divergent beam induced by the concave sample, causes TFM images depicted in Fig. 4.15 (a) – (c) to exhibit no imaging sidelobe artifacts. The observed elevated noise level is ascribed to the outward wave divergence from the transducer, stemming from its adaptation to the geometry of the concave sample. The target is positioned nearer to the array than the first target in the convex sample, with the ultrasonic beam displaying complex interference patterns within the near field region. Artifacts due to matched filter and the divergent beam were observed in target 2 in TFM images shown in Fig. 4.15 (e) and (f), corresponding to Barker and chirp cases, respectively. The artifacts evident in the TFM image in Fig. 4.15 (d), corresponding to the pulse excitation case, are attributed to the divergent beam alone, as the pulse excitation employs a non-modulated waveform, not requiring pulse compression. TFM images shown in Fig. 4.15 (a) – (c) show no matched filter or beam-related artifacts, which is attributed to the rising noise level. The SNR, SSR, and the SFR parameters were quantified, with their average values presented in Fig. 4.16 and the full set of measurements reported in Table 4.4. Barker and chirp coded excitations offered higher SNR relative to the pulse excitation case in both targets. This occurs from the use of the matched filter to compress the coded excitation signals and elevate their amplitude relative to the noise. The consistently lower SNR in target 1 in relation to target 2 for all excitation cases is caused by the divergent beam as a result of the concave sample. Furthermore, while the acoustic beam intrinsically exhibits complicated interference patterns that occur near the array, the beam then diverges steadily with a less complicated interference pattern, before its intensity diminishes in the far field. Comparable behaviour was observed in simulations of the acoustic field distribution in convex and concave components with radius of curvatures of 40 mm, using a 16-element array with a 1.17 mm pitch operating at 2.5 MHz [10]. The SSR findings demonstrate that the sidelobe artifacts remain unaffected in terms of degradation under coded excitation conditions. The average measured SSR for target 2 for the pulse, Barker and chirp cases are 19.3 dB, 20.8 dB and 20.9 dB, respectively. No sidelobe artifacts were evident in target 1, as noted earlier. The artifacts in the axial direction, resulting from a combination of filter and the divergent beam in the coded excitation cases, and solely from the divergent beam in the pulse excitation, do not exhibit degradation with the implementation of coded excitation strategies.

Comparing the results from both convex and concave test specimens, the TFM images, as depicted in Fig. 4.13 and Fig. 4.15, respectively, show better imaging quality when employing coded excitations in relation to pulse excitation. Both convex and concave samples exhibit sidelobe artifacts. While the TFM images in the convex sample show evident sidelobe artifacts in target 1, the TFM images in the concave sample depict sidelobe artifacts in target 2. Despite the array spatial undersampling, the sidelobe artifacts in the images are attributed to the acoustic beam pattern, where the convex sample induces a focusing beam, while the concave sample generates a divergent beam. Matched filter processing artifacts are observed in both convex and concave configurations. On the convex sample, they were observed in target 1, and the concave sample exhibited artifacts in target 2. The divergent beam in the concave sample showed further artifacts in the pulse excitation case. With regards to SNR, Barker and chirp outperformed the pulse excitation case for both samples in both targets. The convex sample has the SNR consistently higher in target 1 relative to target 2 at all excitation cases, while the concave sample exhibits the opposite behaviour. This is attributed to the acoustic beam pattern (converging and diverging), and its impact in imaging quality can be clearly observed in the TFM images in Fig. 4.13 and Fig. 4.15. The SSR in both samples indicate that the sidelobe artifacts do not degrade with coded excitation. The SFR in the convex and concave samples show chirp to outperform Barker. The divergent beam in the concave sample introduces further artifacts, which also impacts the pulse excitation image.

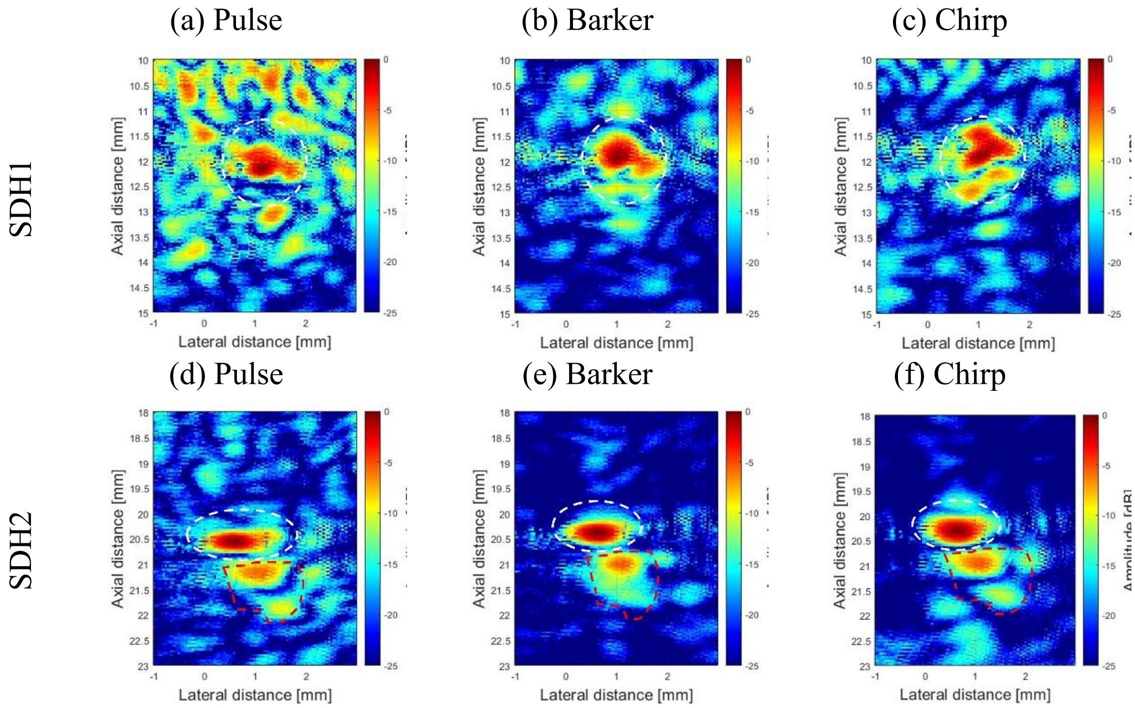

Figure 4. 15: TFM images of the SDH targets in the concave test specimen for different excitation signals. (a) TFM image relating to target 1 for the single-cycle excitation averaged across nine frames. (b) TFM image relating to target 1 for the Barker excitation. (c) TFM image relating to target 1 for the chirp excitation. (d) TFM image relating to target 2 for the single-cycle excitation averaged across nine frames. (e) TFM image relating to target 2 for the Barker excitation. (f) TFM image relating to target 2 for the chirp excitation. The dashed white areas represent the target, and the dashed red areas represent artifacts in the axial direction.

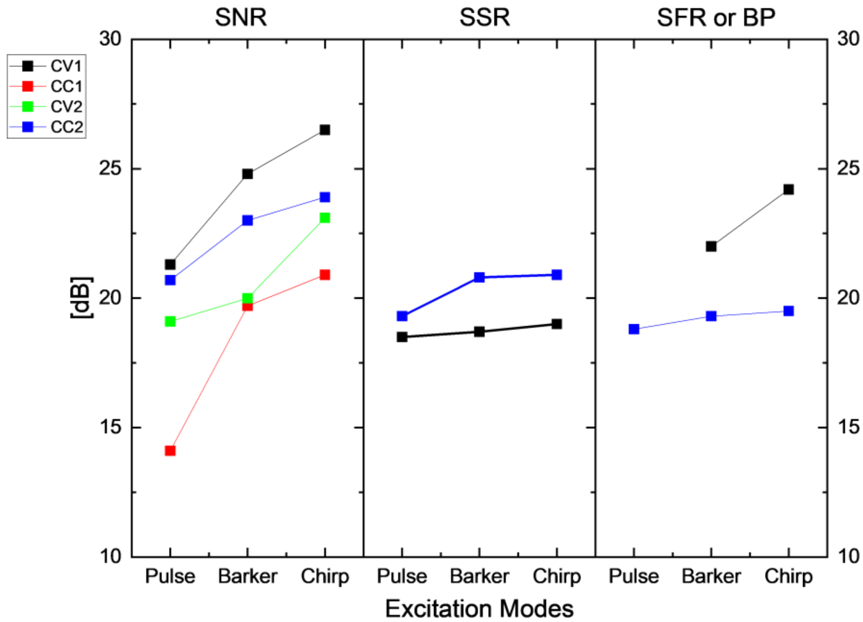

Figure 4. 16: SNR, SSR, and the SFR average values corresponding to the convex (CV) and the concave (CC) test specimens at targets 1 and 2. "BP" represents the beam pattern (converging and diverging).

Table 4. 4: Experimental results of the SNR, SSR and SFR obtained from the TFM images of the convex and the concave test specimens in Fig. 4.12 and Fig. 4.14, respectively. The terms "Ave" and "SD" represent the average and the standard deviation values, respectively, and are expressed in dB. "U" stands for undetected, indicating that a response was not observed. "BP" stands for beam pattern, which considers the effects of the ultrasonic beam on the sample.

Mode	SDH	SNR				SSR				SFR (and/or BP)			
		Convex		Concave		Convex		Concave		Convex		Concave	
		Ave	SD	Ave	SD	Ave	SD	Ave	SD	Ave	SD	Ave	SD
Pulse	1	21.3	2.4	14.1	1.1	18.5	1.1	U	U	–	–	–	–
	2	19.1	1.6	20.7	1.4	U	U	19.3	1.1	–	–	18.8	1.7
Barker	1	24.8	1.9	19.7	1.2	18.7	2.5	U	U	22	1.7	U	U
	2	20	1.9	23	0.6	U	U	20.8	1	U	U	19.3	2.4
Chirp	1	26.5	0.05	20.9	1.5	19	0.8	U	U	24.2	1.1	U	U
	2	23.1	3.5	23.9	0.5	U	U	20.9	0.8	U	U	19.5	0.5

4.5. Conclusion

In this study, a flexible ultrasonic array that is both scalable and RoHS-compliant was used to enhance operability in thick complex-geometry samples. The lead-free array exhibits lower d_{33} value relative to its lead-based counterparts, leading to a reduction in signal quality. Single transmission phase-modulated Barker and frequency-modulated chirp excitation schemes combined with pulse compression were applied to enhance the signal quality of the array.

A comparative study evaluated the single-cycle pulse excitation, Barker and chirp coded excitation strategies with equivalent energy levels for defect detection through TFM imaging through simulation and experiments on a planar defective sample. The evaluation employed a novel SNR approach that examined the characteristics of the image noise region and identified that the SNR started to converge at around 6 wavelengths. The study revealed that the simulated data demonstrated good agreement with the experimental results. Certain discrepancies between experimental and simulated results were noted, which were attributed to imperfections in experimental conditions relative to the simplified assumptions of the simulation model. The inconsistencies consisted of the signal integrity, variations in array element performance and array-to-specimen coupling. The simulation results anticipated enhancement in SNR performance for coded excitation schemes relative to the single-cycle excitation, a finding that was consistently validated through experimental results. Experimentally, the Barker scheme showed an SNR improvement of 2.6 dB, while the chirp scheme achieved a more significant improvement of 4.5 dB. In general, although averaging the single-cycle pulse excitation improves SNR, it results in a trade-off with reduced acquisition speed. The coded excitation schemes improve SNR while preserving acquisition speed through utilising extended coded pulses rather than repeated pulses. Furthermore, all of the TFM images showed sidelobe artifacts, while the coded excitation cases further exhibited matched filter processing artifacts. The subsequent two experiments evaluated the flexibility of the array to determine its effectiveness in enhancing operability in complex-geometry components. The array showed excellent conformity with the convex and concave samples. The coded excitation schemes provided better imaging quality compared to the single-cycle excitation case in both convex and concave scenarios. Both samples exhibited sidelobe and matched filter processing imaging artifacts. The observed sidelobe artifacts were attributed to factors including the array spatial undersampling, and the beam pattern (converging or diverging). The matched filter processing artifacts resulted from the imperfect performance of the filter. The SSR revealed that the sidelobe artifacts do not worsen with coded excitation. While the SFR in both test specimens shows chirp to outperform Barker. In all scenarios, simulation or experimental, the sub-aperture selection technique was implemented, which accounted for the impact of the array element directivity angle.

As a final remark, although the single transmission modulated signals utilised in this study do exhibit processing sidelobes, they offer advantages over the two transmission phase-modulated Golay signals. The latter reduces the data acquisition and frame rate by a factor of two and introduces motion-dependent decoding errors.

Chapter 5

Imaging and Detection of Calcified Plaques in Ex-Vivo Porcine Heart Arteries Using an Intravascular Ultrasound Array with Real-Time Coded Excitations

5.1. Chapter Overview

This work introduces a scalable, RoHS-compliant array transducer (5 French gauge, approximately 1.67 mm diameter), leveraging its fabrication advantages for IVUS imaging. Although the lead-free array exhibits lower piezoelectric coefficient values than its lead-based counterparts, reducing signal quality, its efficacy is demonstrated using frequency- and phase-modulated signals with pulse compression to enhance imaging and detect calcified plaques in *ex-vivo* porcine heart arteries. The array was characterised through electrical impedance analysis and pulse-echo response, with a comprehensive characterisation of the acoustic field presented, based on the transmitted energy in the pulse-echo conditions. The impedance magnitude exhibited uniformly damped responses across all array elements, with the phase angle spectrum indicating resonance at around 21 MHz, and phase variations from approximately $90.7°$ to $91.7°$. The acoustic field characteristics, assessed through experiments and simulation, exhibited higher transmitted energy with three array elements relative to one element, demonstrating strong overall agreement, despite of some discrepancies attributed to imperfections in the experimental conditions. Pulse-echo analysis revealed a peak frequency at 19.22 ± 2.20 MHz, with a -6 dB bandwidth of 66.80 %. Coded chirp and Barker excitation strategies with equivalent energy levels imaged two *ex-vivo* porcine heart arteries and detected the calcified plaques, with chirp offering better imaging quality compared to Barker. A 10-μm thick histological section of an artery, stained with haematoxylin and eosin, was utilised to compare against an IVUS image. The histological images successfully detected the calcified plaque, demonstrating good agreement with the IVUS image. The results underscore the potential of lead-free RoHS-compliant transducers as a sustainable high-performance solution for next generation IVUS systems.

5.2. Introduction

Chapters 3 and 4 have employed a zinc oxide (ZnO) linear ultrasonic array for NDT applications. It involved the application of coded excitation strategies in conjunction with FMC/TFM techniques for inspection of thick convex and concave industrial components. This chapter introduces a 5 French gauge 32-element 163 μm-pitch 3.82 mm-elevation ultrasonic array transducer, allowing radial scanning in *ex-vivo* porcine heart arteries through the selective activation of individual elements with adjustable time delays.

Cardiovascular diseases (CVDs) are the leading cause of death worldwide, responsible for approximately 17.9 million fatalities each year [118, 119]. In Europe, CVDs contribute to approximately 1.8 million deaths annually and exceed 11 million hospital admissions each year. With an aging population, the incidence of numerous CVDs escalates markedly. The associated economic burden and human impact are profound. Overall, CVDs exert a significant economic burden on the European Union (EU), with annual costs approaching 210 billion euros, primarily due to healthcare expenditures and productivity losses [45].

Coronary angiography continues to serve as the gold standard imaging modality for diagnosing coronary artery disease (CAD), and its extensive clinical adoption has been instrumental in guiding patients toward a range of effective interventional therapeutic strategies. X-rays, in conjunction with contrast agents, are employed in coronary angiography to delineate the location and severity of stenosis within affected coronary arteries. Nevertheless, this approach lacks the ability to provide precise insights into vulnerable plaque characteristics and the structural integrity of the vessel wall. It generates only a two-dimensional visualisation of the contrast-filled arterial lumen, failing to image the arterial wall, where the most significant atherosclerotic plaques reside [46, 27]. Moreover, the use of x-rays exposes patients and clinicians to ionising radiation, which can be harmful with repeated procedures.

B-mode ultrasound images consist of the predominant imaging modality in IVUS applications, as it enables real-time acquisition of intuitive two-dimensional cross-sectional images. IVUS systems primarily produce monochrome grayscale images in B-mode, where the brightness of each pixel is directly correlated by the amplitude of the received ultrasound signal [27, 16], [48-55].

This chapter presents novel work on the application of a lead-free and RoHS-compliant ZnO-based array transducer for IVUS imaging. For fast data acquisition and frame rates, single-transmission frequency- and phase-modulated signals are employed, combined with a pulse compression method to improve the signal quality, allowing imaging and detection of calcified plaques in *ex-vivo* porcine heart arteries. The subsequent organisational structure of this chapter is delineated as follow: Section 5.3 presents information on materials and methods utilised in this work. This includes the characterisation of the array. Section 5.3 also includes background information about coded excitation, pulse compression and energy considerations of the transmitted waveforms for an equitable comparative analysis. The preparation process of the *ex-vivo* porcine heart arteries samples was described next through a flowchart, followed by details on the setup configuration, which comprised the array transducer and the Vantage NXT 64LE High Frequency system. The results and discussions are comprehensively detailed in Section 5.4. The array was characterised in terms of electrical impedance and pulse-echo measurements. Coded excitation schemes in forms of chirp and Barker were employed and enabled imaging and detection of calcified plaques in porcine heart arteries. Section 5.5 presents a conclusion of this chapter.

5.3. Materials and Methods

5.3.1. Array Characterisation

In this study, a miniature 32-element array ultrasound transducer was employed, allowing radial scanning through the scanning mechanism and the selective activation of individual elements with adjustable time delays. The IVUS probe was formed using a 3-D printed composite resin, Composite-X (Liqcreate, 3565 CL Utrecht, The Netherlands) inner core by epoxying the array in position, achieving a resulting diameters of 5 French gauge, approximately 1.67 mm. It consists of $163\,\mu$m pitch and 3.82 mm elevation. The characterisation of the array included analyses of the electrical impedance response and the pulse-echo response.

5.3.1.1. Electrical Impedance

The electrical impedance and the phase angle spectra for each element of the IVUS array were measured using an E4990A impedance analyser (Keysight, Santa Rosa, CA, USA) with operational frequencies ranging from 20 Hz to 120 MHz. The impedance analyser was interfaced with a 16047E test fixture (Keysight, Santa Rosa, CA, USA) designed for evaluating frequencies up to 120 MHz. Figure 5.1 shows the layout of the acquisition setup arranged to measure across all the array elements.

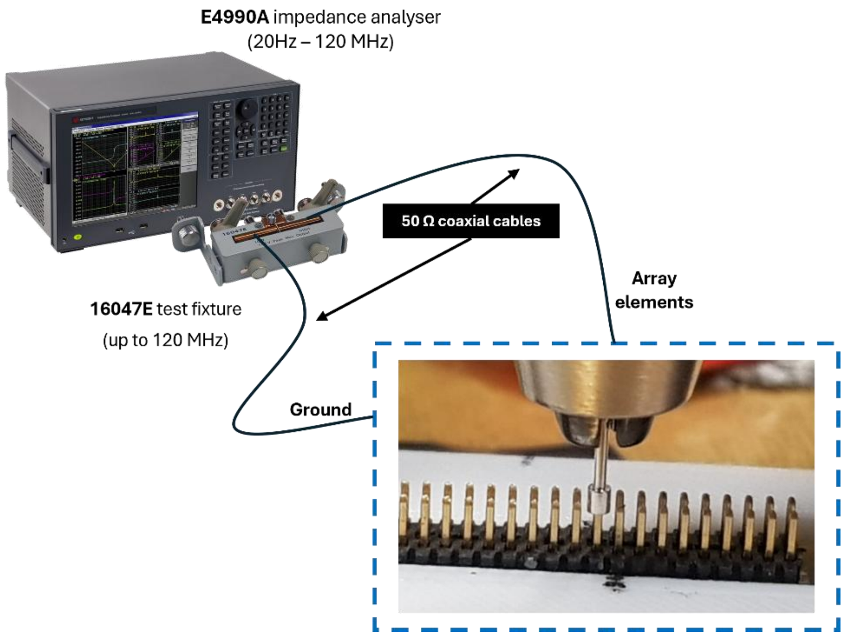

Figure 5. 1: Electrical impedance acquisition setup.

5.3.1.2. Pulse-Echo and Energy Considerations

The acquisition strategy employed for the pulse-echo response used three array elements in transmission, beamformed with differential delays to increase the energy in transmission, and one element in reception. Therefore, assessment of the acoustic field was undertaken. Characterisation of the acoustic field occurred through measurements conducted using a hydrophone mounted in an automated scanning tank filled with deionised (DI) and degassed water. The schematics of the data acquisition configuration is depicted in Figure 5.2, where the signal path is highlighted. The NI PXIe-1071 + 5772 (National Instruments, Austin, Texas, United States) was utilised to trigger the Verasonics Vantage 128^{TM} (Verasonics Inc., Kirkland, USA), which was used to excite the IVUS array. The Vantage 128^{TM} system features a programmable pulser with an amplitude range of 2 to 190 V peak-to-peak, and supports receive frequencies spanning 1 MHz to 50 MHz in its high-frequency configuration, enabling versatile acoustic signal generation and detection. The array was connected to the Vantage 128™ using an ipex female to Hypertronics male adapter, interfaced with a Universal Transducer Adapter (UTA) 160-DH/32 LEMO. A 0.075 mm-diameter polyvinylidene (PVDF) needle hydrophone (NH0075, Precision Acoustics Ltd., Dorchester, UK), with a frequency band between 1 MHz to 60 MHz, was used as a receiver that detected the transmitted acoustic pressure and converted into electrical signals. The hydrophone was connected to a submersible preamplifier and DC coupler that matched the electrical impedance to 50 Ω for efficient signal transfer while offering a small amount of gain to the signal. The submersible preamplifier and DC coupler were connected to a booster amplifier that provided a gain of 30 dB to the signal. This output was captured by the NI PXIe-1071 + 5772 and digitised. A DSO-X 3014A oscilloscope (Agilent Technologies, Inc., Santa Clara, California, USA) was employed to visualise the signal. A custom LabVIEW-based software was used to control the PXIe-1071 and the NI 5772 digitiser. Waveforms were acquired, digitised and stored, while controlled by the scanning tank software, with a sample rate of 800 MHz and 128 averages.

(a)

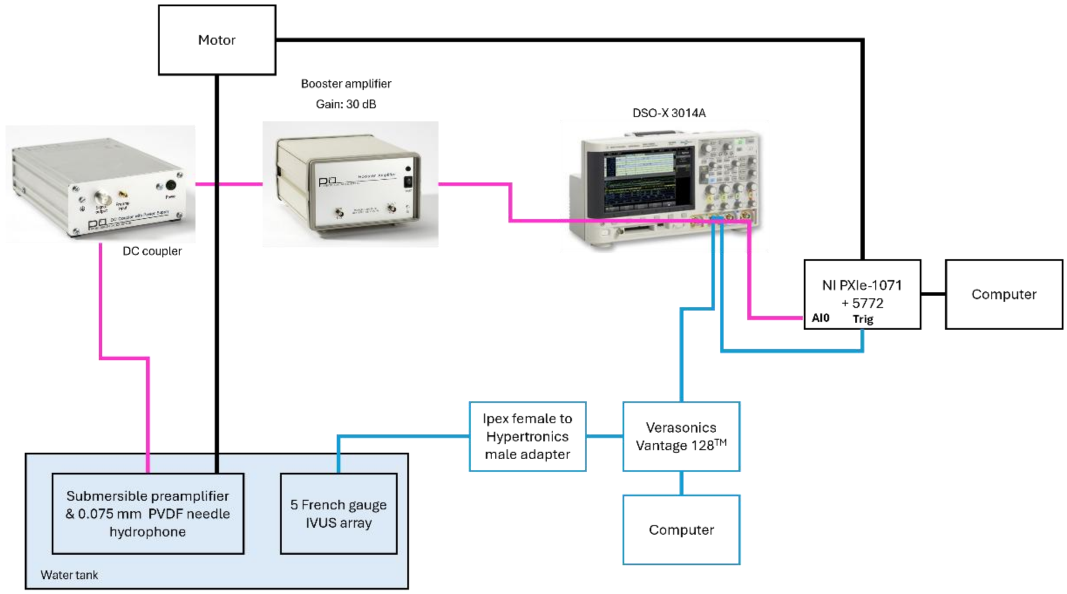

(b)

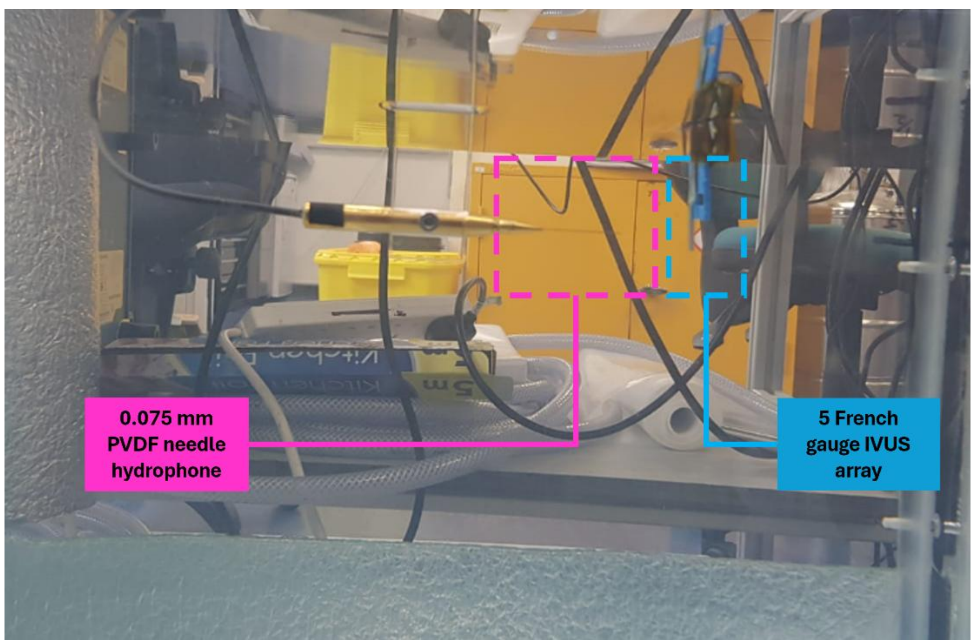

Figure 5. 2: (a) Schematics of the overall acquisition setup for the acoustic field characterisation. (b) Photograph showing the hydrophone and the IVUS array in the water tank. The NI PXIe-1071 + 5772 triggered the Verasonics system to excite the array. The hydrophone received acoustic pressure, converting it to electrical signals. It was connected to a submersible preamplifier and DC coupler, followed by a booster amplifier. The output was digitised by the NI PXIe-1071 + 5772, and visualised on the oscilloscope.

The pulse-echo response of the array was measured using the Vantage NXT 64LE High Frequency system (Verasonics Inc., Kirkland, USA), which features a programmable pulser amplitude adjustable from 3 to 192 V p-p and supports receive frequencies spanning from 1 to 60 MHz in its high-frequency configuration. The array was connected to the Vantage NXT using the same adapter, interfaced with the same UTA, as described in the scanning tank configuration. The analogue-to-digital converter operates at a sampling rate of 125 MHz, with a 16-bit resolution [120]. The configuration parameters including the array, sample and the acquisition strategy for transmission and reception were defined in a MATLAB-based Verasonics environment (MATLAB R2022b). The experimental setup, depicted in Figure 5.3, consisted of the array being immersed in DI water surrounded by a steel tubing (10-mm diameter) that acted as a reflector. The steel reflector offers strong echoes due to its significantly higher acoustic impedance than the surrounding medium.

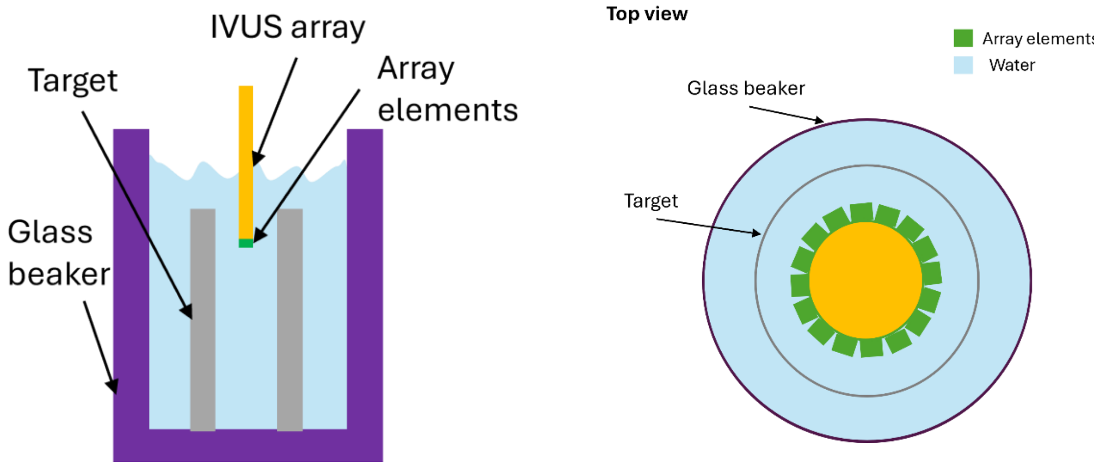

Figure 5. 3: Schematics of the acquisition setup of the pulse-echo experiment and a top view. The IVUS array was connected to the Vantage NXT system.

5.3.2. Coded Excitation and Energy Considerations

This study utilised frequency and phase-modulated signals to excite the IVUS array in real-time. Linear chirps were employed as frequency-modulated signals. The phase-modulated excitation scheme employed was Barker signals. Similar to chirp signals, Barker signals likewise constitute single transmission excitation techniques. These codes were modulated with a half-cycle waveform at 20 MHz and used for excitation.

The excitation signals were designed to have equivalent energy levels, thereby facilitating an equitable comparative evaluation. Consequently, an 18-23 MHz chirp (0.414 μs) and a Barker 5 (0.498 μs), as shown in Fig. 5.4, possessing 0.148 arbitrary units (a.u.) energy, were employed. Their energy was determined through a trapezoidal method to calculate the integral of the squared waveform across the temporal domain [111, 112]. In general, increasing the duration of the transmitted signals intrinsically results in an expansion of the dead zone. Determining the optimal signal length is application-dependent and requires balancing sufficient SNR improvement with minimising the dead zone to maintain near-field target detection performance [26].

(a) Chirp

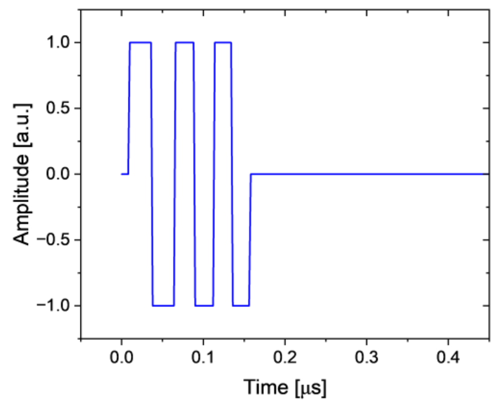

(b) Barker

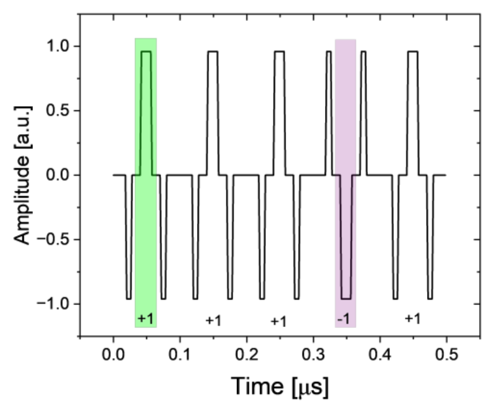

Figure 5. 4: Frequency- and phase-modulated signals used for excitation in tri-level representation. (a) 18-23 MHz chirp signal of 0.414 μs duration. (b) Barker signal of length 5 (0.498 μs). The shaded green area illustrates a positive phase and the shaded purple area highlights a negative phase.

5.3.3. Ex-Vivo Porcine Heart Arteries

This study employed chirp and Barker coded excitation techniques to image *ex-vivo* porcine heart arteries (WETLAB Ltd., Warwickshire, England, United Kingdom) and plaque detection. Fig. 5. 5 shows a flowchart offering an overview of the preparation process of the samples. Phase 1 consisted of placing the porcine heart on a chopping board. In phase 2, the arteries were cut, varying in heights between approximately 25 mm to 40 mm. The arteries were securely immobilised on a foam substrate in phase 3. Phase 4 involved the construction of calcified plaques using calcium carbonate powder (Heiltropfen Lab. LLP, London, England, United Kingdom). Coronary calcification serves as a key indicator of atherosclerotic disease progression [121, 27]. Highly reflective or echogenic structures, including calcifications (or calcified deposits) generate brighter signals, whereas echo-lucent structures, such as lipid deposits, result in substantially reduced signal intensity [54, 27]. Calcium acts as a strong ultrasound reflector, with minimal beam penetration, consequently casting acoustic shadows over deeper arterial structures. In phase 5, the sample was fully prepared.

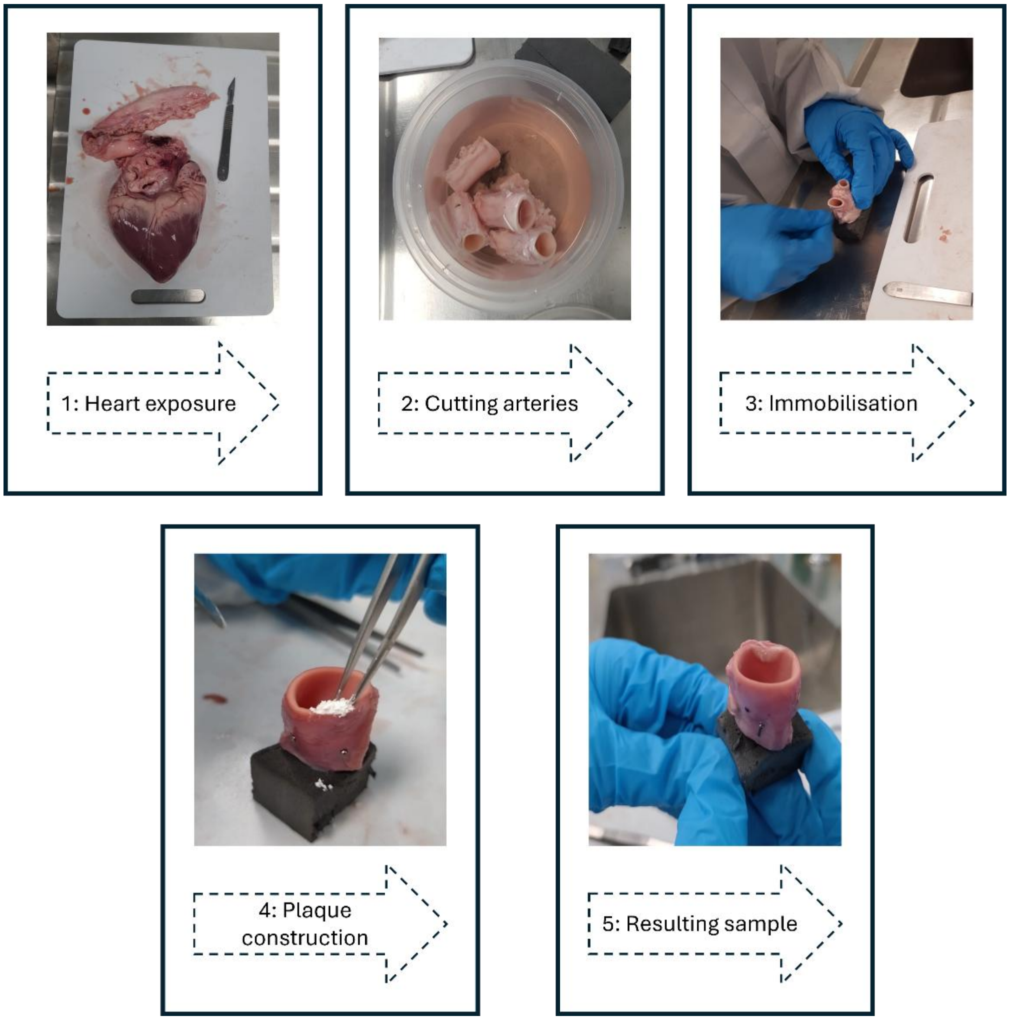

Figure 5. 5: Flowchart providing an overview of the preparation process of the arteries. Phase 1 included placing the porcine heart on a chopping board. The arteries were cut in phase 2. Phase 3 consisted in securely immobilising the heart arteries on a foam substrate. The calcified plaque construction occurred in phase 4. The resulting sample was fully prepared in phase 5.

The setup configuration used a MATLAB-based IVUS system to observe the *ex-vivo* porcine heart arteries, achieving real-time acquisition and image formation of a frame rate of approximately 64 frames per second (fps) for the single transmission coded excitation techniques (Barker and chirp). Fig. 5. 6 (a) shows the configuration comprising the array transducer for radial ultrasound transmission, integrated with the Vantage NXT 64LE High Frequency system for advanced imaging processing and visualisation. The array was immersed in a glass beaker filled with phosphate buffer saline (PBS) and surrounded by the *ex-vivo* arteries, as highlighted in Fig. 5.6 (b). A picture of the array, emphasising its elements is depicted in Fig. 5. 6 (c).

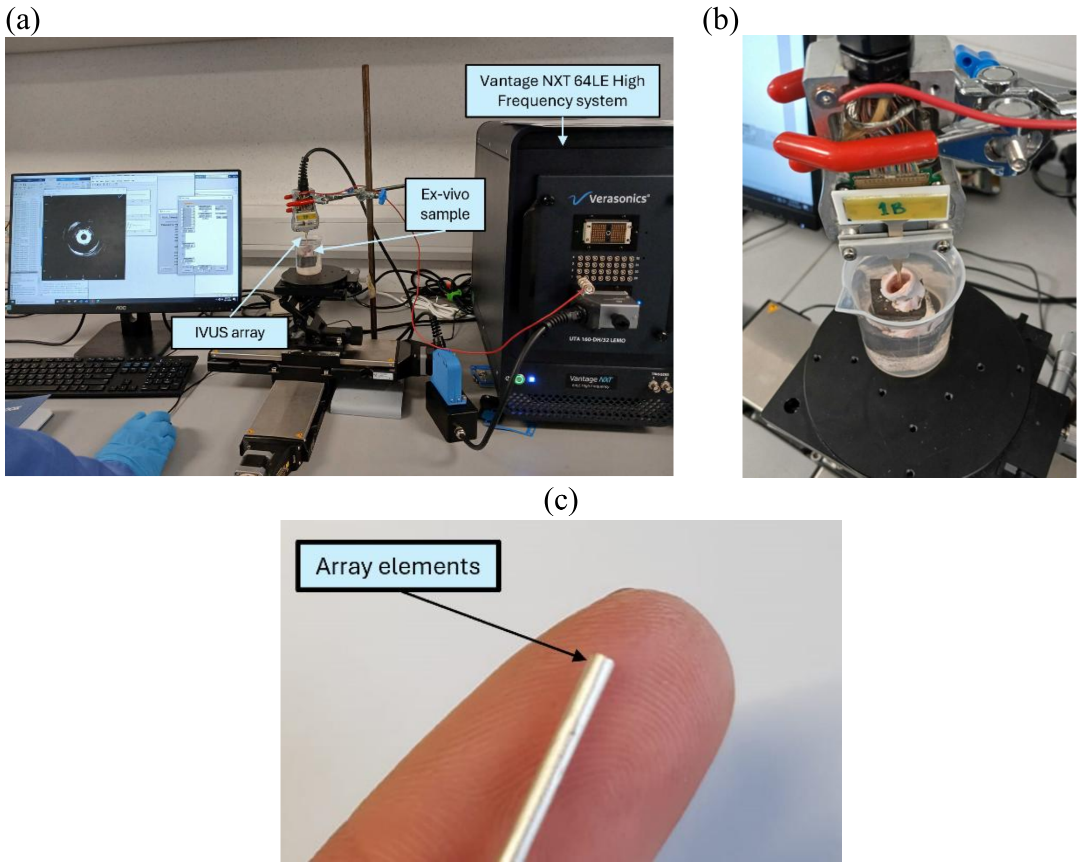

Figure 5. 6: (a) Real-time IVUS system for observing ex-vivo porcine heart arteries. It consists of the array that radially transmits ultrasound signals and the Vantage NXT 64LE High Frequency system for imaging processing and display. The array is securely positioned parallel to the long axis of the vessel wall. (b) A close-up photograph to emphasise the ex-vivo sample. (c) Photograph of the multi-element array highlighting the location of its elements. The configuration of the elements in the array is illustrated in Fig. 2.14 (b).

Histological sections were prepared and compared against an IVUS image. Histological preparations were undertaken at the Histology Laboratory, Anatomy Facility, School of Medicine, Dentistry & Nursing (Thomson Building, University of Glasgow, Scotland, UK). Fig. 5. 7 shows the key steps of the preparation process. An *ex-vivo* porcine heart artery was immersed into a mould (25 × 25 × 15 mm^3) containing FSC22® (Clear Frozen Section Compound, Leica Biosystems, Nussloch, Germany) and cooled in the Leica CM1860 cryostat (Leica Biosystems, Nussloch, Germany), operating at -22 ℃. The FSC22® solidified to form a block that contained the artery. The block was bonded to a holder, by means of the FSC22®, to allow cryo-sectioning. Frozen histological sections, 10-μm in thickness, were cut by a disposable blade edge from the distal side of the block. The sections were mounted on room-temperature glass microscope slides which were air dried and fixed in 10% buffered Formalin for 10 minutes, followed by washing in water. The slides were stained using the standard haematoxylin and eosin method. Staining provides colour and contrast to the specimen, allowing more details to be observed. Photography of stained and unstained sections was achieved using an EOS 5D Mark III (Ota-ku, Tokyo, Japan) and a Light Box (LitEnergy 9 × 12 Inch Light Pad). This allowed for images showing the complete transverse section of the porcine heart artery.

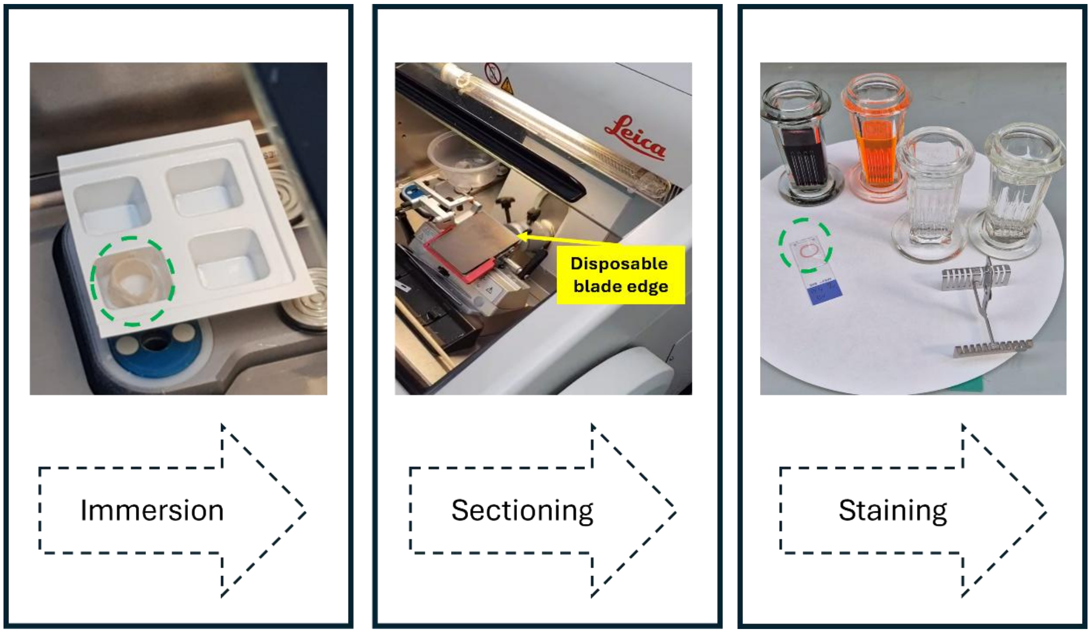

Figure 5. 7: Histological preparations of an ex-vivo porcine heart artery. The immersion phase included immersing the artery into a mould. The sectioning phase included cutting frozen histological sections using a disposable blade edge. Staining was conducted through a standard haematoxylin and eosin technique. The dashed green circle indicates the sample at the different preparation stage.

5.4. Results and Discussions

5.4.1. Array Characterisation

5.4.1.1. Electrical Impedance

The electrical impedance magnitude and the phase angle were measured across all elements of the IVUS array. The average impedance magnitude and phase angle spectra are shown in Figs. 5. 8 (a) and (b), respectively. The measured impedance magnitude shows uniformly damped responses across all of the elements in the array, with the phase angle spectrum indicating resonance at around 21 MHz, and phase variations from approximately 90.7° to 91.7°. The damped responses observed across all array elements are attributed to the weak resonance nature of ZnO and losses associated with the coaxial cable employed for data acquisition, in conjunction with the 3-D printed Composite-X inner core, which served as both to assemble the array and as a backing material.

(a) (b)

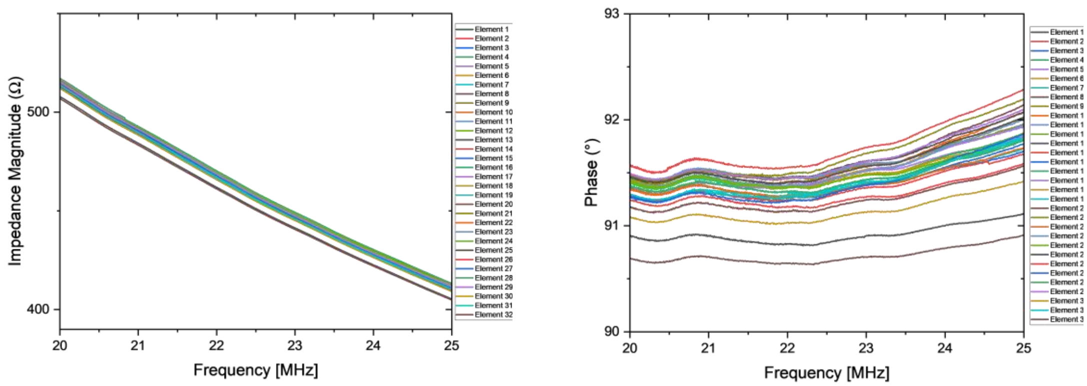

Figure 5. 8: Measured electrical impedance response across all array elements. (a) Average electrical impedance and (b) phase angle curves with respect to frequency.

5.4.1.2. Pulse-Echo and Energy Considerations

The pulse-echo acquisition approach utilised a transmit aperture comprising three array elements, beamformed with differential time delays to enhance transmitted energy, and a single element for reception. The acoustic field characteristics were evaluated when the IVUS array used one and three elements in transmission. Simulated data was produced through the Verasonics Software (Verasonics Inc., Kirkland, USA), and used to compare against experimental data. The simulation employed the array on an acoustic medium with a longitudinal velocity of 1500 m/s. Fig. 5. 9 shows the geometry configuration considered for simulation, with the IVUS circular array highlighted in red. The experimental configuration had the hydrophone aligned with the acoustic beam of the array element under evaluation (element 16) by finding the location of the peak pressure. The scan area parameters of the acoustic field are presented in Table 5. 1. The scanning programme was utilised to acquire and store the data. Data processing was conducted using MATLAB. Fig. 5. 10 shows experimental and simulated data of the beam profile corresponding to one and three transmissions. The behaviour of the simulated shows good agreement with that of the experiments, with some discrepancies associated with imperfections in the experimental conditions. The transmitted energy with 3 elements, as presented in the simulated and experimental data in Figs. 5. 10 (b) and (d) respectively, is higher than when 1 element was used in transmission, as shown in Figs. 5. 10 (a) and (c). Moreover, the experimental condition is influenced by the performance variations in the ultrasonic array elements. This is primarily attributed to manufacturing and aging-related degradation effects, leading to non-uniform element responses, which are not accounted for in the simulation model that assumes consistent performance across all array elements. Another aspect is crosstalk between array elements. This causes unwanted signals from neighbouring elements to degrade the beam profile, for instance, by introducing distortions or anomalous behaviours [122, 123].

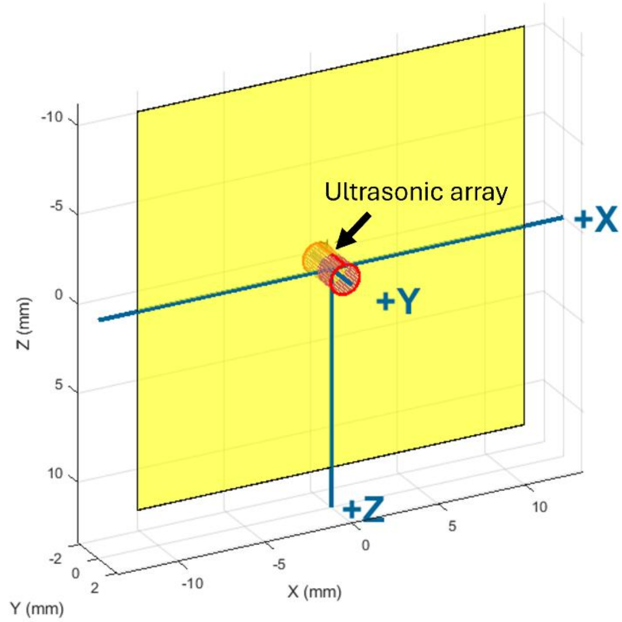

Figure 5. 9: Geometry configuration considered in simulation conditions.

Table 5. 1: Scan area parameters of the acoustic field relative to centre of the array element under evaluation (element 16).

ID	Span (mm)	Step (mm)	Velocity (mm/s)
X	4.875	0.075	0.5
Y	0	0	0
Z	4.875	0.075	0.5

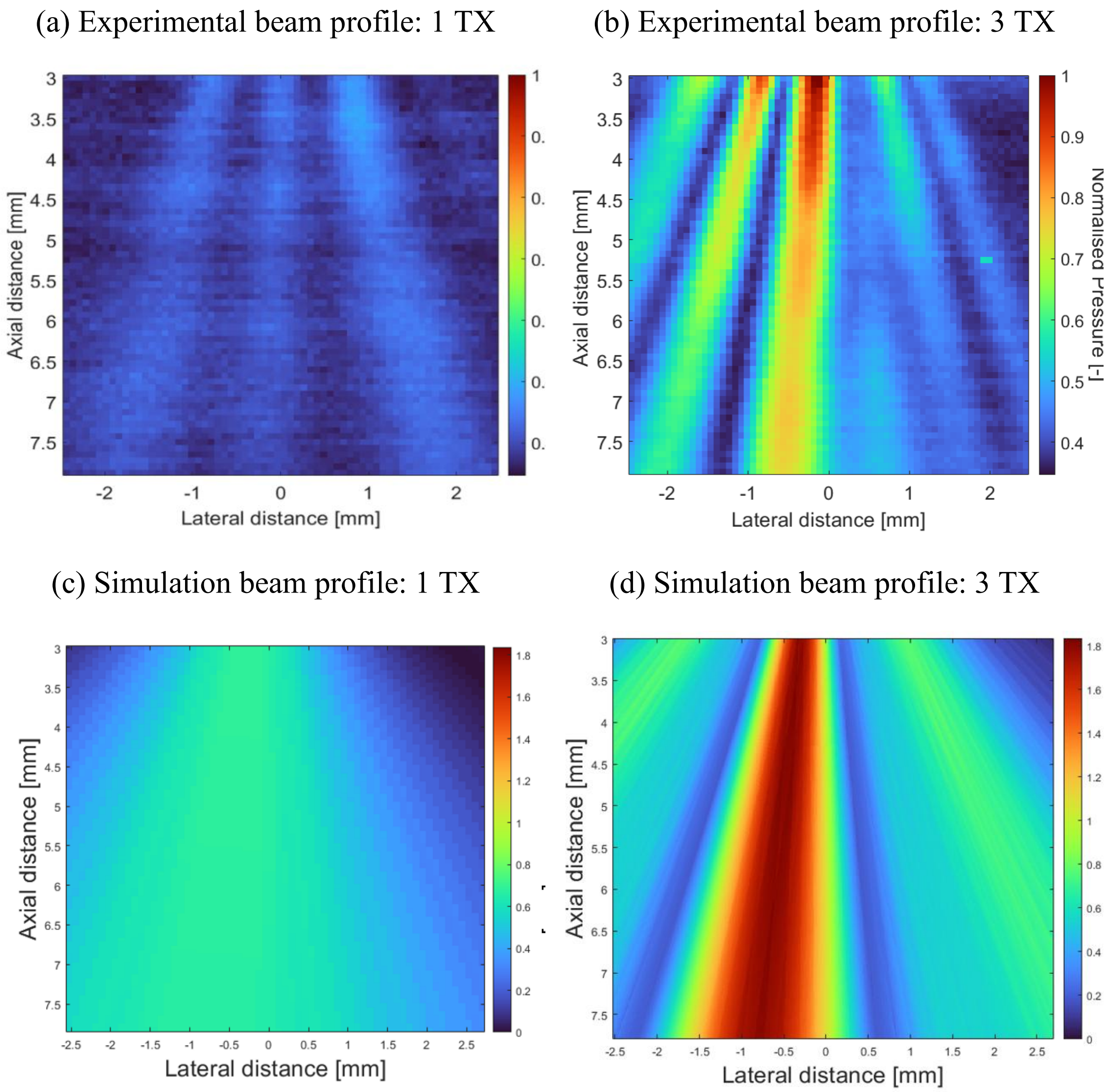

Figure 5. 10: Acoustic beam profile. (a) Experimental results for 1 transmission (TX). (b) Experimental results for 3 TX. (c) Simulated results for 1 TX. (d) Simulated results for 3 TX.

The pulse-echo response of the array was evaluated using a single cycle pulse excitation at 20 MHz, a driving voltage of 30 V generated by the Verasonics Vantage NXT controller, with a receive gain set to 40 dB. Data was processed using MATLAB and the thirty-two A-scan signals were examined. Fig. 5. 11 (a) shows the average time domain, measured from the front face of the reflector, and its frequency spectrum. The frequency spectrum was derived by applying the FFT to the individual time-domain waveforms, followed by averaging. The peak frequency (f_p) was 19.22 $\pm$ 2.20 MHz and the -6 dB bandwidth was calculated to be 66.80 %. Fig. 5. 11 (b) shows the peak frequency response across all the array elements.

(a)

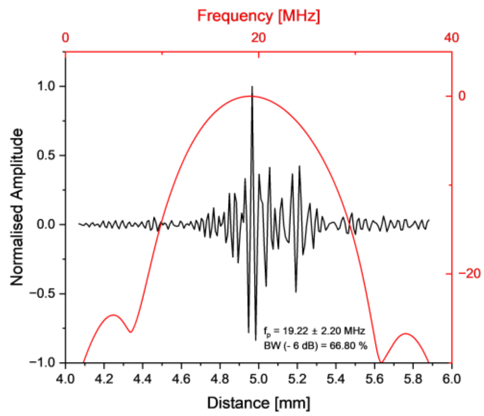

(b)

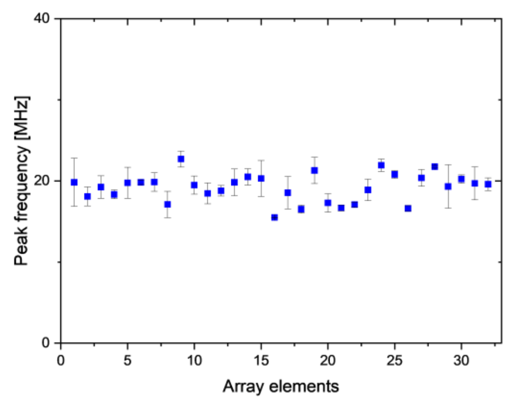

Figure 5. 11: Pulse-echo response. (a) Average time and frequency domains. (b) Peak frequency response across all elements of the array. The peak frequency is represented as f_p and the bandwidth as BW.

5.4.2. Ex-Vivo Porcine Heart Arteries Imaging

The first experiment investigated the plaque imaging and detection across two *ex-vivo* porcine heart arteries, as shown in Figs. 5. 12 (a) and (d). The designed excitation strategies for chirp and Barker were utilised, and a B-scan image frame from the real-time imaging system is presented for each case, as shown in Figs. 5. 12 (b), (c), (e), and (f). The key acquisition parameters consisted of an excitation voltage of 40 V and a receive gain of 30 dB. To evaluate the imaging quality for each excitation technique, the dynamic range was set to 30 dB. All of the B-scan images consistently imaged and detected the calcified plaque and the arterial wall. Some imaging artifacts, common in IVUS [54, 124], can also be observed. For example, acoustic shadowing artifacts behind the calcified plaque can be seen in each case. This occurs as calcium is a strong reflector of ultrasound and it casts shadows over deeper arterial structures. The dead zone is also shown in every B-scan image. The dead zone is the bright ring region in the images, near the transducer elements, where no useful imaging data is obtained. The frequency-modulated chirp scheme provided better imaging quality compared to that of the phase-modulated Barker strategy, with better imaging contrast. On a general outlook, tissues exhibit low reflectivity, allowing partial reflection while permitting substantial ultrasound wave transmission to deeper layers. Sound waves highly distort when travelling through tissues. This causes ultrasound images to show intensity fluctuations, a combination of bright and dark regions, and degraded quality [125].

(a) Artery 1

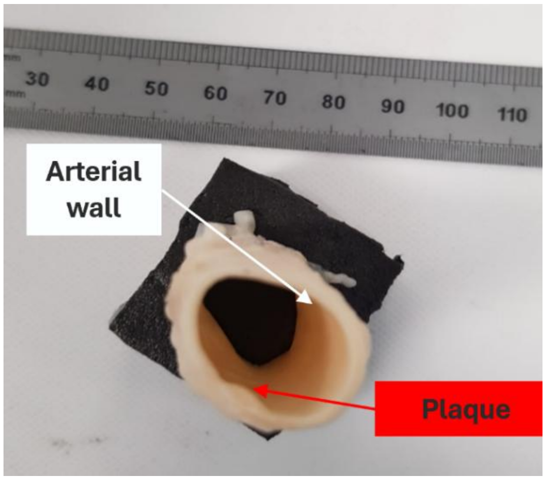

(b) Chirp: artery 1

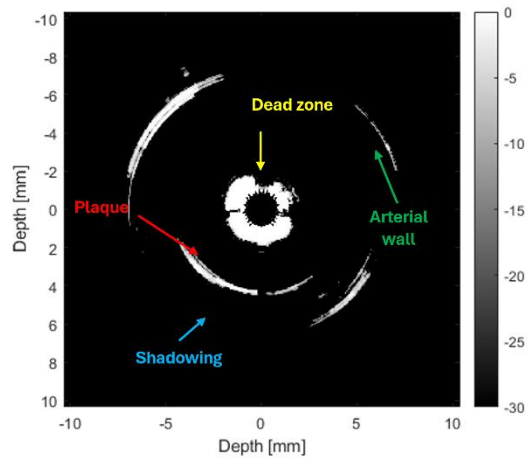

(c) Barker: artery 1

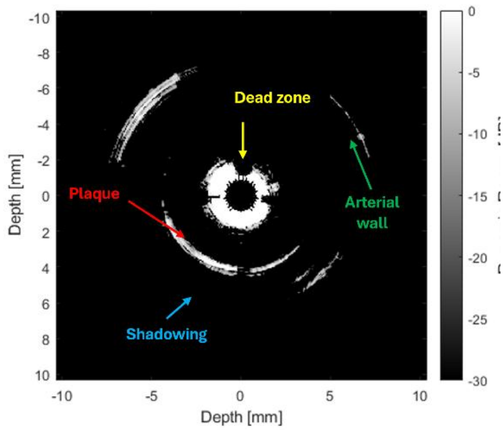

(d) Artery 2

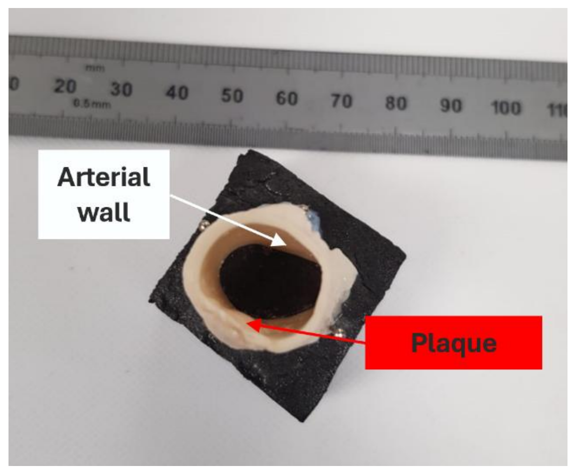

(e) Chirp: artery 2

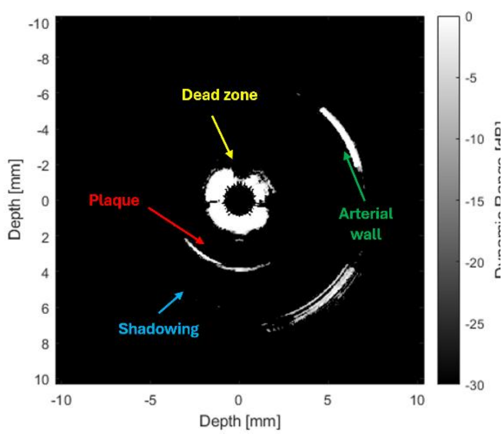

(f) Barker: artery 2

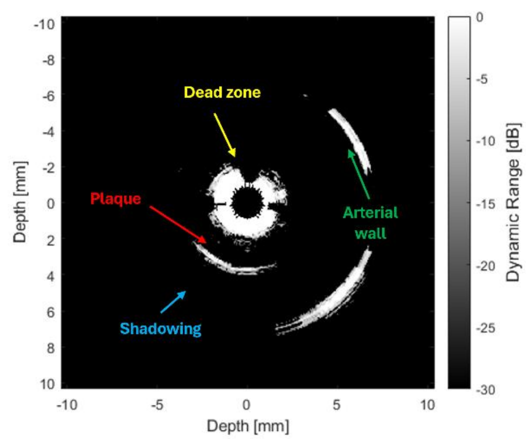

Figure 5. 12: Ex-vivo porcine heart arteries 1 and 2 and corresponding B-scan images. (a) Artery 1, highlighting the plaque and the arterial wall. (b) and (c) B-scan images corresponding to the coded chirp and Barker excitations, respectively, evaluating the plaque imaging and detection in artery 1. (d) Artery 2, highlighting its plaque and arterial wall. (e) and (f) B-scan images corresponding to the coded chirp and Barker excitations, respectively, evaluating the plaque imaging and detection in Artery 2. In all cases, the dead zone and the acoustic shadowing can be observed.

The next investigations used an ex-vivo porcine heart artery, as depicted in Fig. 5. 13 (a), to produce histological sections that were used to compare against an IVUS image. Comparisons between IVUS and histology images have been previously studied [45, 50, 53]. A comparison between the two imaging modalities is presented in Figs. 5.13 (b) – (d). The red arrowheads represent the location of the plaque for each case. An IVUS B-scan image is depicted in Fig. 5.13 (b). This was generated using a Barker excitation strategy. Fig. 5.13 (c) shows an unstained histological section. The plaque is distinctly delineated, with the calcium carbonate clearly evident. Fig. 5.13 (d) depicts a stained histological section. The position of the plaque is discernible, however, the calcium carbonate is removed during the staining process. Neither histological image reveals the protrusion of the calcified plaque, as observed in the arterial image and its corresponding B-scan, in Figs. 5.13 (a) and (b), respectively. The discrepancy may be attributed to compromised structural integrity of the calcium carbonate during the immersion phase of the histological preparation process.

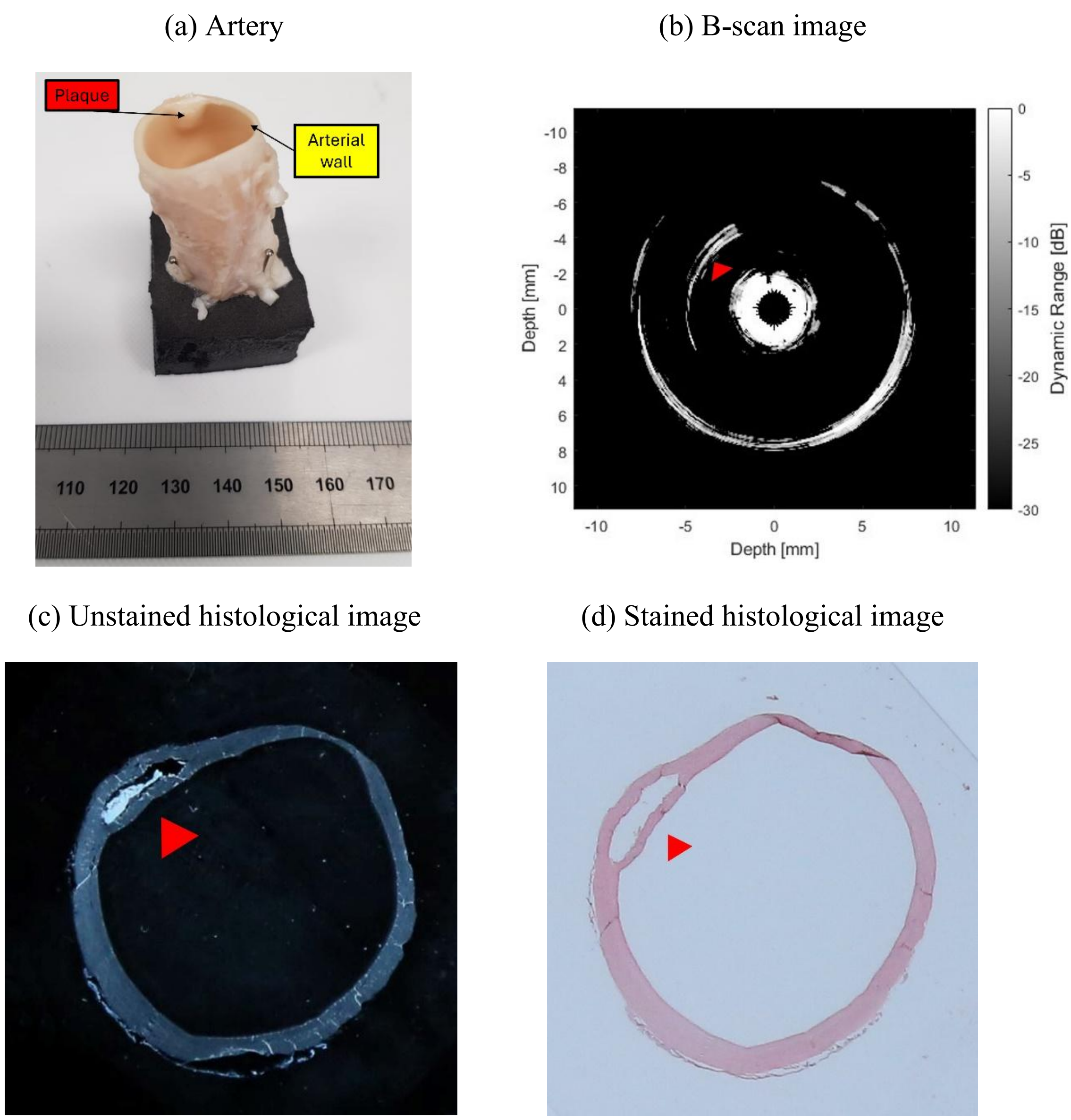

Figure 5. 13: Comparison between IVUS and histology imaging modalities using an ex-vivo porcine heart artery. (a) Artery highlighting the location of its plaque and arterial wall. (b) IVUS B-scan image produced using the phase-modulated Barker excitation scheme. (c) Unstained histological image. The plaque is clearly highlighted, with the calcium carbonate visible. (d) Stained histological image. The standard haematoxylin and eosin method was used for staining. The location of the plaque is visible, however, the calcium carbonate is washed out during the staining process.

5.5. Conclusion

The integration of lead-free transducers into commercial IVUS catheters is both critical and opportune to propel the development of environmentally sustainable piezoelectric materials. Although numerous investigations have explored the piezoelectric properties of lead-free materials, the obstacle of scaling these findings to large-scale manufacturing remains unresolved. Furthermore, the ZnO-based array introduced in this study (5 French gauge) emerges as a compelling solution, leveraging advantages inherent to its fabrication processes.

In this work, a scalable, lead-free and RoHS-compliant ZnO-based array transducer was used for IVUS imaging applications. Frequency- and phase-modulated signals were employed and pulse compressed to improve the signal quality, allowing imaging and detection of calcified plaques in porcine heart arteries. To accomplish this, the array was characterised through electrical impedance analysis and pulse-echo response evaluation, accompanied by characterisation of the acoustic field based on the transmitted energy considerations in the pulse-echo configuration. The impedance magnitude exhibited damped responses consistently across all the elements in the array. The phase angle spectrum revealed a resonance centred at approximately 21 MHz, with phase variations ranging from approximately 90.7° to 91.7° across all array elements. The acoustic field showed higher transmitted energy with 3 elements compared to 1 element. This was observed in both simulation and experimentation, demonstrating good agreement, regardless of some discrepancies related to imperfections in the experimental conditions.

The pulse-echo response exhibited a peak frequency at 19.22 ± 2.20 MHz, accompanied by a -6 dB bandwidth of 66.80 %.

The subsequent experimental work used chirp and Barker signals with equivalent energy levels, combined with pulse compression to image and detect calcified plaques in *ex-vivo* porcine heart arteries. A 10 μm-thick artery histological section, stained through the standard haematoxylin and eosin approach, was presented and compared with an IVUS image. The imaging and detection of plaques was investigated using two different samples. In all cases, B-scan images successfully detecting the calcified plaques were produced, where imaging artifacts, including acoustic shadowing, common in IVUS were observed. Moreover, chirp offered better imaging quality with better imaging contrast compared to Barker. The histology images effectively identified the calcified plaque, indicating strong concordance with the IVUS image. The findings highlight the potential of lead-free transducers as a sustainable option for next-generation IVUS systems.

Chapter 6

Summary

6.1. Conclusions

Piezoelectric ceramics, such as Lead Magnesium Niobate-Lead Titanate (PMN-PT) and Lead Zirconate Titanate (PZT), are widely utilised in both industrial and medical applications due to their high piezoelectric coefficients (d_{33}), which enable high-performance functionality. Concerns regarding human health and environmental impacts stemming from the lead content in piezoelectric ceramics have prompted urgent action. Aligning with international regulatory framework, including the Restriction of Hazardous Substances (RoHS) directive set by the European Union and comparable legislation in Japan and China, the timely adoption of lead-free alternatives is essential to advance the development of environmentally sustainable piezoelectric materials. Despite extensive research into the piezoelectric properties of lead-free materials, the challenge of scaling these findings for large-scale industrial production remains unaddressed. In industrial scenarios, the increasing geometric complexity of components has spurred the development of conformable ultrasonic probes, facilitating effective inspection without the need for custom-designed wedges to adapt to curved or irregular surfaces. Thus, a flexible ultrasonic array that is both RoHS-compliant and scalable, has been proposed as a solution to enhance operability in thick complex-geometry industrial components. In medical settings, a scalable, RoHS-compliant, ZnO-based ultrasonic array has been presented as a lead-free alternative for intravascular ultrasound imaging applications.

Firstly, a 20 MHz flexible linear ultrasonic array was used to inspect a thick convex industrial component combining advanced phase-modulated dual transmission Golay coded excitation with FMC/TFM strategies. The array performance was initially characterised. Golay-coded excitation schemes were designed and implemented. This allowed improvement in the imaging quality of the array. The optimal code length varies by application, balancing SNR and near-field defect detection. A sub-aperture selection approach, based on the array element directivity, further improved SNR and increased imaging penetration depth, enabling a new target to be detected, which was undetected using the conventional pulse excitation method.

The flexible linear array was subsequently employed with single transmission phase-modulated Barker signal and frequency-modulated chirp excitation signal techniques. Compared to Golay excitation strategies, these single transmission methods improve data acquisition efficiency and frame rate by a factor of two, and do not introduce motion-dependent decoding errors. A comparative investigation of the performance associated with the coded excitation strategies and the conventional pulse excitation through simulation and experimentation utilised a novel SNR approach. Qualitative and quantitative measurements were performed, with good agreement between the simulated and the experimental data. Averaging a conventional single pulse excitation enhances SNR. However, it compromises acquisition speed. In contrast, coded excitation strategies improve SNR without compromising acquisition speed by employing extended coded pulses instead of repeated pulses. Moreover, all of the TFM images presented sidelobe artifacts, while for the coded excitation scenario, matched filter processing artifacts were further observed. Convex and concave test specimens were utilised to assess the flexibility of the array, with the array demonstrating excellent conformity to both geometries.

A lead-free 5 French gauge (around 1.67 mm diameter) 32-element 163 μm-pitch 3.82 mm-elevation ultrasonic array has been proposed as an alternative for IVUS catheters. The scalable, RoHS-compliant ZnO-based array was used in conjunction with Barker and chirp excitation schemes for improved imaging quality for detection of calcified plaques in *ex-vivo* porcine heart arteries. The performance of the array was initially characterised. Barker and chirp strategies were designed and implemented to allow real-time imaging. Histology images were acquired and evaluated against an IVUS image. The results underscore the viability of the lead-free array transducer as a sustainable solution for the next generation of IVUS systems.

This thesis has presented work exploring the implementation of coded excitation strategies in both industrial and medical settings. In the industrial context, the performance of the linear ultrasonic array was evaluated offline under static conditions. Conversely, in the medical context, the circular ultrasonic array was assessed in real-time under static conditions, with the long-term goal of integration into a dynamic IVUS diagnostic system incorporating an imaging catheter, a motor drive unit and a controller for image processing and visualisation. Thus, for applications akin to the industrial scenarios examined, the adoption of Golay coded excitation is recommended as the preferred scheme. Golay coding schemes provide optimal range sidelobe cancellation, attributed to the requirement of two consecutive transmissions. The single transmission chirp and Barker excitation strategies result in processing sidelobes in the pulse compression stage. For the medical IVUS scenario, single transmission coded excitation schemes are recommended, as they improve data acquisition efficiency and frame rate by a factor of two compared to the dual transmission Golay coded excitation schemes. Moreover, these schemes avoid motion-dependent decoding errors. Based on qualitative and quantitative performance comparisons with Barker and chirp excitation schemes, chirp strategies are recommended for enhanced signal fidelity and imaging quality.

6.2. Suggestions for Future Work

In order to advance with the work described in this thesis, future work in the industrial settings should be focused on the development of a real-time system to qualitatively and quantitatively evaluate Barker, chirp and Golay excitations incorporating the newly developed SNR method. The proposed system would leverage from the Verasonics NXT platform to enable versatile waveform generation. Coded excitation signals would be transmitted through the transducer, with pulse compression applied to the receive echoes. Real-time visualisation of the processed data would be facilitated through a custom graphical user interface, which supports code selection, live image display, and data export functionality. The development of the real-time data acquisition and processing algorithms will facilitate inspections and improve the practicality of the technology in industrial applications. On the medical scenarios, future research includes a detailed parameter optimisation of the chirp excitation strategy to maximise imaging quality in *ex-*

vivo studies. This includes frequency range, duration, amplitude and windowing considerations to enhance the real-time IVUS imaging capability. Another avenue for future work involves the evaluation of arterial wall imaging and plaque detection through *ex-vivo* porcine blood, furthering the work from PBS, while exploring different plaque compositions that contribute to arterial narrowing and hardening. The signal quality is expected to degrade in blood due to scattering. Therefore, this should be considered and techniques to mitigate this degradation should be studied to promote robust plaque detection. The outcomes of these *ex-vivo* investigations will be essential for enabling the translation of findings to *in-vivo* experiments.

6.3. Final Summary

The research conducted during this Doctor of Philosophy has presented the application of lead-free (ZnO-based) ultrasonic arrays for industrial and medical settings. Phase- and frequency-modulated excitation strategies have been designed and implemented, in conjunction with pulse compression techniques, to improve the signal quality of the array. Evaluation studies of the performance associated with the coded excitation schemes were conducted to improve the ultrasonic array operability in thick convex and concave components. Moreover, a novel SNR approach was developed. This allowed the characterisation of the image noise region and identified parameters where the SNR converged. Furthermore, the development of a novel lead-free transducer system for intravascular ultrasound catheters was presented. The system incorporates the high-frequency, flexible array transducer combined with coded excitation schemes. This allowed imaging and detection of calcific plaques in *ex-vivo* porcine heart arteries.

References

[1] M. Pelayo Garcia, D. Gibson, D. A. Hughes, C. Garcia Nuñez, "A Refined Quasi-Static Method for Precise Determination of Piezoelectric Coefficient of Nanostructured Standard and Inclined Thin Films," Advanced Physics Research, pp. 1-12, Nov. 2023. DOI: 10.1002/apxr.202300091

[2]European Directive 2002/95/EC, "Restriction of the use of certain hazardous substances in electrical and electronic equipment," *Off. J. Eur. Union*, vol. L37, pp. 19–23, Feb. 2003.

[3]European Directive 2011/65/EU, "Restriction of the use of certain hazardous substances in electrical and electronic equipment," *Off. J. Eur. Union*, vol. L174, pp. 88–110, Jul. 2011.

[4]European Directive 2018/736/EU, "Restriction of the use of certain hazardous substances in electrical and electronic equipment," *Off. J. Eur. Union*, vol. L123, pp. 94–96, May 2018

[5] E. Ringgaard, F. Levassort, K. Wang, J. Vaitekunas, H. Nagata, "Lead-Free Piezoelectric Transducers," IEEE, vol. 71 (1), pp. 3-15, Jan. 2024DOI: 10.1109/TUFFC.2023.3340950

[6] J. Koruza, A. J. Bell, T. Frömling, K. G. Webber, K. Wang, J. Rödel, "Requirements for the transfer of lead-free piezoceramics into application," J Materiomics, vol. 4 (1). pp. 13-26, Mar. 2018. DOI: 10.1016/j.jmat.2018.02.001

[7]J. Rödel, K. G. Webber, R. Dittmera, W. Jo, M. Kimura, D. Damjanovic, "Transferring lead-free piezoelectric ceramics into application," Journal of the European Ceramic

Society, vol. vol. 35 (6), pp. 1659-1681, Jun. 2015. DOI: 10.1016/j.jeurceramsoc.2014.12.013

[8] H. Hu, X. Zhu, C. Wang, L. Zhang, X. Li, S. Lee, Z. Huang, R. Chen, Z. Chen, C. Wang, Y. Gu, Y. Chen, Y. Lei, T. Zhang, N. Kim, Y. Guo, Y. Teng, W. Zhou, Y. Li, A. Nomoto, S. Sternini, Q. Zhou, M. Pharr, F. L. di Scalea, S. Xu1, "Stretchable ultrasonic transducer arrays for three-dimensional imaging on complex surfaces" Science advances, vol. 4 (3)., pp. 1-11, Mar. 2018. DOI: 10.1126/sciadv.aar3979

[9]C. J. L. Lane, "The inspection of curved components using flexible ultrasonic arrays and shape sensing fibres," *Case Stud. Nondestruct. Test. Eval*. 1, 13–18 (2014). DOI: 10.1016/j.csndt.2014.03.003

[10] Y. Zheng, X. Zhao, S.-J. Song, J. Zhang, "Beam generating and sound field modeling of flexible phased arrays for inspecting complex geometric components," *Wave Motion*, vol. 94, 2020. DOI: 10.1016/j.wavemoti.2019.102494

[11] K. Nakahata, S. Tokumasu, A. Sakai, Y. Iwata, K. Ohira, Y. Ogura, "Ultrasonic imaging using signal post-processing for a flexible array transducer," *NDT&E International*, vol. 82., pp. 13-25, 2016. DOI: 10.1016/j.ndteint.2016.04.002

[12] C. Wang, X. Chen, L. Wang, M. Makihata, H. C. Liu, T. Zhou, X. Zhao, "Bioadhesive ultrasound for long-term continuous imaging of diverse organs," *The American Association for the Advancement of Science*, vol. 377., pp. 517 - 523, 2022. DOI: 10.1126/science.abo2542

[13] J. Elloian, J. Jadwiszczak, V. Arslan, J. D. Sherman, D. O. Kessler, K. L. Shepard, "Flexible ultrasound transceiver array for non-invasive surface-conformable imaging

enabled by geometric phase correction," *Nature Publishing Group*, vol. 12., pp. 1-12, 2022. DOI: 10.1038/s41598-022-20721-7

[14] J. Chang, Z. Chen, Y. Huang, Y. Li, X. Zeng, C. Lu, "Flexible ultrasonic array for breast-cancer diagnosis based on a self-shape-estimation algorithm," *Ultrasonics*, vol. 108., 2020. DOI: 10.1016/j.ultras.2020.106199

[15] O. Roy, S. Mahaut, O. Casula, "Control of the ultrasonic beam transmitted through an irregular profile using a smart flexible transducer: modelling and application," *Ultrasonics*, vol. 40., pp. 243–246, 2002. DOI: 10.1016/S0041-624X(02)00145-2

[16] C. Qiu *et al.*, "Textured-piezoelectric-ceramic-based focused intravascular ultrasonic transducer with improved image quality and uniformity," *Applied physics letters,* vol. 125, no. 23, 2024, doi: 10.1063/5.0237897.

[17] J. Wang, Z. Zheng, J. Chan, and J. T. W. Yeow, "Capacitive micromachined ultrasound transducers for intravascular ultrasound imaging," *Microsyst Nanoeng,* vol. 6, no. 1, pp. 73-73, 2020, doi: 10.1038/s41378-020-0181-z.

[18] B. Rocks, F. Gaudenzi, D. Irving, D. A. Hughes, "Fully-flexible Thin-film Ultrasonic Array for use in Industrial NDE Applications," *IEEE International Ultrasonics Symposium*, Glasgow, Scotland, 2019.

[19] D. Lines, E. Mohseni, Y. Javadi, C. Mineo, R. Vithanage, Z. Qiu, C. MacLeod, G. Pierce, A. Gachagan, "Using Coded Excitation to maintain Signal to Noise for FMC+TFM on Attenuating Materials," *IEEE. IUS*, pp. 1–4, 2019.

[20] B. Rocks, D. Irving, K.L. McAughey, H.G. Wells, C.B. Thring, D.A. Hughes, Noise Reduction in Flexible-Array-Inspection Images with Machine Learning for

Aerospace Applications. In Proceedings of the 2021 IEEE International Ultrasonics Symposium (IUS), Xi'an, China, 11–16 September 2021.

[21] E. A. Foster *et al.*, "Automated Real-Time Eddy Current Array Inspection of Nuclear Assets," *SENSORS-BASEL,* vol. 22, no. 16, p. 6036, 2022, doi: 10.3390/s22166036.

[22] D. Ganguly, S. Chakraborty, M. Balitanas, and T.-h. Kim, "Medical Imaging: A Review," vol. 78, pp. 504-516, 2010, doi: 10.1007/978-3-642-16444-6_63.

[23] R. Hanke, T. Fuchs, and N. Uhlmann, "X-ray based methods for non-destructive testing and material characterization," *NUCL INSTRUM METH A,* vol. 591, no. 1, pp. 14-18, 2008, doi: 10.1016/j.nima.2008.03.016.

[24] V. P. Vavilov and D. D. Burleigh, "Review of pulsed thermal NDT: Physical principles, theory and data processing," *NDT&E INT,* vol. 73, pp. 28-52, 2015, doi: 10.1016/j.ndteint.2015.03.003.

[25] A. Zolfaghari and F. Kolahan, *Reliability and Sensitivity of Visible Liquid Penetrant Ndt for Inspection of Welded Components.* Materials Testing, 2017. **59**(3): p. 290-294.

[26] E. Germano et al., "Application of Golay-based total focusing method using a high-frequency, lead-free, flexible ultrasonic array for inspection of thick non-planar industrial components," NDT & E international : independent nondestructive testing and evaluation, vol. 150, p. 103282, 2025, doi: 10.1016/j.ndteint.2024.103282.

[27] S. Balocco, "Intravascular Ultrasound: From Acquisition to Advanced Quantitative Analysis," 2020.

[28] T. L. Szabo, "Diagnostic Ultrasound Imaging: Inside Out," 2014, doi: 10.1016/C2011-0-07261-7

[29] M. Matsukawa, P.-K. Choi, K. Nakamura, H. Ogi, H. Hasegawa, and p. Institute of Physics, "Ultrasonics : physics and applications," 2022, doi: 10.1088/978-0-7503-4936-9

[30] R. McPhillips, "Fabrication of Ultrasound Transducers and Arrays Integrated within Needles for Imaging Guidance and Diagnosis," 2017.

[31] E. Nicolson, "Considerations for an in-process ultrasonic phased array inspection method for narrow gap welds," 2024, doi: 10.48730/g37h-8m40.

[32] E. Duernberger, "Advanced non-destructive testing of blade manufacturing defects," 2023, doi: 10.48730/e6hm-hd58.

[33] Drinkwater BW, Wilcox PD. Ultrasonic arrays for non-destructive evaluation: a review. NDT E Int 2006;39(7):525–41.

[34] IMASONIC. *Design Notes for Phased Array*. [cited June 2025]; Available from: https://www.imasonic.com/industry/design-notes-for-phased-array/.

[35] Evident. *Grating Lobes and Side Lobes*. Phased Array Tutorial [cited June 2025]; Available from: https://www.olympus-ims.com/en/ndt-tutorials/transducers/lobes/.

[36] Z. Zhang, Q. Li, M. Liu, W. Yang, and Y. Ang, "Through transmission ultrasonic inspection of fiber waviness for thickness-tapered composites using ultrasound non-reciprocity: Simulation and experiment," *ULTRASONICS,* vol. 123, pp. 106716-106716, 2022, doi: 10.1016/j.ultras.2022.106716.

[37] Sonatest. *Ultrasonic Inspection of Welds in Tubes & Pipes*. [cited June 2025]; Available

from:https://sonatest.com/application/files/4016/9563/2199/Ultrasonic_Inspection_of_Welds_in_Tubes__Pipes_MKT271120.pdf

[38] S. J. Lim, Y. L. Kim, S. Cho, and I. K. Park, "Ultrasonic Inspection for Welds with Irregular Curvature Geometry Using Flexible Phased Array Probes and Semi-Auto Scanners: A Feasibility Study," APPL SCI-BASEL, vol. 12, no. 2, p. 748, 2022, doi: 10.3390/app12020748.

[39] S. Chatillon, G. Cattiaux, M. Serre, and O. Roy, "Ultrasonic non-destructive testing of pieces of complex geometry with a flexible phased array transducer," *ULTRASONICS,* vol. 38, no. 1, pp. 131-134, 2000, doi: 10.1016/S0041-624X(99)00181-X.

[40] O. Roy and M. S. Chatillon, "Ultrasonic inspection of complex geometry component specimen with a smart flexible contact phased array transducer: modeling and application," *ULTSYM,* vol. 1, pp. 763-766 vol.1, 2000, doi: 10.1109/ULTSYM.2000.922656.

[41] A. J. Hunter, B. W. Drinkwater, and P. D. Wilcox, "Ultrasonic imaging using a flexible array: Improvements to the maximum contrast autofocus algorithm," *AIP CONF PROC,* vol. 1096, no. 1, pp. 800-807, 2009, doi: 10.1063/1.3114338.

[42] IMASONIC. *SMART CONTACT LINEAR ARRAYS*. [cited June 2025]; Available from: https://www.imasonic.com/industry/smart-contact-linear-arrays/

[43] J. Russel, " The Development and Implementation of Advanced Ultrasonic Phased Array Technology," 2010.

[44] J. S. Lim, T. S. Park, Y. M. Choi, and I. K. Park, "Improvement in Accuracy of a Multi-Joint Robotic Ultrasonic Inspection System for the Integrity of Composite

Structures," *APPL SCI-BASEL,* vol. 10, no. 19, pp. 6967-11, 2020, doi: 10.3390/app10196967.

[45] R. P. Zangabad, J. G. Bosch, F. Mastik et al., “Real-Time Coded Excitation Imaging Using a CMUT-Based Side Looking Array for Intravascular Ultrasound,” T-UFFC, vol. 68, no. 6, pp. 2048-2058, 2021.

[46] B. Liu *et al.*, "A Novel Dual-Element Catheter for Improving Non-Uniform Rotational Distortion in Intravascular Ultrasound," *TBME,* vol. 70, no. 6, pp. 1768-1774, 2023, doi: 10.1109/TBME.2022.3226955.

[47] Rodnieoro. *Percutaneous Coronary Intervention (PCI)*. [cited June 2025]; Available from: https://rodnieoro.com/home/percutaneous-coronary-intervention-angioplasty

[48] van der Steen, A. F. W. *et al.* 2006 IVUS beyond the horizon. *EuroIntervention* 2, 132 –142

[49] S. K. Mehta, J. R. McCrary, A. D. Frutkin, W. J. S. Dolla, and S. P. Marso, "Intravascular ultrasound radiofrequency analysis of coronary atherosclerosis: an emerging technology for the assessment of vulnerable plaque," *EUR HEART J,* vol. 28, no. 11, pp. 1283-1288, 2007, doi: 10.1093/eurheartj/ehm112.

[50] N. A. L. Yap *et al.*, "What have we learnt from histology about the efficacy of coronary imaging modalities in assessing plaque composition?," *FRONT CARDIOVASC MED,* vol. 12, p. 1507892, 2025, doi: 10.3389/fcvm.2025.1507892.

[51] Z. Yang, L. Liu, X. Li, J. Li, Y. Jiao, and Y. Cui, "Development and Control of a Dual-Mode Magnetic Intravascular Ultrasound Robot for Imaging in Tortuous Blood

Vessels," *TMECH,* vol. 30, no. 1, pp. 168-179, 2025, doi: 10.1109/TMECH.2024.3392243.

[52] A. J. V. Mézquita *et al.*, "Clinical quantitative coronary artery stenosis and coronary atherosclerosis imaging: a Consensus Statement from the Quantitative Cardiovascular Imaging Study Group," *Nat Rev Cardiol,* vol. 20, no. 10, pp. 696-714, 2023, doi: 10.1038/s41569-023-00880-4.

[53] M. Ono *et al.*, "Advances in IVUS/OCT and Future Clinical Perspective of Novel Hybrid Catheter System in Coronary Imaging," *FRONT CARDIOVASC MED,* vol. 7, pp. 119-119, 2020, doi: 10.3389/fcvm.2020.00119.

[54] Xu, J. & Lo, S. Fundamentals and role of intravascular ultrasound in percutaneous coronary intervention. *Cardiovasc. Diagn. Ther.* 10, 1358–1370 (2020).

[55] G. Mintz, "American College of Cardiology Clinical Expert Consensus Document on Standards for Acquisition, Measurement and Reporting of Intravascular Ultrasound Studies (IVUS). A report of the American College of Cardiology Task Force on Clinical Expert Consensus Documents developed in collaboration with the European Society of Cardiology endorsed by the Society of Cardiac Angiography and Interventions," *Eur J Echocardiogr,* vol. 2, no. 4, pp. 299-313, 2001, doi: 10.1053/euje.2001.0133.

[56] R. Y. Chiao, and X. Hao, "Coded Excitation for Diagnostic Ultrasound: A System Developer's Perspective," *Tran. Ult.*, vol. 52, no. 2, pp. 160–170, Feb. 2005. DOI: 10.1109/TUFFC.2005.1406543

[57] F. Gini, A. De Maio, and L. Patton "Classical radar waveform design," in *Waveform Design and Diversity for Advanced Radar Systems,* London, England, United Kingdom: The Institution of Engineering and Technology, 2012, pp. 1–9.

[58] N. Levanon, and E. Mozeson “Matched Filter,” in *Radar Signals,* Hoboken, New Jersey, USA: John Wiley & Sons, 2004, pp. 20–24.

[59] J. Isla, F. Cegla, “Coded Excitation for Pulse-Echo Systems,” IEEE, vol. 64 (4), pp. 736-748, Apr. 2017. DOI: 10.1109/TUFFC.2017.2661383

[60] L. Jie and M. F. Insana, "Coded pulse excitation for ultrasonic strain imaging," *T-UFFC,* vol. 52, no. 2, pp. 231-240, 2005, doi: 10.1109/TUFFC.2005.1406549.

[61] C. E. Cooke, “The early history of pulse compression radar-the history of pulse compression at Sperry Gyroscope Company,” T-AES, vol. 24, no. 6, pp. 825-833, 1988.

[62] S. Hedayatrasa, G. Poelman, J. Segers et al., “Novel discrete frequency-phase modulated excitation waveform for enhanced depth resolvability of thermal wave radar,” Mechanical systems and signal processing, vol. 132, pp. 512-522, 2019.

[63] A. S. Mudukutore, V. Chandrasekar, and R. J. Keeler, “Pulse compression for weather radars,” TGRS, vol. 36, no. 1, pp. 125-142, 1998.

[64] M. Parlak, M. Matsuo, and J. F. Buckwalter, “Analog Signal Processing for Pulse Compression Radar in 90-nm CMOS,” TMTT, vol. 60, no. 12, pp. 3810-3822, 2012.

[65] M. H. Bae, W. Y. Lee, M. K. Jeong et al., “Orthogonal Golay code based ultrasonic imaging without reducing frame rate,” ULTSYM, vol. 2, pp. 1705-1708 vol.2, 2002.

[66] R. Y. Chiao, and L. J. Thomas, “Synthetic transmit aperture imaging using orthogonal Golay coded excitation,” ULTSYM, vol. 2, pp. 1677-1680 vol.2, 2000.

[67] T. Misaridis, and J. A. Jensen, “Use of modulated excitation signals in medical ultrasound. Part I: basic concepts and expected benefits,” T-UFFC, vol. 52, no. 2, pp. 177-191, 2005.

[68] T. Misaridis, and J. A. Jensen, "Use of modulated excitation signals in medical ultrasound. Part II: design and performance for medical imaging applications," T-UFFC, vol. 52, no. 2, pp. 192-207, 2005.

[69] T. Misaridis, and J. A. Jensen, "Use of modulated excitation signals in medical ultrasound. Part III: high frame rate imaging," T-UFFC, vol. 52, no. 2, pp. 208-219, 2005.

[70] I. Trots, "Mutually Orthogonal Golay Complementary Sequences in Synthetic Aperture Imaging Systems," Archives of acoustics, vol. 40, no. 2, pp. 283-289, 2015.

[71] I. Trots, Y. Tasinkevych, A. Nowicki et al., "Golay coded sequences in synthetic aperture imaging systems," Archives of acoustics, vol. 36, no. 4, pp. 913-926, 2011.

[72] E. P. Vienneau, and B. C. Byram, "A Coded Excitation Framework for High SNR Transcranial Ultrasound Imaging," TMI, vol. 42, no. 10, pp. 1-1, 2023.

[73] X. Wang, J. Yang, J. Ji et al., "Research on Golay-coded excitation in real-time imaging of high frequency ultrasound biomicroscopy," Sci Rep, vol. 11, no. 1, pp. 1848-1848, 2021.

[74] B. U. Zejak, I. S. Simic, and A. J. Zejak, "Matched and mismatched pulse compression in medical ultrasound imaging," EURCON, vol. 2, pp. 333-336 vol.2, 2001.

[75] H. Zhang, S. Wu, D. Ta et al., "Coded excitation of ultrasonic guided waves in long bone fracture assessment," Ultrasonics, vol. 54, no. 5, pp. 1203-1209, 2014.

[76] A. Bernieri, L. Ferrigno, M. Laracca et al., "Ultrasonic NDT on aluminum bars: An experimental performance comparison of excitation and processing techniques,"

Measurement : journal of the International Measurement Confederation, vol. 128, pp. 393-402, 2018.

[77] F. Cegla, and B. Herdovics, “Coded excitation, motion and signal-to-noise ratio,” ISCAS, pp. 1-4, 2018.

[78] J. Hua, J. E. Michaels, X. Chen et al., “Simultaneous excitation system for efficient guided wave structural health monitoring,” Mechanical systems and signal processing, vol. 95, pp. 506-523, 2017.

[79] J. Hua, L. Zeng, J. Lin et al., “Excitation series design and pulse compression synthesis for high-resolution Lamb wave inspection,” Structural health monitoring, vol. 18, no. 5-6, pp. 1464-1478, 2019.

[80] D. Hutchins, P. Burrascano, L. Davis et al., “Coded waveforms for optimised air-coupled ultrasonic nondestructive evaluation,” Ultrasonics, vol. 54, no. 7, pp. 1745-1759, 2014.

[81] R. Mulaveesala, and S. Venkata Ghali, “Coded excitation for infrared non-destructive testing of carbon fiber reinforced plastics,” Rev Sci Instrum, vol. 82, no. 5, pp. 054902-054902-4, 2011.

[82] M. K. Rizwan, S. Laureti, H. Mooshofer et al., “Ultrasonic imaging of thick carbon fiber reinforced polymers through pulse-compression-based phased array,” Applied sciences, vol. 11, no. 4, pp. 1-15, 2021.

[83] J. Tang, W. Zhu, X. Qiu et al., “Non-contact phase coded excitation of ultrasonic Lamb wave for blind hole inspection,” Ultrasonics, vol. 119, pp. 106606-106606, 2022.

[84] C. Challinor, and F. Cegla, “Pulse compression with and without matched filtering: Why codes beat chirps,” *NDT & E international : independent nondestructive testing and evaluation,* vol. 147, pp. 103180, 2024.

[85] Wang, N.; Yang, C.; Xu, J.; Shi, W.; Huang, W.; Cui, Y.; Jian, X. An Improved Chirp Coded Excitation Based on Compression Pulse Weighting Method in Endoscopic Ultrasound Imaging. *IEEE Trans. Ultrason. Ferroelect. Freq. Control* 2021, 68, 446–452.

[86] Olympus NDT. *Advances in Phased Array Ultrasonic Technology applications – Advanced Practical NDT Series*. 2007

[87] The British Institute of Non-Destructive Testing (BINDT). *C-Scan*. [cited June 2025]; Available from: https://www.bindt.org/What-is-NDT/Index-of-acronyms/C/C-Scan/#:~:text=C%2DScan%20refers%20to%20the,plan%20view%20of%20the%20component.

[88] Nicolson E, et al. Dual-tandem phased array Method for Imaging of near-vertical Defects in narrow-gap welds. NDT E Int 2023;135:102808.

[89] C. Holmes, B. W. Drinkwater, and P. D. Wilcox, “Post-processing of the full matrix of ultrasonic transmit–receive array data for non-destructive evaluation,” *NDT & E.*, vol. 38, pp. 701–711, Apr. 2005. DOI: 10.1016/j.ndteint.2005.04.002

[90] Evident. *Use of the Total Focusing Method with the Envelope Feature*. [cited June 2025]; Available from: https://ims.evidentscientific.com/en/learn/white-papers/use-of-the-total-focusing-method-with-the-envelope-feature

[91] R. Mohammadkhani, L. F. Zanotti, J. Padiyar M., I. Petrunin, J. Raposo, A. Tsourdos, I. Gray, “Improving Depth Resolution of Ultrasonic Phased Array Imaging

to Inspect Aerospace Composite Structures," Sensors, vol. 20, pp. 1-18, Jan. 2020. DOI:10.3390/s20020559

[92] C.M. Wong, S.F. Chan, R. Liu, J. Zhang, W.C. Wu, Z. Liang, H.M. Yau, D.Y. Wang, S. Li, K.H. Lam, W.B. Qiu, H.S. Luo, J.Y. Dai, "20-MHz phased array ultrasound transducer for in vivo ultrasound imaging of small animals," Ultrasonics, vol. 126, pp. 1-9, Dec. 2022. DOI: 10.1016/j.ultras.2022.106821

[93] W. Ninghao, L. Xinze, X. Jie, J. Yang, C. Yaoyao, and J. Xiaohua, "A high frequency endoscopic ultrasound imaging method combining chirp coded excitation and compressed sensing," *Ultrasonics*, vol. 121., pp. 1-11, 2022. DOI: 10.1016/j.ultras.2021.106669

[94] D. Hughes, D. Irving, "Ultrasound Array Transducer Manufacturing," United Kingdom Patent WO2019166815 (A1), Sep.6, 2019.

[95] D. Hughes, D. Gibson, D. Irving, "Formation of Piezoelectric Devices," United Kingdom Patent WO2019166805 (A2), Sep. 6, 2019.

[96] J. Mamou, J. A. Ketterling, and R. H. Silverman, "Chirp-Coded Excitation Imaging With a High-Frequency Ultrasound Annular Array," *Tran. Ult.*, vol. 52, no. 2, pp. 508–513, Feb. 2008. DOI: 10.1109/TUFFC.2008.670

[97] Yang, Y.; Wang, P.; Jia, Y.; Jing, L.; Shi, Y.; Sheng, H.; Jiang, Y.; Liu, R.; Xu, Y.; Li, X. Rail Fracture Monitoring Based on Ultrasonic-Guided Wave Technology with Multivariate Coded Excitation. *Ultrasonics* 2024, 136, 107164.

[98] T. X. Misaridis, K. Gammelmark, C. H. Jørgensen, N. Lindberg, A. H. Thomsen, M. H. Pedersen, and J. A. Jensen, "Potential of coded excitation in medical ultrasound imaging," *Ultrasonics*, vol. 38, pp. 183–189, 2000.

[99] BSI Standards Publication, “Non-destructive testing – Characterisation and verification of ultrasonic phased array equipment,” BS EN ISO 18563-2:2017, Sep. 2017

[100] Verasonics “Vantage Product Specification,” May 2022, pp. 1–40.

[101] Verasonics “Vantage Sequence Programming Manual,” Nov. 2022, pp. 1–195.

[102] A. Nowicki, W. Secomski, I. Trots, and J Litniewski, “Extending penetration depth using coded ultrasonography,” *Bull. Pol. Acad. Sci.*, vol. 52, no. 3, pp. 215-220, 2004.

[103] F. Hamilton, P. Hoskins, G. Corner, and Z. Huang, “Nonlinear Harmonic Distortion of Complementary Golay Codes,” *Ultr. Imag.*, vol. 45, no. 1, pp. 22–29, 2023. DOI: 10.1177/01617346221147820

[104] Paul Wilcox. MFMC format. 2: [Available from: https://github.com/ndtatbristol/mfmc; 2019.

[105] D. Lines, “The Application of Real-Time Medical Ultrasound Imaging to NDT,” The British Institute of NDT Annual Conference on Non-Destructive Testing for the Engineer, Keele, 19-21 September 1983.

[106] C. Li, D. Pain, P. D. Wilcox, and B. W. Drinkwater, "Imaging composite material using ultrasonic arrays," *NDT & E international : independent nondestructive testing and evaluation,* vol. 53, pp. 8-17, 2013, doi: 10.1016/j.ndteint.2012.07.006.

[107] P. D. Wilcox and Z. Jie, "Quantification of the Effect of Array Element Pitch on Imaging Performance," *T-UFFC,* vol. 65, no. 4, pp. 600-616, 2018, doi: 10.1109/TUFFC.2018.2794627.

[108] EXTENDE. CIVA NDE software. 2020.

[109] Sweeney NE, et al. In-process phased array ultrasonic weld pool monitoring. NDT E Int 2023;137:102850.

[110] S. Zhang, R. Cheng, C. Tao, and X. Liu, Appl. Phys. Express 9, 047301 (2016).

[111] V. T Potsika *et al.*, "Computational Study of the Effect of Cortical Porosity on Ultrasound Wave Propagation in Healthy and Osteoporotic Long Bones," *Materials (Basel),* vol. 9, no. 3, p. 205, 2016, doi: 10.3390/ma9030205.

[112] K. Russell *et al.*, "Assessment of wasted myocardial work: A novel method to quantify energy loss due to uncoordinated left ventricular contractions," *Am J Physiol Heart Circ Physiol,* vol. 305, no. 7, pp. H996-H1003, 2013, doi: 10.1152/ajpheart.00191.2013.

[113] E. Moghimirad, A. Mahloojifar, and B. M. Asl, "Computational complexity reduction of synthetic-aperture focus in ultrasound imaging using frequency-domain reconstruction," Ultrason. Imag., vol. 38, no. 3, pp. 175–193, Apr. 2015

[114] Doblhof G, Satrapa J, Coulthard P (2017) Recognising small image quality diferences for ultrasound probes and the potential of misdiagnosis due to undetected side lobes. Ultrasound 25(1):35–44

[115] S. D. Silverstein and L. J. Thomas, "Analytical comparison of sensor signal processing enhancements for NDT synthetic aperture imaging," IEEE Trans. Image Processing, vol. 2, pp. 60–67, 1993.

[116] S. McKnight, et al., A comparison of methods for generating synthetic training data for domain adaption of deep learning models in ultrasonic non-destructive evaluation, NDT E Int. 141 (Jan. 2024) 102978, https://doi.org/10.1016/j.ndteint.2023.102978.

[117] T.-Y. Lai, M. Bruce, and M. A. Averkiou, “Modeling of the acoustic field produced by diagnostic ultrasound arrays in plane and diverging wave modes,” *IEEE Trans. Ultrason., Ferroelectr., Freq. Control*, vol. 66, no. 7, pp. 1158–1169, Jul. 2019.

[118] World Health Organization, *Cardiovascular diseases*. [cited January 2025]; Available from: https://www.who.int/health-topics/cardiovascular-diseases/

[119] M. E. M. K. Abdelaziz *et al.*, "Thermally Drawn Polymeric Catheters for MR-Guided Cardiovascular Intervention," *Adv Sci (Weinh),* vol. 11, no. 45, pp. e2407704-n/a, 2024, doi: 10.1002/advs.202407704.

[120] Verasonics. Vantage NXT product specification. 2024. p. 1–29

[121] G. S. Mintz and G. Guagliumi, "Intravascular imaging in coronary artery disease," *LANCET,* vol. 390, no. 10096, pp. 793-809, 2017, doi: 10.1016/S0140-6736(17)31957-8.

[122] A. Bybi, S. Grondel, J. Assaad, A. C. Hladky-Hennion, C. Granger, and M. Rguiti, "Reducing crosstalk in array structures by controlling the excitation voltage of individual elements: A feasibility study," *ULTRASONICS,* vol. 53, no. 6, pp. 1135-1140, 2013, doi: 10.1016/j.ultras.2013.02.009.

[123] M. Celmer, K. J. Opieliński, and M. Dopierała, "Structural model of standard ultrasonic transducer array developed for FEM analysis of mechanical crosstalk," *ULTRASONICS,* vol. 83, pp. 114-119, 2018, doi: 10.1016/j.ultras.2017.06.006.

[124] Mintz GS. Intravascular imaging of coronary calcification and its clinical implications. J Am Coll Cardiol Img. 2015;8:461–471.

[125] S. H. Contreras Ortiz, T. Chiu, and M. D. Fox, "Ultrasound image enhancement: A review," *BIOMED SIGNAL PROCES,* vol. 7, no. 5, pp. 419-428, 2012, doi: 10.1016/j.bspc.2012.02.002.